Modeling and simulation with molecular dynamics of the edge dislocation behavior in the presence of Frank loops in austenitic stainless steels Fe-Ni-Cr

Jean-Baptiste Baudouin

2014ISAL0055 Thèse

Soutenue le 5 Juin 2014 devant la Commission d'examen

Numéro d'ordre : 2014ISAL0055

Modeling and simulation with molecular dynamics of the edge dislocation behavior in the presence of Frank loops in austenitic stainless steels Fe-Ni-Cr

Présenté par

Jean-Baptiste BAUDOUIN

Pour obtenir le grade de

Docteur de l'Institut National des Sciences de Lyon

École Doctorale : Matériaux de Lyon

Spécialité : Matériaux

Membres du jury :

Xavier Feaugas	Rapporteur
Benoît Devincre	Rapporteur
Charlotte Becquart	Présidente du jury
Chad Sinclair	Examinateur
Michel Perez	Directeur de thèse
Ghiath Monnet	Encadrant
Christophe Domain	Encadrant

Acknowledgments

First and foremost, I would like to express my special appreciation and gratitude to the Head of Departement, Philippe Ollar, who has allowed me to conduct my research in the MMC Department of EDF-R&D research center "Les Renardières". This Department has provided the support and equipment that I have needed to produce and complete my postgraduate thesis.

I also want to thank the MATEIS laboratory, which welcomed me for the first four months of my postgraduate research as well as Jean-Yves Buffière, who heads the Materials Doctoral School of Lyon. I was pleased to collaborate with Roberto Veiga who has taught me the basics of molecular dynamics during this period.

I wish to thank the members of the jury and particularly Charlotte Becquart who did me the honor of chairing this jury, Xavier Feaugas and Benoît Devincre who have agreed to be appointed the rapporteurs of this thesis and Chad Sinclair, who has come a long way from Vancouver to attend this presentation.

I would like to extend my acknowledgment to Abderrahim Al-Mazouzi, the Perform60 project manager, for including this work in his project as well as Benoît Tanguy, the WP2-2 leader. I would also like to thank for their contribution and involvement Olivier Dupond, my Group Leader, who has welcomed me in the Metallurgy team and Christophe Domain, who has integrated me in the Simulation Team.

I received generous support from Michel Perez, my Ph.D. supervisor, who helped me through this difficult task of research and followed the working progress all along my Ph.D. thesis, I am extremely grateful to him. I would also like to thank Ghiath Monnet, who agreed to advise and tutor me for these three consecutive years. Discussions with him have been very insightful. Special thanks to Akiyoshi Nomoto, who gladly allowed me to use his molecular dynamics code and gave me useful advice and comments on this calculation technique. I have really appreciated discussing and exchanging with him day by day. I also want to thank the other research engineers and Ph.D. fellow students of the simulation team, Gilles Adjanor and Philippe Baranek, as well as Davide Costa and Gustavo Doamaral for all our fruitful debates.

Thanks also to the office staff: Chantal Delarue, Isabelle Pirès, Agnès Daime and Chaveli Bitsindou.

My sincere thanks to all the EDF volley-ball players and especially to Daniela Bory, Pierre-Emile Lhuillier, Didier Leclaire and Rémi Le-Berre.

Finally, I am very grateful to my family members, especially my parents and sister, who have been very important for me these last years. Thank you mum for proofreading the English version of this manuscript.

Modeling and simulation with molecular dynamics of the edge dislocation behavior in the presence of Frank loops in austenitic stainless steels Fe-Ni-Cr.

Austenitic stainless steels are widely used in the nuclear industry as internals. These structures reside mainly in the reactor vessel and, due to their proximity with fuel assemblies, are subjected to severe operating conditions. These elements are exposed to high irradiation doses which can reach 100 dpa after 40 years of operating, at a temperature close to 350°C. These operating conditions affect the microstructure of steels and their mechanical behavior, which leads to the deterioration of their mechanical properties and their corrosion resistance.

The objective of this PhD research work is to establish at the atomic scale a constitutive law describing the edge dislocation motion in a random Fe-Ni_{10}-Cr_{20} solid solute solution, to bring a comprehensive understanding of the interaction mechanism between the edge dislocation and the Frank loops and to investigate the effect of temperature, alloying random generator, orientation and size of the Frank loop on the mechanical stress.

To achieve these objectives, molecular dynamics simulations were conducted with a recently developed FeNiCr potential used to mimic the behavior of austenitic stainless steels. These simulations have been performed in static conditions as well as at 300 K, 600 K and 900 K and the interactions realized for loop sizes of 2nm and 10nm.

- a constitutive law taking into account the temperature and strain rate is proposed;
- the interaction between the edge dislocation and the Frank loop revealed 3 kinds of interaction mechanisms: simple shearing, unfaulting and absorption of the loop. Absorption is the most stable mechanism;
- the analyses of the resulting mechanical properties have shown that the unfaulting mechanism requires the highest stress to make the dislocation overcome the obstacle. On the other hand, contrary to previous studies, the unfaulting of the loop surface occurs only when the dislocation comes into contact with the edge dislocation;
- for the 2 nm Frank loop size, the coupling between the probability of the outcome of the reaction and the average strength of the obstacle constitutes useful data for Dislocation Dynamics simulations.

The observations of the resulting Frank loop configurations following the interaction with the dislocation allow justifying the emergence of clear bands observed in TEM. This work has been partially supported by the European Commission FP7 with the grant number 232612 as part of the PERFORM 60 project.

Key-words: austenitic steels, Frank loop, dislocation, plasticity, molecular dynamics

Modélisation et simulation par dynamique moléculaire du comportement de la dislocation coin en présence de boucles de Frank dans les aciers austénitiques inoxydables Fe-Ni-Cr.

Les aciers inoxydables austénitiques sont très utilisés dans l'industrie nucléaire comme structure interne. Ces structures se retrouvent en grande majorité dans la cuve du réacteur et, du fait de leur proximité avec les assemblages combustibles, sont soumis à de rudes conditions d'utilisation. Ces éléments sont donc exposés à des doses d'irradiation élevées et peuvent atteindre 100 dpa après 40 ans d'utilisation, à une température proche de 350°C. Ces conditions d'utilisation modifient la microstructure de l'acier et son comportement mécanique, ce qui entraîne une dégradation de leurs propriétés mécaniques et de leur résistance à la corrosion.

L'objectif de cette thèse est d'établir à l'échelle atomique une loi de comportement décrivant le déplacement d'une dislocation coin dans une solution solide Fe-Ni_{10}-Cr_{20}, d'apporter une compréhension des mécanismes d'interaction entre une dislocation coin et une boucle de Frank et d'investiguer l'effet de la température, du générateur aléatoire d'alliage, de l'orientation et du diamètre de la boucle sur la contrainte mécanique.

Pour atteindre ces objectifs, des simulations en dynamique moléculaire sont réalisées, basées sur potentiel FeNiCr récemment développé pour imiter le comportement de l'acier austénitique inoxydable. Les simulations sont réalisées en conditions statiques, à 300 K, 600 K et 900 K et les interactions effectuées pour des tailles de boucle de Frank de 2 nm et 10 nm.

- nous proposons une loi de comportement où sont incluses la température et la vitesse de déformation;
- l'interaction entre la dislocation coin et la boucle de Frank révèle trois types de mécanismes d'interactions : le cisaillement simple, le défautement et l'absorption de la boucle. L'absorption est le mécanisme le plus stable ;
- Les analyses des propriétés mécaniques résultantes ont montré que le mécanisme de défautement requiert la contrainte la plus élevée pour que la dislocation franchisse l'obstacle. D'autre part, contrairement aux études précédentes, le défautement de la surface de la boucle n'a lieu que lorsque celle-ci entre en contact avec la dislocation coin ;
- dans le cas de la boucle de Frank de 2 nm, la corrélation entre la probabilité du mécanisme d'interaction et la force moyenne de l'obstacle constitue des données utiles pour les simulations en Dynamique des Dislocations.

Les observations des configurations résultantes de la boucle de Frank suite à l'interaction avec la dislocation permettent de justifier l'apparition de bandes claires observées au MET. Ce travail a été partiellement soutenu par la Commission européenne FP7 par le numéro de subvention 232612 dans le cadre du projet PERFORM 60.

Mots-clés : aciers austénitiques, boucle de Frank, dislocation, plasticité, dynamique moléculaire

Table of Contents

Abbreviations and Acronyms

BCC	Body Centered Cubic
BWR	Boiling Water Reactor
CGR	Conjugate Gradient Relaxation
CRSS	Critical Resolved Shear Stress
CSD	Centro-Symmetry Deviation
DD	Dislocation Dynamics
DFT	Density Functional Theory
dpa	displacement per atom
EAM	Embedded Atom Method
FCC	Faced Centered Cubic
FE	Finite Element
GSF	Generalized Stacking Fault
HCP	Hexagonal Close-Packed
MD	Molecular Dynamics
MET	Microscope Électronique en Transmission
PAD	Periodic Array of Dislocations
PBC	Periodic Boundary Conditions
PWR	Pressurized Water Reactor
RPV	Reactor Pressure Vessel
SFE	Stacking Fault Energy
SFT	Stacking Fault Tetrahedron
TEM	Transmission Electron Microscope
UTS	Ultimate Tensile Stress
YS	Yield Stress

Chapter 1. Industrial context

Électricité de France has 58 Units of Pressurized Water Reactor (PWR) which supply 80% of the total amount of electricity for France. A scheme of PWR and its components is represented in Figure 1.1. The reactor core is constituted of the Reactor Pressure Vessel (RPV), within which there are the fuel assembly and internal components (called "internals" in the following) that maintain it. The core is cooled by the water in the primary circuit transmitted to the steam generator, which releases the required steam to produce electricity.

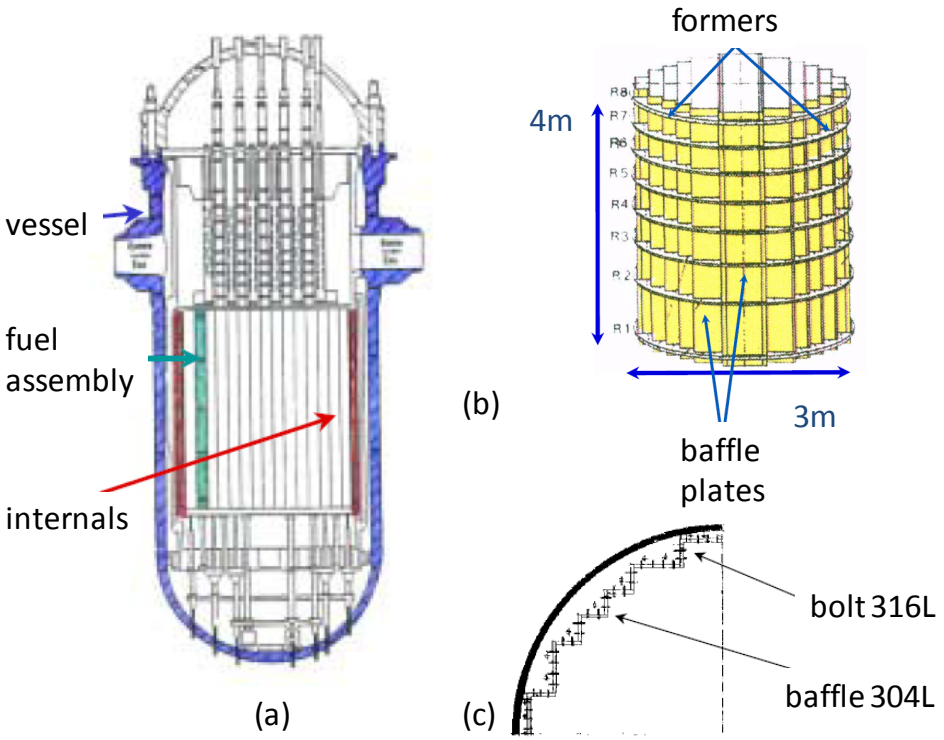

Figure 1.1: Schematic of PWR showing fuel assemblies, internals and the vessel (a). Internals details (b) and cross section to highlight baffles.

1.1. Reactor vessel Internals in Pressurized Water Reactor

Reactor vessel internal components are designed to support the fuel assembly within the reactor vessel. They are subjected to a combined effect of irradiation, temperature and corrosion. Austenitic stainless steels offer a good compromise. These materials offer versatile metallurgy with a wide range of mechanical and physical properties which can be achieved upon application request. The ore is cheap and abundant and the processing techniques like fabrication, forming and welding are economical and available. Although austenitic stainless steels have a good irradiation resistance, they show a high corrosion resistance especially in aqueous media, thus making them a good choice for the nuclear industry. Austenitic stainless steels belong to the 300 series of steel of American standard AISI. The 304 and 316 austenitic stainless steels are used for partitions, reinforcement of core barrel and for bolts.

1.1.1. Functions of internals

We can distinguish the lower Internals from the upper Internals depending on their role in the core. The main purpose of lower internals is to maintain the alignment of the fuel assemblies, the control rods and the in-core instrumentation. They have to support the core weight and channel the coolant

fluid flow. They undergo strong irradiation during the reactor operation. In addition to all these requirements, internals have to exhibit a constant rigidity. In addition to these functions, the upper components are useful in keeping the position of the control rods in the axis of the fuel assemblies.

These internals are near fuel assemblies and are constituted of vertical baffle plates in 304L solution annealing austenitic stainless steels, assembled into 8 levels of horizontal reinforcements with 900-1000 bolts in cold-worked 316 austenitic stainless steels which are dipped in water.

1.1.2. Properties of 300's series

Stainless steels are defined as iron-chromium alloys with a chromium content equal or greater than 10.5 wt.%. This high Chromium content gives stainless steels their excellent corrosion resistance through the formation of a chromium-rich surface oxide. Stainless steels are typically divided into five categories depending on their microstructure and response to the heat treatment. These five categories are martensitic, ferritic, austenitic, duplex (ferritic-austenitic), and precipitation-hardening. Austenitic stainless steels, *e.g.* 304 and 316, are tough and corrosion-resistant alloys of iron, chromium and nickel. A typical composition of these alloys is gathered in Table 1.1:

Table 1.1: Chemical composition of 304 and 316 austenitic stainless steel.

	Steel	Cr	Ni	Mo	C	Mn	Si	P	N	S	Fe
at.%	304	19 ± 1	10 ± 2		0.03	2.0	0.75	0.045	0.10	0.03	Bal.
	316	17 ± 1	12 ± 2	2.5 ± 0.5	0.03	2.0	0.75	0.045	0.10	0.03	Bal.
wt.%	304	17.93 ± 0.94	10.65 ± 2.13		0.0065	1.99	0.38	0.025	0.025	0.017	Bal.
	316	16.04 ± 0.94	11.32 ± 2.13	2.36 ± 0.87	0.0028	1.89	0.71	0.04	0.094	0.028	Bal.

Austenitic stainless steels are used because they show good corrosion and mechanical properties, particularly a high Ultimate Tensile Stress (UTS) and an excellent ductility. Figure 1.2 shows that the Yield Stress (YS) and UTS are ranging between 150-200 MPa and 500-700 MPa, respectively. Their associated ductility is as high as approximately 100%.

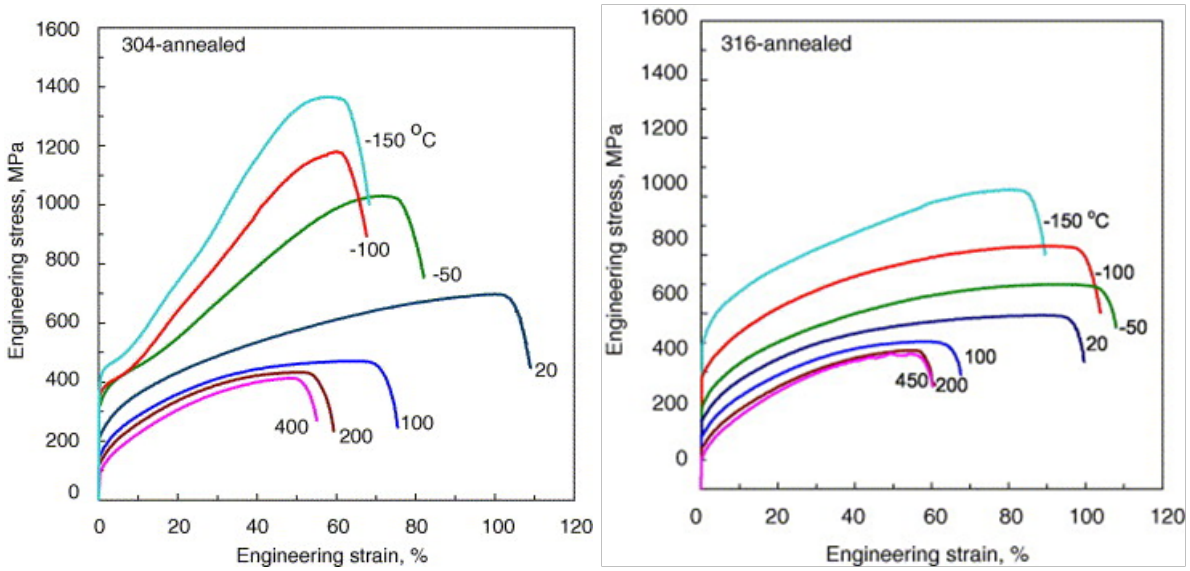

Figure 1.2: Temperature dependence of the engineering stress-strain curves for (a) annealed 304 stainless steel and (b) 316 stainless steel [1].

1.1.3. Operating conditions

Internals are submitted to an intensive neutron flux, strong enough to deteriorate their initial properties, especially when the irradiation takes place at temperatures between 300°C and 380°C. In fact, neutron irradiation can lead to major modifications of materials microstructure which induces a degradation of their mechanical properties and corrosion resistance. Features of operating conditions are gathered in Figure 1.3.

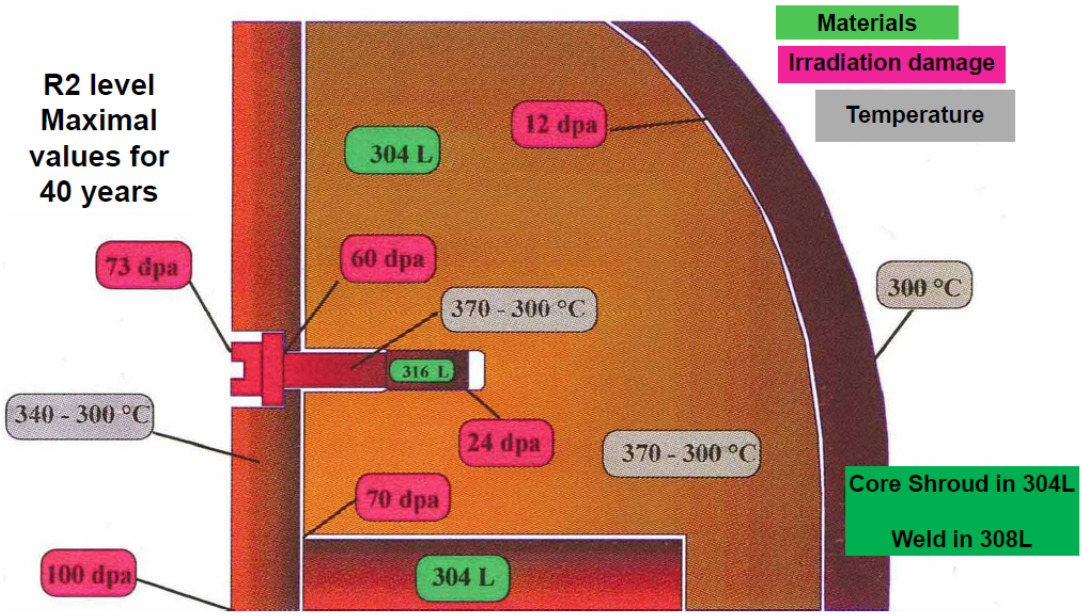

Figure 1.3: Operating condition features of bolts (316L) baffle and reinforcement (304L) and dose received for a 40 years' operating [2].

1.1.4. Irradiation damaging

The degradations are depending on fluence and operating temperature. These operating parameters are highly geometrically dependent and strongly vary within the pressure vessel. The effects of operating parameters are strongly locally dependent on internals and are reported in Table 1.2 in the

case of a 900 MWe PWR. The dose received corresponds to an operating time of 40 years. For certain pieces the displacement per atom (dpa) can reach 100 with an annual dose which can be more than 1 dpa per year.

Table 1.2: PWR Internals and irradiation conditions. Data for 900 MWe group of CP0 series.

Component	Material	Temperature (°C)	Dose at end-of-life (dpa)
Baffle bolts	Cold-worked 316	~300 to 370	up to ~80
Baffle plate	Solution annealing 304L	~300 to 350	up to ~80
Former		~300 to 370	up to ~50
Core barrel		~300	up to ~10
Core barrel longitudinal and circumf. Welds	308L welds	~300	up to ~10

Since irradiation leads to string modifications of the mechanical behaviour, it is necessary to investigate the effects of irradiation on the microstructure of the steel. The main effect of irradiation (under typical conditions experienced in a pressure vessel) is the creation of interstitial atoms and vacancies. These interstitial/vacancy pairs eventually recombine or diffuse independently to aggregate creating clusters of different sizes and nature.

The most sensitive parameters controlling irradiation microstructures and hardening are: radiation dose, irradiation temperature, initial states in term of dislocation densities and also a possible relation with the initial chemical composition of the material.

A typical observation of microstructure evolution of a damaged bolt reveals the presence of black dots, Frank loops and a few cavities or bubbles (see Figure 1.4). An important observation indicates that the initial dislocation network has completely disappeared [3]. The irradiation defect population is widely dominated by an interstitial Franck loops population which grows with the interstitial created under irradiation, and that is why we generate only the interstitial type in Chapter 4. These defects are formed at low irradiation doses and their size increasing with the dose until saturation at 5-10 dpa [4].

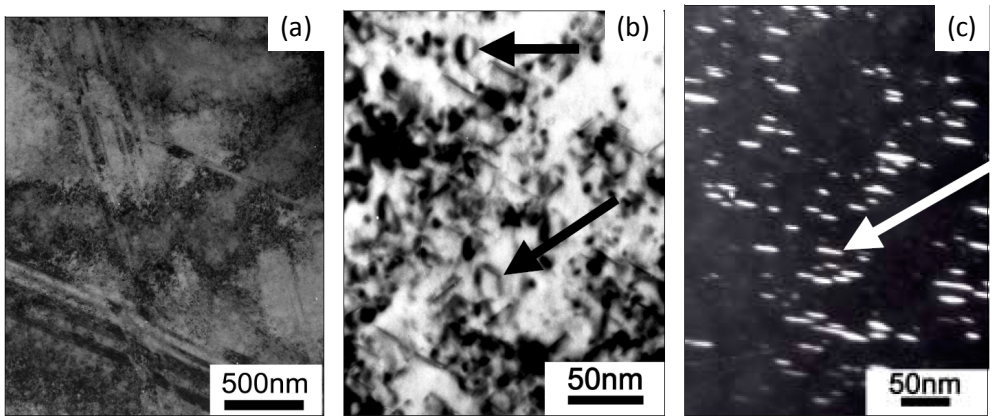

Figure 1.4: General aspect of observed microstructure for a cold-worked 316 (a). A typical microstructure of Franck loops (b) and faulted Franck loops (c). The cold-worked 316 observed here received a dose of 10 dpa at 375°C [5].

After irradiation at 5 dpa, the dislocation cells are no longer observed. Thus, once a cold-worked material has been irradiated, the initial dislocation network caused by cold working is progressively replaced by a Frank loops microstructure [3]. Nevertheless, it has been observed that Frank loops constitute a defect which can be absorbed by work hardening dislocations [6].

One of the most detrimental effects of irradiation on mechanical properties is the loss of fracture toughness due to irradiation embrittlement. Figure 1.5 compiles a set of many different experiments showing a strong decrease of the fracture toughness with neutron exposure. This is believed to be due to the interaction between dislocations and irradiation defects: *i.e.* cavities, Frank loops, bubbles.

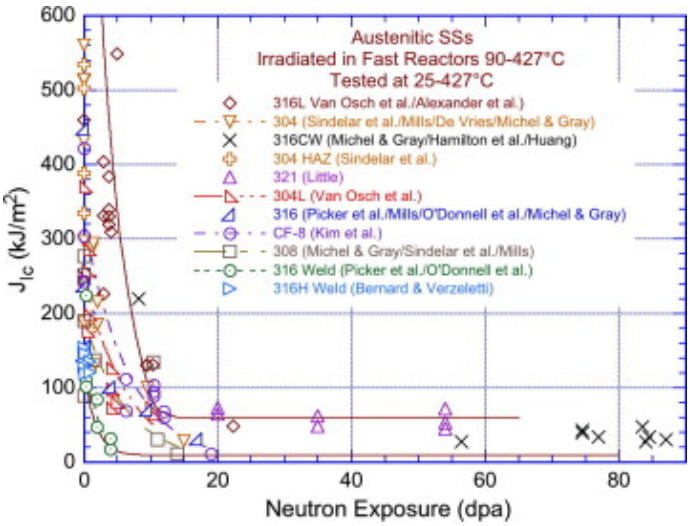

Figure 1.5: Effect of irradiation exposure on fracture toughness J_{IC} for austenitic stainless steels irradiated in fast reactors. Solid lines represent the scatter band for the fast reactor data on austenitic stainless steels [7].

The detailed interaction mechanisms between dislocations and defects, in particular Frank loops are not known very well, in particular, the interaction strength and nature.

1.2. Perform 60 project

The classical approaches to describe and predict radiation induced embrittlement are based on empirical formula that are obtained from fitting the results issued from testing specimens out of the surveillance capsules inserted in each reactor. If the lifetime of the reactors is to be extended, such an approach is not possible.

Utilities and companies that operate nuclear reactors need to quantify the ageing and the degradations undergone by essential structures to guarantee the safety and the reliability of operation plants. The material database needed to include these degradations in the design of new types of reactors, in order to extend the operating time, relies on long term irradiation time programs. The progress of knowledge in the physical understandings of the phenomena involving irradiation defects, and the computer increasing capacities generate tools to study deeply, and at multi-scales, the effects of irradiation on RPV and internals steels.

Based on the previous PERFECT Roadmap, the 4-year Integrating Project PERFORM 60 has the overall objective of developing multi-scale modelling tools aimed at predicting the combined effects of irradiation and corrosion on internals (austenitic stainless steels)and also improving existing ones on

RPV components (low-alloy bainitic steels). When possible, these tools are experimentally validated at each characteristic time or length scale. The PERFORM 60 will include:

1. An improved Fracture Toughness Module to produce an Advanced Fracture Toughness Module to model the irradiation degradation on RPV of PWR and Boiling Water Reactor (BWR) for a maximum duration of 60 years.
2. A platform of simulation tools to couple corrosion and irradiation effects on reactor internals in PWRs and BWRs. This platform is represented in Figure 1.6.
3. Experimental validation and model qualification using industrial plant data and results of existing or new experiments. In addition, other means of validation such as benchmarking with existing qualified calculation codes will be considered. A Users' Group will be established to test the modelling tools.

In order to achieve the above objectives, PERFORM 60 is constructed around three technical sub-projects

- RPV
- Internals and
- Users' Group

This PhD research thesis is part of the platform of Perform60 simulation tools, particularly devoted to studying the interaction of dislocation with Frank loop at the atomic scale, using Molecular Dynamics.

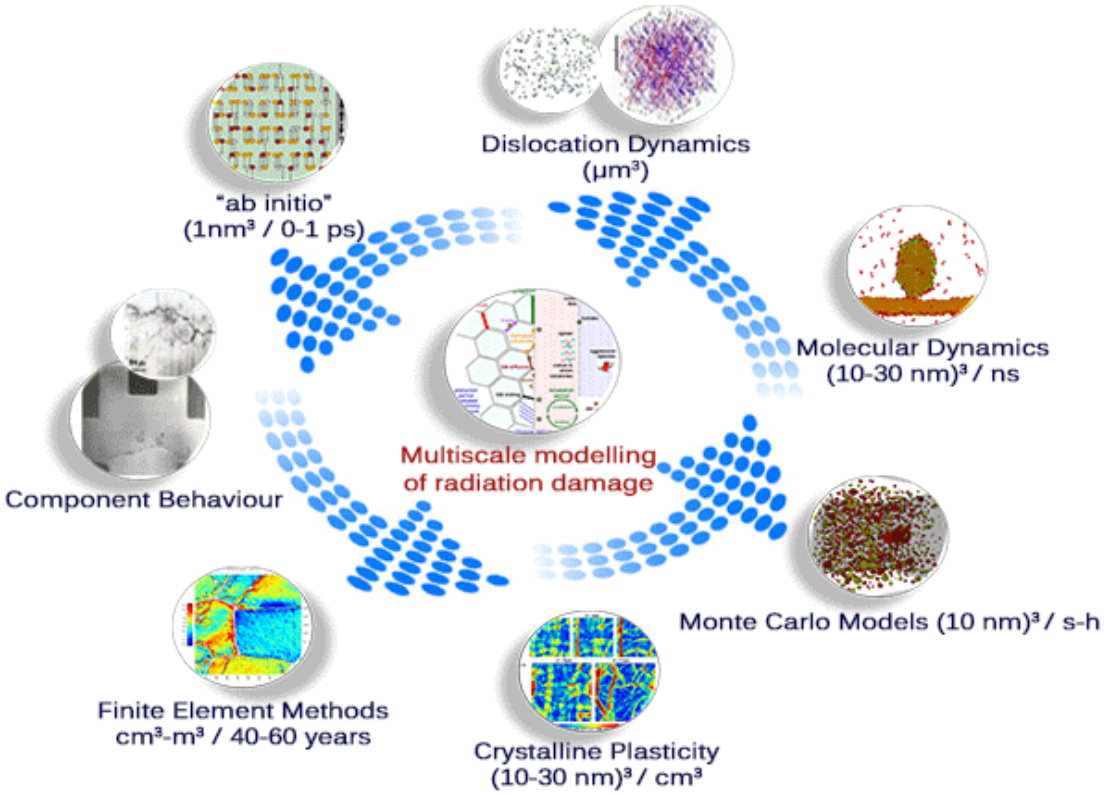

Figure 1.6: Modelling strategy at different atomic scales used in Perform60 project [8].

1.3. PhD research objectives

The purpose of this research thesis is characterized the behaviour of dislocations and their interactions with Frank loops in a Fe-Ni-Cr ternary alloy, considered as an austenitic steels model alloy, by using Molecular Dynamics simulations (MD). Explicitly, we aim at the following objectives:

1. Analyse the effects of alloying content (concentration in Ni and Cr) on the local value of Stacking Fault Energy (SFE);
2. Determine the alloy friction stress on dislocations;
3. Determine the effect of SFE and alloy friction stress on the dislocation dissociation in Fe-Ni-Cr alloy;
4. Establish the constitutive law of edge dislocation;
5. Identify the interaction between dislocation and Frank loops.

This study is organized in three parts. In the second chapter, we investigate the separation between the two dissociated partials as a function of the staking fault energy, elastic constants, applied stress and possible friction force.

The third chapter is devoted to the simulation of the gliding of an edge dislocation in a Fe-Ni_{10}-Cr_{20} alloy. The first objective of these simulations is to validate the potential in terms of staking fault energy and dissociation distance for various compositions. Then the following objective is to describe the mobility of the dislocation. The friction stress is evaluated for various temperatures and shear rates.

The fourth chapter aims at studying the detailed interactions between edge dislocations and Frank loops. Multiple parameters are tuned, such as the size of Frank loops, the temperature and the orientation of the Frank loops in the habit plane. Multiple interactions are also investigated in order to reproduce experimental results displaying clear bands, *i.e.* areas from which the defects have been annihilated.

References

- Chapter I -

[1] T. S. Byun, N. Hashimoto, K. Farrell, **Temperature dependence of strain hardening and plastic instability behaviors in austenitic stainless steels**, Acta Mater., 52 (2004) 3889-3899.
[2] C. Pokor, J.-P Massoud, G. Courtemanche, **Influence of the irradiation conditions on the microstructure, tensile properties and IASCC sensitivity of irradiated austenitic stainless steels: comparison between irradiations in experimental reactors and in pressurized water reactor**, PAMELA Perform-60 Workshop (2011).
[3] P. J. Maziasz, **Temperature dependence of the dislocation microstructure of PCA austenitic stainless steel irradiated in ORR spectrally-tailored experiment**, J. Nucl. Mater., 191-194 (1992) 701-705.
[4] C. Pokor, Y. Bréchet, P. Dubuisson, J.-P. Massoud, A. Barbu, **Irradiation damage in 304 and 316 stainless steels: experimental investigation and modeling. Part I: Evolution of the microstructure**, J. Nucl. Mater., 326 (2004) 19-29.
[5] C. Pokor, **Caractérisation microstructurale et modélisation du durcissement des aciers austénitiques irradiés des structures internes des réacteurs à eau pressurisée**, PhD thesis (2002) Institut National Polytechnique de Grenoble.
[6] H. Trinkaus, B. N. Singh, A. J. E. Foreman, **Segregation of cascade induced interstitial loops at dislocations: possible effect on initiation of plastic deformation**, J. Nucl. Mater., 251 (1997) 172-187.
[7] O. K. Chopra, A. S. Rao, **A review of irradiation effects on LWR core internals materials – Neutron embrittlement**, J. Nucl. Mater., 412 (2011) 195-208.
[8] http://**www.perform60.net/**.

Chapter 2. Including the friction stress in the theory of dislocation dissociation

The separation between partials in FCC (Faced Centered Cubic) alloys is known to be a function of the elastic constants and the SFE. In this work, we complete this classical picture by investigating three other effects. First we show that the direction of the applied stress component in the slip plane perpendicular to the Burgers vector induces an additional force on the partials. Depending on the value of the SFE, a critical value for this shear component leads to an infinite separation [1], which explains the deformation mechanism by a formation of extended stacking faults [2]. In alloys where the friction stress is not negligible, we show that the friction plays an important and complex role on dissociation, depending on the previous dislocation motion. This factor can be responsible for the discrepancy in the experimental measurement of the dissociation width. In all cases, we show that the effect of the friction stress vanishes as soon as the dislocation starts gliding in its slip plane. Finally, we show that the choice of effective shear modulus in elastically anisotropic materials constitutes an important feature in the modelling of the equilibrium dissociation width.

2.1. Introduction

The dislocation dissociation is an important feature in low SFE materials such as AISI 316 type austenitic stainless steels [3, 4]. The dissociation is supposed to be the controlling factor in the formation of twins and extended stacking faults [5, 6]. A large number of experimental investigations report on the activation of these mechanisms in the 316L steels [7, 8].

Recently, Byun [2] has investigated the role of the applied stress on the partial separation and shown that some stress components may be responsible for the spreading of stacking faults, affecting substantially the microstructure deformation.

In these investigations, an implicit assumption is made: the friction stress on the Shockley partials is considered to be negligible. In the case of pure FCC metals, this assumption is quite plausible, since the critical resolved shear stress measured on single crystals is very low. However, in industrial materials made harder by alloying, this assumption may be questionable.

In this research work, we are investigating theoretically the role of the applied stress as well as the friction stress on the dissociation spacing. Unlike the convention considered by Byun [2], we consider a configuration in which a stress tensor is applied to a crystal containing a slip system with a fixed Burgers vector and slip plane. The dissociation distance is studied as a function of the dislocation character, *i.e.* the angle made by the dislocation line and its Burgers Vector. The force balance includes the presence of a friction stress on every Shockley partial. For the sake of simplicity, we consider here the mathematical derivation of an elastically isotropic material,. Thus we then make an application on the case of the 316L steel and we discuss the effect of friction stress and the choice of the effective isotropic elastic constants on the dissociation width.

2.2. Force components

Let's consider a perfect dislocation with a line vector parallel to the $\vec{e}_r$ axis of a cylindrical coordinate system, incorporated in a Cartesian coordinate system as shown in Figure 2.1. The orthonormal

Cartesian axes coincide with the crystal axes: $\vec{e}_x = \frac{1}{\sqrt{2}}[\bar{1}10]$, $\vec{e}_y = \frac{1}{\sqrt{6}}[1\bar{1}2]$ and $\vec{e}_z = \frac{1}{\sqrt{3}}[111]$. The dislocation Burgers vector is $\vec{b} = \frac{1}{2}[\bar{1}10]$ and can be written as $\vec{b} = b\vec{e}_x$. The normal to the slip plane matches with the z-axis of our coordinate. The dislocation character refers to the angle ϑ between the dislocation line vector $\vec{e}_r$ and the Burgers vector. In order to study the influence of the applied stress tensor on the dissociation of a dislocation loop in a given slip system, the dislocation Burgers vector should be kept constant while the angle ϑ varies from 0 (screw dislocation) to 90° (edge dislocation). This change in the dislocation character differs from that considered by Byun [2], who fixed the dislocation line vector and considered a rotation of the Burgers vector in the slip plane, which leads to a rotation in comparison with the stress coordinates system. We believe that the Burgers vector of the slip system should be fixed in the crystal coordinate system for two reasons: Firstly (i) the direction of the Burgers vector cannot rotate freely since it must match with the dense crystallographic direction and secondly (ii) along a dislocation loop the Burgers vector is constant while the dislocation line vector varies.

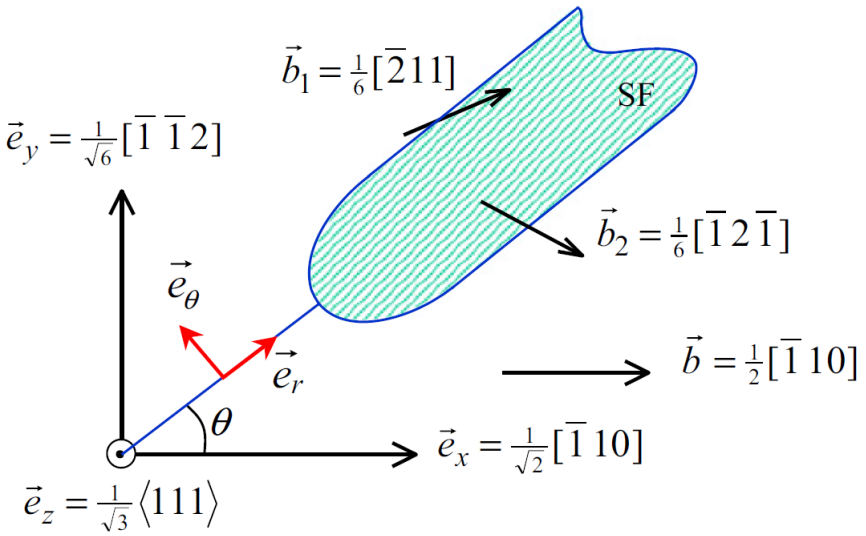

Figure 2.1: Configuration of the perfect and dissociated dislocation.

According to the elastic theory of dislocations [1], the perfect dislocation described above tends to dissociate into Shockley partials as sketched in Figure 2.1. We consider the dissociation plane to be the x-y plane. One leading partial is given by $\vec{b}_1 = [\alpha\ \beta\ 0]$, while the other partial is $\vec{b}_2 = [\alpha - \beta\ 0]$, where α equals ($a\sqrt{2}/4$), β equals ($a\sqrt{6}/12$) and a the lattice parameter. With these variables, the Burgers vector becomes $\vec{b} = [2\alpha\ 0\ 0]$. In order to investigate the effects of all stress components, we consider the general stress tensor Σ written in our Cartesian coordinate system:

$$\Sigma = \begin{pmatrix} \sigma_{xx} & \tau_{XY} & \tau_{XZ} \\ \tau_{XY} & \sigma_{YY} & \tau_{YZ} \\ \tau_{XZ} & \tau_{YZ} & \sigma_{ZZ} \end{pmatrix} \tag{2.1}$$

Given the configuration considered in Figure 2.1, the resultant forces per unit length on the leading partial is given by:

2.2. Force components

$$\vec{F}_1 = \left(\vec{F}_{\text{int}} - \gamma\vec{e}_\theta + \vec{F}_{PK,1} + \varepsilon_1 F_f\right)\vec{e}_\theta \tag{2.2}$$

This balance of forces is equivalent to the one present in [5], except that in this study, the force components are more detailed. The different forces appearing on the right-hand side are respectively: the interaction force with the trailing partial, the attractive force resisting to the expansion of the stacking fault, the Peach-Kœhler force [9] and the friction force per unit length: $F_f = b\tau_f$, where τ_f is the friction stress. ε_1 is a sign parameter ($\varepsilon_1 = \pm 1$) depending on the direction of motion of the leading partial. Equivalently: the effective stress on the trailing partial can be given as:

$$\vec{F}_2 = \left(\vec{F}_{\text{int}} + \gamma\vec{e}_\theta + \vec{F}_{PK,2} + \varepsilon_2 F_f\right)\vec{e}_\theta \tag{2.3}$$

Note that since the crystallographic nature of the two partials is different, there is no evidence that both friction forces are equal. However, for the sake of simplicity we consider that the difference between them is negligible. Projecting these forces on the $\vec{e}_\theta$ axis and considering that the amplitude of the interaction between the partials is the same, we get:

$$F_1 = \vec{F}_1 \cdot \vec{e}_\theta = F_{int} - \gamma + F_{PK,1} + \varepsilon_1 F_f \tag{2.4}$$

for the leading partial and:

$$F_2 = \vec{F}_2 \cdot \vec{e}_\theta = -F_{int} + \gamma + F_{PK,2} + \varepsilon_2 F_f \tag{2.5}$$

for the trailing partial. Using the classical formulas for the Peach-Kœhler force [9], one finds:

$$F_{PK,1} = \alpha\tau_{xz} + \beta\tau_{yz} \tag{2.6}$$

and

$$F_{PK,2} = \alpha\tau_{xz} - \beta\tau_{yz} \tag{2.7}$$

As expected, only the stress component parallel to each Burgers vector component contributes to the effective force on every partial. On the other hand, the interaction force per unit length between the parallel partials can be computed using Eqn. (5.17) of Hirth and Lothe textbook [5], which was first developed by Nabarro. In our case, we have:

$$F_{int} = \frac{G}{2\pi d}\left[\left(\alpha^2 + \beta^2\right)\cos^2\theta - \beta^2 + \frac{\alpha^2 \sin^2\theta - \beta^2\cos^2\theta}{1-\nu}\right] \tag{2.8}$$

where G is the shear modulus and d the spacing between partials. Since α^2 and β^2 equal respectively ($b^2/4$) and ($b^2/12$), F_{int} can be reduced to:

$$F_{int} = \frac{Gb^2}{24\pi(1-\nu)d}\left(2 + \nu - 4\nu\cos^2\theta\right) \tag{2.9}$$

2.3. Equilibrium at zero applied stress

When τ_{xz} and τ_{yz} vanish, one can identify the static dissociation distance. The energy of the dissociated dislocation *E(d)* must exhibit a minimum for the well-known equilibrium spacing $d = d_0$, which is given by:

$$d_0 = \frac{2+\nu-4\nu\cos^2\theta}{24\pi(1-\nu)}\frac{Gb^2}{\gamma} \tag{2.10}$$

If every partial is shifted away from the other one by *dx*, the associated change in energy is given by $\Delta E = F_1 dx - F_2 dx$. Since at equilibrium ΔE must vanish, we have: $2F_{int} - 2\gamma + \varepsilon_1 F_f - \varepsilon_2 F_f = 0$. The parameters ε_i depend on the direction of motion of every partial dislocation towards the equilibrium position. Two important cases can be distinguished. If the partials move away from each other towards the equilibrium dissociation distance d_0, then ε_1 is equal to –1 and ε_2 is equal to +1 and the separation distance reached is:

$$d_- = \frac{2+\nu-4\nu\cos^2\theta}{24\pi(1-\nu)}\frac{Gb^2}{\gamma+F_f} \tag{2.11}$$

In the other case where the dissociation tends to shrink from a larger dissociation distance, partials move towards each other and ε_1 is now equal to +1 and ε_2 is –1. We then have:

$$d_+ = \frac{2+\nu-4\nu\cos^2\theta}{24\pi(1-\nu)}\frac{Gb^2}{\gamma-F_f} \tag{2.12}$$

The presence of a friction force causes a degeneration of the dissociation distance depending on the direction of motion of the partials.

2.4. Dissociation under applied stress

Table 2.1: Displacement scenarii for each partial and associated value of $\varepsilon_{1,2}$ and/or $F_{1,2}$.

Partial	Condition	$E_{1,2}$	Action
1	$F_1^{nf} \succ F_f$	$\varepsilon_1 = -1$	Displ. Twds $\vec{e}_\theta$
	$-F_f \prec F_1^{nf} \prec F_f$	$F_1 = 0$	Partial 1 pinned
	$F_1^{nf} \prec -F_f$	$\varepsilon_1 = +1$	Displ. Twds $-\vec{e}_\theta$
2	$F_2^{nf} \succ F_f$	$\varepsilon_2 = -1$	Displ. Twds $\vec{e}_\theta$
	$-F_f \prec F_2^{nf} \prec F_f$	$F_2 = 0$	Partial 2 pinned
	$F_2^{nf} \prec -F_f$	$\varepsilon_2 = +1$	Displ. Twds $-\vec{e}_\theta$

Only the applied shear components τ_{xz} and τ_{yz} contribute to the force on the partials dislocations. The sum of the two forces corresponds to the net force F_{tot} on the perfect dislocation, *i.e.* on the ensemble of the two partials. Depending on the sign and amplitude of the non-friction part of F_1 and F_2, namely

$$F_1^{nf} = F_{int} - \gamma + F_{PK,1} \tag{2.13}$$

$$F_2^{nf} = -F_{int} + \gamma + F_{PK,2} \tag{2.14}$$

3 possible scenarii per partial can occur: it can move backward, forward or be pinned (see Table 2.1). In order to evaluate the equilibrium dissociation distance, a simple algorithm is used.

1) Set the initial partials distance to the equilibrium distance at zero applied stress without friction force (using Eqs. (2.11) or (2.12) with $F_f = 0$);
2) Calculate non friction parts F_1^{nf} and F_2^{nf} of forces acting on both partials (using Eqs. (2.13) and (2.14));
3) Calculate ε_1 and ε_2 and, eventually, F_1 and F_2 (using Table 2.1);
4) Calculate net forces F_1 and F_2 on both partials (using Eqs. (2.4), (2.5), (2.6), (2.7) and (2.9));
5) Move both partials by a small increment $\delta x_{1,2} = F_{1,2}/\tau_0$ where τ_0 is a constant of about 1 GPa;
6) Go to 1) until the distance between the partials is constant ($\delta d/d < 10^{-5}$).

2.5. Discussion

We discuss our results in the light of the applications on the 316L steel, which is of technological interest in the nuclear industry. The single crystal elastic constants are $C_{11} = 210$ GPa, $C_{12} = 130$ GPa, $C_{44} = 120$ GPa [10]. The application of our theoretical results on this material faces two difficulties: (i) the material is highly anisotropic and (ii) the SFE varies substantially between the different alloys from 10 to 40 mJ/m² [4]. For the sake of simplification, we treat three sets of effective isotropic elastic constants: the Voigt average [11] ($G = 88$ GPa, $\nu = 0.26$), Reuss average [12] ($G = 60$ GPa, $\nu = 0.32$) and the Scattergood and Bacon average [13, 14] ($G = 61$ GPa, $\nu = 0.4$).

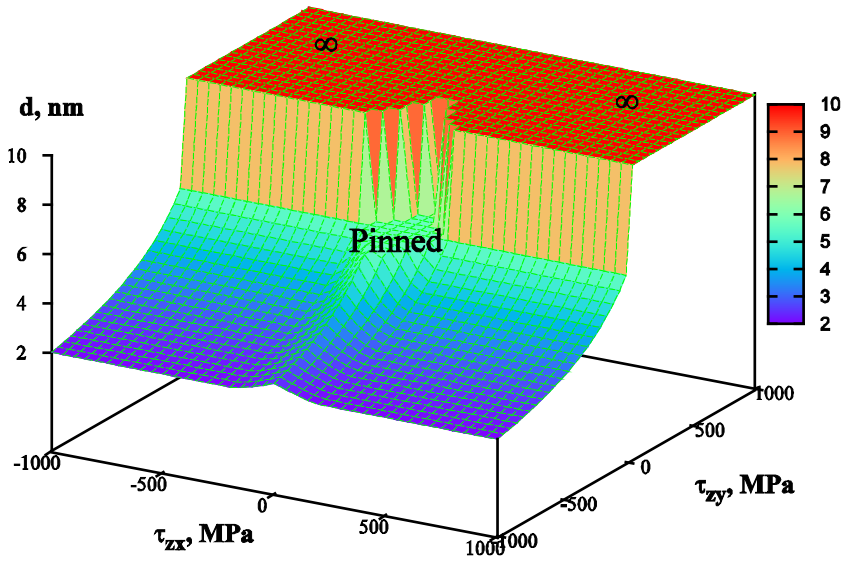

Figure 2.2: Typical surface of dissociation distance between both partials for different values of stresses in the (τ_{xz}, τ_{yz}) plane. Friction force has been set to τ_f=90 MPa ($F_f=b\tau_f$) [15]. Voigt average for the effective isotropic elastic constants has been considered (see text).

In the absence of applied stress and depending on the considered effective elastic constants, we get different values for the friction-free material concerning the screw ($\theta = 0°$) and edge ($\theta = 90°$) perfect dislocations. The computation results are given in Table 2.2 for the two extreme values of the SFE.

We can clearly see that depending on the average considered, the dissociation distance for the screw dislocation varies by almost a factor of two, while that of the edge dislocations changes only by 30%. Increasing the SFE by a factor of 4 causes the dissociation distance to decrease by a factor of 4. Depending on the material and the elastic constants to be considered, the dissociation of screw dislocations varies from 1.7 to 11.8 nm, while that of edge dislocations varies from 4.2 up to 21.9 nm. In the presence of applied stress, the stress component parallel to the perfect Burgers vector, *i.e.* τ_{xz} in our configuration, contributes to a global motion of the two partials in the same direction. However, the presence of a shear stress component perpendicular to the perfect Burgers vector leads to a change in separation distance. In the configuration of Figure 2.1, a negative value of τ_{yz} enhances the effect of the SFE, while a positive value of τ_{yz} causes the stacking fault to extend. Escaig stress has to be introduced right at the time when we defined it [16]. But in this study, we are not considering the effect of curvature.

Table 2.2: Equilibrium dissociation distance d_0 (nm) for friction-free 316L with a SFE of 10 and 40 mJ/m^2 as a function of the average elastic constants and the dislocation character in the absence of applied stress.

d_0(nm)	Voigt	Reuss	Scattergood andBacon
Screw (10 mJ/m²)	11.8	7.5	6.6
Edge (10 mJ/m²)	21.9	16.7	19.9
Screw (40 mJ/m²)	3.0	1.9	1.7
Edge (40 mJ/m²)	5.5	4.2	5.0

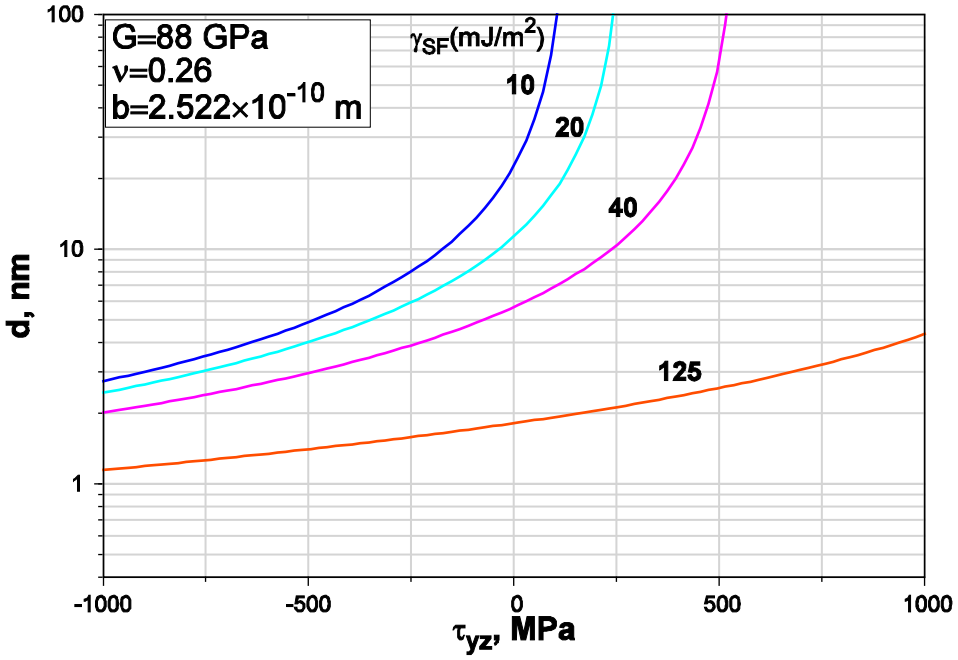

Figure 2.3: Partial separation distance versus stress component τ_{yz} for different SFE values γ_{SF}. Voigt average for the effective isotropic elastic constants has been considered.

This algorithm presented above leads to the evaluation of the dissociation distance as a function of τ_{xz} and τ_{yz} (see Figure 2.2). The friction force $F_f = b\tau_f$ with $\tau_f = 90\,\mathrm{MPa}$ has been used, complying with the MD simulations performed on a Fe-Ni-Cr alloy [15].

Depending on the applied stress, three domains are observed in:

1) $F_1 = F_2 = 0$ (in a diamond shaped domain delimited by $\left|\alpha\tau_{xy} + \beta\tau_{yz}\right| < b\tau_f$ and $\left|\alpha\tau_{xy} - \beta\tau_{yz}\right| < b\tau_f$, both partials are pinned by the friction force and remain thus immobile;
2) one (or two) partial(s) is (are) pinned and the dissociation distance tends to an equilibrium value;
3) one (or two) partial(s) is (are) unpinned and the dissociation distance diverges to infinity.

In the case when both partials are moving in the same direction (thanks to the contribution of τ_{xz}), we have $\varepsilon_1 = \varepsilon_2 = \pm 1$. Thus, at dynamical equilibrium, the dissociation distance is such that the force acting on both partials is equal: $F_1 = F_2$, leading to the dissociation distance:

$$d_\tau = \frac{2 + \nu - 4\nu \cos^2\theta}{24\pi(1-\nu)} \frac{Gb^2}{\gamma - \beta\tau_{yz}} \tag{2.15}$$

It is remarkable that the separation d_τ between partials becomes independent of the friction stress and the τ_{xz} shear stress component. Moreover, for a critical value $\tau_{yz,c} = \gamma/\beta$, the partials separation becomes infinite for screw dislocations as well as for edge dislocations. This conclusion is different from that drawn by Byun [2], who stated that the dissociation distance diverges only for screw dislocations. This difference is due to (i) the evolution of the stress state with the dislocation line orientation: in Byun's paper, the dislocation line was fixed whereas the orientation of the Burgers vector varied (which is a surprising choice); and, (ii) Byun only considered τ_{yz} to be non-zero, whereas it has been shown here that τ_{yz} contributes to the partials divergences.

The evolution of the dissociation distance versus the shear stress component τ_{yz} is represented in Figure 2.3 for different values of SFE. For the 316L referenced material, $\tau_{yz,\,c}$ varies between 100 MPa (for $\gamma = 10\ \mathrm{mJ/m^2}$ and 500 MPa (for $\gamma = 40\ \mathrm{mJ/m^2}$). For Nickel ($\gamma = 125\ \mathrm{mJ/m^2}$), it is not possible to evaluate $\tau_{yz,\,c}$ in the stress range [-1000:1000]. As discussed by Byun [2] these stress levels can be easily met during the deformation of austenitic steels [3] and are frequently reached in mechanical tests [4, 17]. In this case, partial dislocations are expected to move separately, thus, inducing extended faults and facilitating twin formations.

2.6. Conclusions

A theoretical analysis of the effect of the stress on the separation distance of partial dislocations has been investigated. The results obtained in this article are summarized as follows:

1) A global expression has been established gathering the different forces exerted on dislocation partials. The stress acting on the dislocation is introduced by using the Peach-Khœler formula. The partials experience attractive and repulsive forces, which are introduced via the SFE, the Nabarro Formula and the Peach-Khœler formula.
2) It is shown that only two stress components τ_{xz} and τ_{yz} affect the dislocation: τ_{xz} leads to the movement of the whole dislocation whereas τ_{yz} influences the dissociation distance.
3) Above a critical stress τ_{yz}, which depends only on the SFE, it is found that the distance between the two partials diverges, whatever the dislocation type (edge or screw).
4) The friction stress on partial dislocations is found to affect strongly the dissociation width. Depending on the previous motion of the dislocation, this stress may retain the partials far from their equilibrium spacing.

References

- Chapter II -

[1] J. B. Baudouin, G. Monnet, M. Perez, C. Domain, A. Nomoto, **Effect of the applied stress and the friction stress on the dislocation dissociation in face centered cubic metals**, Materials Letters, 97 (2013) 93-96.
[2] T. S. Byun, **On the stress dependence of partial dislocation separation and deformation microstructure in austenitic stainless steels**, Acta Mater., 51 (2003) 3063-3071.
[3] K. Lo, C. Shek, J. Lai, **Recent developments in stainless steels**, Mater. Sci. Eng., 65 (2009) 39-104.
[4] X. Li, A. Almazouzi, **Deformation and microstructure of neutron irradiated stainless steels with different stacking fault energy**, J. Nucl. Mater., 385 (2009) 329-333.
[5] J. P. Hirth, J. Lothe, **Theory of Dislocations**, Kringer Publishing Company, (1982).
[6] D. Hull, D. J. Bacon, **Introduction to Dislocations**, Butterworth-Heineman, (2001).
[7] X. Feaugas, **On the origin of the tensile flow stress in the stainless steel AISI 316L at 300 K: back stress and effective stress**, Acta Mater., 47 (1999) 3617-3632.
[8] E. Lee, T. S. Byun, J. Humm, M. Yoo, K. Farrell, L. Mansur, **On the Origin of deformation microstructures in austenitic stainless steel: Part I-Microstructures**, Acta mater., 49 (2001) 3269-3276.
[9] M. Peach, J. S. Kœhler, **The Forces Exerted on Dislocations and the stress Fields Produced by Them**, Phys. Rev., 80 (1950) 436-439.
[10] M. C. Mangalick, N. F. Fiore, **Orientation Dependence of Dislocation Damping and Elastic Constants in Fe-18Cr-Ni Single Crystals**, Transactions of the Mettalurgical Society of AIME, 242 (1968) 2363-2364.
[11] W. Voigt, **Lehrbuch der Kristalphysik**, Teubner, 1928.
[12] A. Reuss, **Berechnung der Fliessgrenze von Mischkristallen auf Grund der Plastizitäsbendingung für Einkristalle**, Z. Angew Math. Mech., 9 (1929) 49-58.
[13] R. O. Scattergood, D. J. Bacon, **Dislocation shear loops in anisotropic crystals**, Phys. Status. Solidi. A, 25 (1974) 395-404.
[14] D. J. Bacon, In : B. A. Bilby, K. J. Miller, J. R. W. Jr. editors, **Fundamentals of deformation and fracture**, Eshelby memorial symposium. Cambridge, England; Sheffield, England: Cambridge University Press; 1985.
[15] G. Bonny, D. Terentyev, R. C. Pasianot, S. Poncé, A. Bakaev, **Interatomic potential to study plasticity in stainless steels: the FeNiCr model alloy**, Modelling Simul. Mater. Sci. Eng., 19 (2011) 085008.
[16] B.Escaig, **Sur le glissement dévié des dislocations dans la structure cubique à faces centrées**, J. Phys., 29 (1968) 225-239.
[17] T. S. Byun, N. Hashimoto, K. Farrell, **Temperature dependence of strain hardening and plastic instability behaviors in austenitic stainless steels**, Acta Mater., 52 (2004) 3889-3899.

Chapter 3. Structure and mobility of an edge dislocation in an Fe-Ni_{10}-Cr_{20} alloy

The plasticity of pure FCC metals has been investigated at many different scales over the last century. Recent advances in simulation techniques at the atomic scale have provided an important insight into the detailed mechanisms at the origin of dislocation dissociation, motion and interaction (see the review of Bacon et al. [1]). Molecular Dynamics (MD) is a fairly well-adapted simulation technique to study these phenomena because it provides insights into both the dislocation structure (dissociation) and the critical stress (Peierls stress) necessary to move the dislocation. With this technique, the friction stress of the dislocation can also be estimated in a given range of strain rates and temperatures. Extensive MD studies on copper [2], aluminium [3] led to the determination of an accurate constitutive law for the dislocation motion in pure metals.

However it is known from experiments that alloying elements play an important role on these mechanisms; *e.g.* it is well-known that alloying elements hinder the dislocation motion by interacting with the dislocation core, inducing a pinning and/or friction force. In austenitic stainless steels, the effect of alloying element is even more pronounced since their fraction is very high (more than 30%).

To date, a few binary potentials have been proposed. Meyer [4] originally proposed an Embedded Atom Method (EAM) Fe-Ni potential. However, this potential states that austenite is stable for more than 55 at% Ni, in contradiction with experimental findings reporting much lower Ni concentrations. To go beyond this difficulty, Becquart and Domain [5] proposed a new Fe-Ni potential based on state-of-the-art interatomic functions for Fe [6, 7] and Ni [8]. This potential led to a more reasonable ferrite/austenite relative stability (austenite is stable from 25 at% of Ni) and reasonable estimations of lattice parameters and stacking fault energies.

To our knowledge, no theoretical approach at the atomic scale is able to provide any quantitative results, and associated detailed mechanisms, concerning the effect of more than one alloying element on the stacking fault energy, the pinning force and the friction force in austenitic stainless steels.

An interatomic potential for austenitic Fe-Ni-Cr alloys has been recently proposed by Bonny et al [9]. It has been built to fit both elastic constants and stacking fault energy for the target composition Fe-Ni_{10}-Cr_{20} that mimics stainless 316L steel. It has been validated on Ni and Cr compositions ranging from 0 to 30%. The aim of this chapter is to use this potential to (i) quantify the effect of Ni and Cr on stacking fault energy for various temperatures; (ii) investigate the effect of temperature and shear rate on the dislocation dissociation distance; and, (iii) propose a constitutive law accounting for temperature and shear rate for the target composition.

This chapter will be divided in four parts. Section 1 will focus on the simulation techniques and the generation of the simulation box. Section 2 is devoted to the bulk properties of the alloy crystals. Section 3 will present the effect of alloying elements, temperature and strain rate on the dislocation structure. Section 4 will deal with the effect of temperature and strain rate on the friction stress. This chapter will be concluded by a short discussion on the simulation results that have been found and their potential insertion in a multiscale modeling approach of plasticity of austenitic steels.

3.1. Temperature and composition dependence of Stacking Fault Energy

Stacking fault energy is a key parameter to understand the plasticity of FCC metals at the atomic scale. It is then necessary to compare the experimental dislocation structure (dissociation distance) to the structure obtained with the ternary Fe-Ni-Cr potential. The aim of this section is to present a brief summary of experimental stacking fault energy dependence with composition and temperature.

Brown and Thölen [10] proposed a method to measure SFE from the size of triple junction observed in (Transmission Electron Microscope) TEM. The triple junctions are assimilated to circles, for which the radius depends on SFE. An example of triple junction is represented in Figure 3.1. The intrinsic SFE is determined with the measurement of the radius *y* of the circle inscribed in the extended node. The relation proposed by Brown and Thölen [10] connects the SFE γ to the radius *R* of the external curvature of the dislocation and the radius *y* of the inscribed circle:

$$\frac{\gamma y}{\mu b_p^2} = 0.055\frac{(2-\nu)}{(1-\nu)} - 0.06\left(\frac{\nu}{(1-\nu)^2}\right)\cos 2\alpha + \left[0.018\left(\frac{2-\nu}{1-\nu}\right) + 0.036\left(\frac{\nu}{1-\nu}\right)\cos 2\alpha\right]\log_{10}\frac{R}{\in} \quad (3.1)$$

where b_p is the partial Burgers vector of the dislocation, α is the angle of the dislocation character, ν Poisson's ratio and ϵ the cut off distance related to the core radius of the dislocation. Note that this measurement cannot be conducted above ~300°C, due to the dislocation annealing.

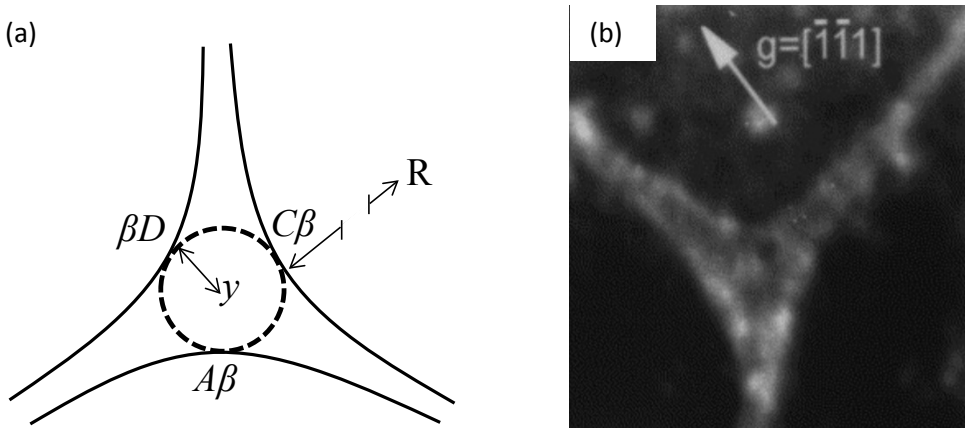

Figure 3.1: Extended dislocation junction. (a) diagram based on Thompson notation where *y* is the radius inscribed in the triple junction and (b) example of triple junction observed in TEM on a 310s stainless steel (from [11]).

The compilation of SFE proposed by Remy *et al.* [12] reveals that SFE increases with temperature in FCC systems (including many austenitic steels). Note that Saka *et al.* reported an opposite trend for pure Ag [13]. The results of Lecroisey *et al.* [14] are gathered for Fe-Cr_{16}-Ni_{13} and Fe-$Cr_{17.8}$-Ni_{14} compositions and of Latanasion *et al.* [15] for Fe-Cr_{18}-Ni_{11} and Fe-Cr_{19}-Ni_{16} and are represented in Figure 3.2.

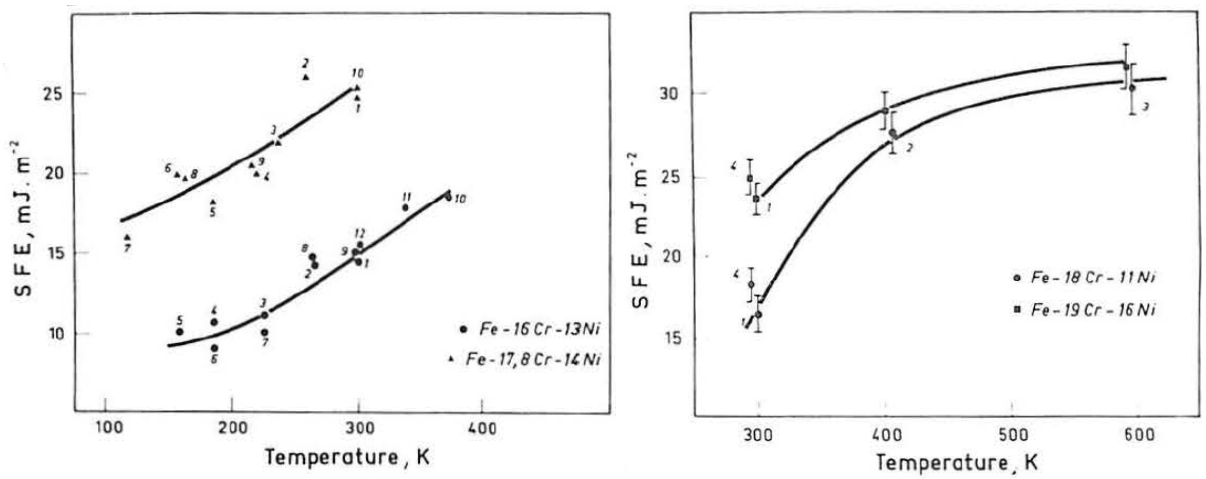

Figure 3.2: Experimental study on the variation of SFE depending on temperature for four Fe-Ni-Cr compositions (from [12], which is itself based on data obtained by [14] and [15]).

Rémy and Pineau [12] proposed an explanation for this temperature dependence of SFE by considering the stacking fault as an infinite plane of HCP (Hexagonal Close-Packed) structure with a thickness of 2 inter-plane distances. Based on values of entropy change between FCC and HCP, they proposed an expression for the temperature dependence of the SFE. For austenitic steel, they assumed that the entropy change between the FCC and HCP phase was weighted by the composition of the steel. They found that SFE does increase with temperature in all investigated steels but their predicted slope, $d\gamma/dT$, did not fit with experiments. Moreover no explanation on the role of alloying elements on SFE was proposed.

In Figure 3.2, we can observe a saturation of SFE with temperature from 400 K. Latanasion *et al.* [15] suggested that a segregation of solute atoms on partial dislocations could explain this saturation by pinning both partials and making thus the measure of SFE irrelevant.

Rhodes *et al.* [16] investigated the effect of Ni and Cr content on SFE of austenitic stainless steels based on the method developed by Brown and Thölen [10]. They observed an increase of SFE with alloying element content, as a general trend. They also reported a more complex dependence for higher alloying element contents. Their major results are reported in Figure 3.3. These results are in quantitative agreement with the results obtained by Remy *et al.* [12].

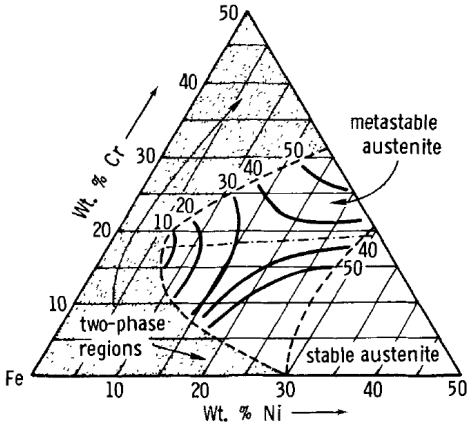

Figure 3.3: Fe-Ni-Cr ternary diagram showing the SFE dependence in Ni and Cr within the metastable austenitic phase domain [16].

From the theoretical point of view, Miodownik estimated the SFE of Fe-Ni_x-Cr_y alloys based on thermodynamic calculations. These calculations have been used by Bonny *et al.* to validate their MD FeNiCr potential. Figure 3.4 compares the SFE obtained by Miodownik and by Bonny. The composition dependence of SFE is also well-reproduced in accordance with Cr and Ni content. Moreover, the saddle around Fe-Ni_{45}-Cr_{30} is correctly reproduced. Note that the saddle shape energy landscape was also observed experimentally.

Moreover, around the target composition, Fe-Ni_{10}-Cr_{20}, thermodynamic calculations (23 $mJ.m^{-2}$ [17]) and Bonny's potential (20 $mJ.m^{-2}$ [9]) compare well with experimental results (10-30 $mJ.m^{-2}$ [18, 19, 20]).

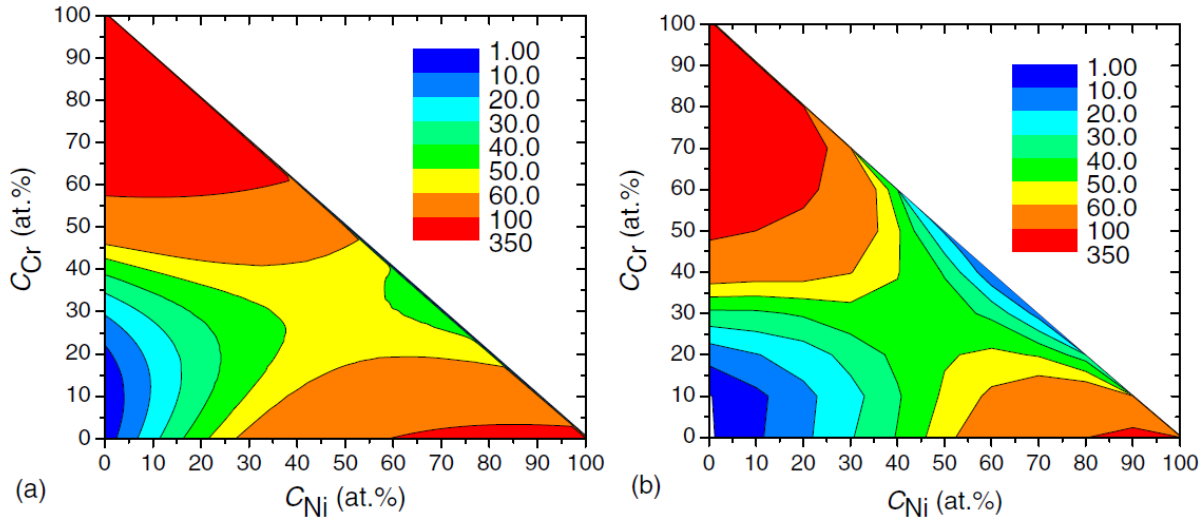

Figure 3.4: Composition dependence of SFE ($mJ.m^{-2}$) obtained from thermodynamics calculations [17] (a) and from the EAM Fe-Ni-Cr potential used in this study (b) [9] (from ref. [9]).

These experimental and theoretical results will constitute a reference for our investigation of temperature and composition dependence of SFE (detailed in section 3.4.3.).

3.2. Constitutive law: previous models

This chapter aims at proposing a constitutive law associated to Bonny's EAM potential for the target composition Fe-10Ni-20Cr, which is supposed to mimic the 316L stainless steel. Different models of constitutive laws can be used to describe the stress and temperature dependence of the dislocation velocity. An overwhelming quantity of models has been proposed in the literature. However, in the framework of this chapter, we decided to focus on the most generic laws, namely the power law and thermo-mechanically activated law.

One of the most generic laws based on experimental results establishes a linear relationship between the logarithm of the strain-rate (or dislocation velocity) and the logarithm of the applied stress. This is the so-called power law proposed by many authors (see for example the textbook of Hull and Bacon [21]):

$$\frac{v}{v_0} = \left(\frac{\tau}{\tau_0}\right)^n \tag{3.2}$$

where v is the velocity, τ is the applied stress, τ_0 and v_0 are rescaling factors such that $v=v_0$ when $\tau=\tau_0$ and n is a constant which is supposed to be affected by temperature. This law is purely empirical and is based on multiple empirical results conducted on different materials, from pure metals to ionic compound, but does not imply any effects of dislocation motion. Note that eq. (3.2) is purely empirical and provides no physical explanation on the mechanism of dislocation motion.

Another type of constitutive law describes gliding as a thermo-mechanically activated process. In this case, the thermally activated motion is taken into account by introducing an activation barrier ΔH and the temperature T. In general, this constitutive law is formulated as:

$$v = v_0 \exp\left(\frac{-\Delta G}{k_b T}\right) \tag{3.3}$$

Where the activation enthalpy ΔG can be lowered by applying a stress τ. The activation volume V can be obtained from the relation:

$$V = \frac{k\ T\partial \ln \dot{\varepsilon}}{\partial \tau} \tag{3.4}$$

When the activation volume is constant, we may write:

$$\Delta G = \Delta G_0 - \tau V = (\tau_0 - \tau)V \tag{3.5}$$

where τ_0 is a rescaling parameter and V is the activation volume. This last parameter can be obtained from mechanical tests performed at constant temperature and constant strain rate.

From a theoretical point of view, when the activation volume is supposed to be a constant parameter, it is neither affected by temperature nor by strain rate. However, many experimental studies pointed out a temperature and a strain rate dependence of the activation volume.

An example of determination of activation volume has been conducted on 316L stainless steel by Lee *et al.* [22]. Usually, the activation volume data are normalized by b^3, where b is the Burgers vector.

Concerning the activation enthalpy ΔG, both experimental and modeling results (see for example [22] and [23]) reveal a non-linear decrease of the activation energy with stress (which is connected to a non-constant activation volume). An example of determination of the activation energy has been proposed by Rodney on aluminum by MD [23]. Note that on a limited stress domain, the activation volume can be considered as constant. Interestingly, Follansbee [24] proposed a hybrid model (power law and thermo-mechanical law) to describe the experimental results of Clauss [25] on different stainless steels.

The aim of this chapter is to establish a constitutive law able to describe the stress response of an edge dislocation submitted to different strain rates at different temperatures in the ternary Fe-Ni_{10}-Cr_{20} alloy. Based on our simulation results, (a) a power law and (b) a thermo-mechanically activated law will be proposed to describe our results (see section 3.6.4.).

3.3. Simulation techniques, box and conditions

Any Molecular Dynamics simulation starts with the definition of the initial state: positions, velocities and types of all atoms. To study the structure and mobility of dislocation, one needs to introduce a dislocation, apply appropriate boundary conditions and visualize the dislocation structure.

3.3.1. Insertion of the edge dislocation

The simulation box is oriented along $[110]$ (*x*-axis), $[1\,\bar{1}\,\bar{2}]$ (*y*-axis) and $[1\,\bar{1}\,1]$ (*z*-axis) (see Figure 3.5). The box is cut in two equal parts along the $(1\,\bar{1}\,1)$ plane, which is called the slip plane. In this work, two methods for the generation of the dislocation were used: the Osetsky method [26] and the Rodney method [27].

The Osetsky method consists in building two half samples: an upper part with N planes and a lower part with N-1 planes. If we consider L_N the initial length of the half-crystal which contains N planes and L_{N-1} the equivalent length of the other half-crystal, thus the two crystals have to be scaled in such a way that the final length of the crystal is $L_b = (L_N + L_{N-1})/2$. In this way the half-crystal with the length L_N is in compression whereas the other half-crystal is in tension, so that the whole crystal is submitted to no net internal stress.

The other method, that is called the Rodney method, consists in deleting one half-plane perpendicular to Burgers vector direction. Then, the upper and lower parts of this crystal are rescaled in order to have a final length $L_b = (L_N + L_{N-1})/2$. That way, the tension and the compression parts are balanced.

For both methods, energy is finally minimized and atom positions are relaxed thanks to a quench algorithm, leaving thus the dislocation split into two partials. The main difference between these two methods is the initial Burgers circuit generated in the simulated cell just before the minimization. In the case of the Osetsky method, the Burgers circuit is spread over the whole box whereas it is concentrated in the center with the Rodney method. Due to the friction that operates on both partials during minimization, the Osetsky method leads to a dissociated dislocation where the two partials are beyond their equilibrium position (distance $d_+ > d_0$), whereas the Rodney method generates a dissociated dislocation, for which the two partials are below their equilibrium position (distance $d_- < d_0$).

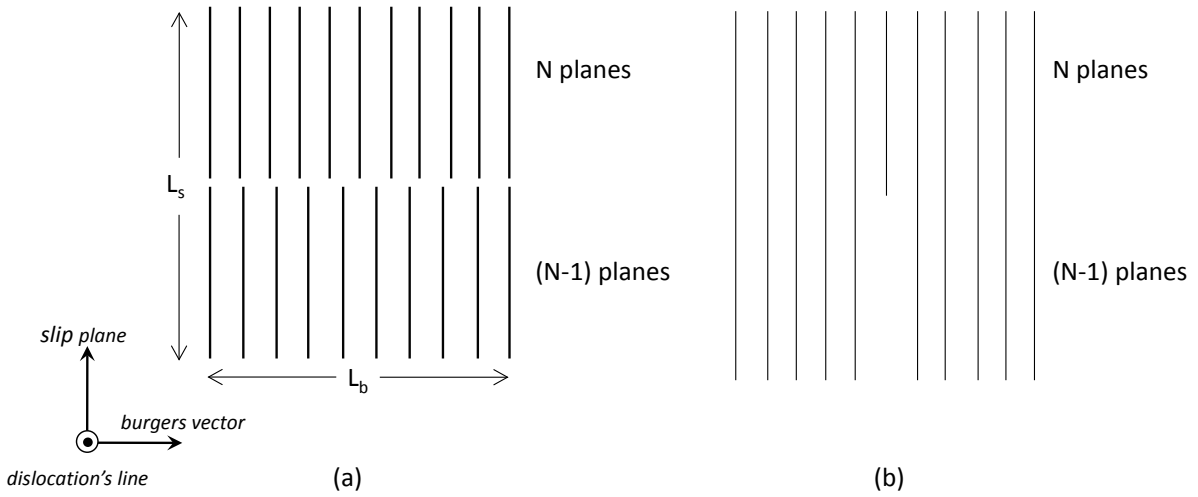

Figure 3.5: Construction of an edge dislocation with two half-crystals with a different number of *y-z* planes in the case of the method developed by Osetsky *et al.* [26] (a) and Rodney et al. [27] (b).

Periodic boundary conditions are enforced along the Burgers vector direction and the dislocation line direction. The other direction (perpendicular to the slip plane) is either a free surface (zero stress) or a fixed layer (rigid block of thickness of 3 atomic planes) that is used as a grip to apply shear.

The model used to apply a shear displacement on the edge dislocation is sketched in Figure 3.6, where the edge dislocation evolves in a $\langle 110 \rangle$ dislocation gliding direction and a $\{111\}$ dislocation habit plane. The line direction is $[\bar{1}12]$ and the slip plane is $(1\bar{1}1)$. The *A* region locates free atoms. The *D* region represents the upper and lower rigid blocks where atoms are not allowed to relax (grips). These rigid blocks are submitted to PBC (Periodic Boundary Conditions) in the *x-z* directions and are displaced in the *x* direction in an opposite direction. This method of displacement leads to generate a gliding of the dislocation from a shearing deformation of the simulation cell. The regions *P* and *S* are respectively the regions where PBC and a fixed surface are applied. The dislocation is subjected to a glide force with a rigid displacement of the block *D* in the *x* direction. The shearing is simulated and the stress is calculated from the internal force per unit area: $\sigma_{xy} = F_x / A_{xy}$. Where F_x is the external force applied by the rigid displacement in the *x* direction to the block *B*. A_{xz} is the area of the *x-z* cross-section of mobile atoms *A*.

The advantage of shear deformation is that it can be extended over a long period of time. The difference between static and dynamic is that in the first case, the conjugate gradient relaxation (CGR) [28] method is used to relax the *A* region whereas in the second case, the atoms are relaxed in *NVE* ensemble. But in both static and dynamics conditions, the shear deformation leads to an elastic deformation of the simulated cell until local Yield Stress (YS) is reached. Once this stress level is reached, the dislocation starts to move according to the shear deformation direction. Thanks to PBC, the motion of the dislocation can be infinite.

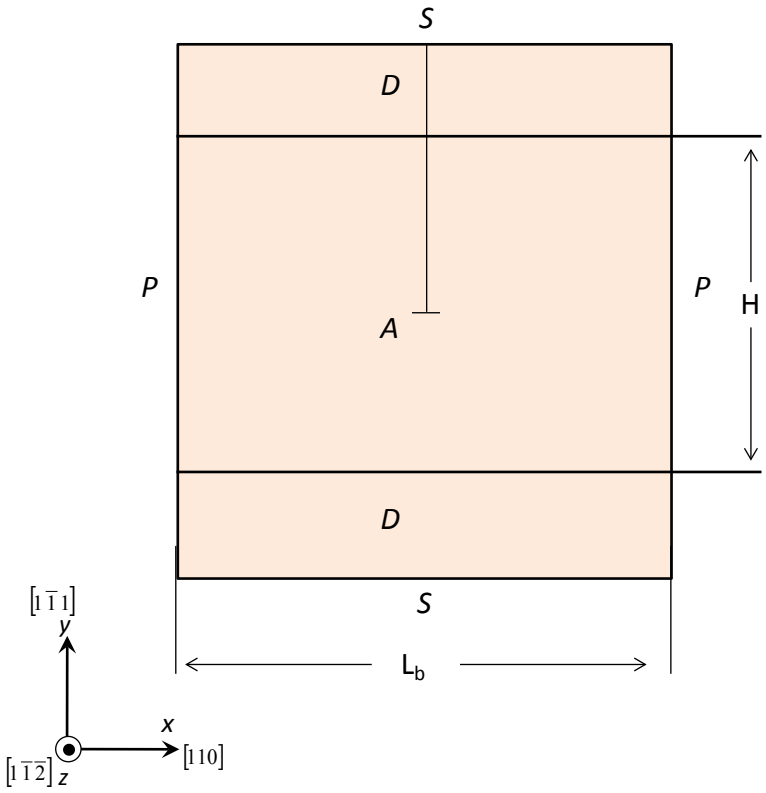

Figure 3.6: Representation of the simulated cells. *A*: mobiles atoms, *P*: PBC applied, *S*: Fixed Surface applied, *D*: rigid block for shearing.

3.3.2. Visualization method

Two geometrical methods are used to visualize the dislocation core. The first one is based on the visualization method developed by Rodney [29]. The local environment of each atom in the cell is compared to a perfect FCC environment by counting the number of first neighbors that are less than 0.25 nm. Thus, only the atoms, which have not twelve perfect FCC first neighbors are displayed. Based on these conditions, atoms which have 11 or 10 FCC perfect first neighbors are associated to the partial dislocation core whereas the atoms in the stacking fault area are associated with 9 FCC perfect first neighbor atoms. So the dislocation core is revealed as a double layer belonging to the upper and lower half-crystals.

The second method consists in creating pairs of neighbor atoms in symmetrically opposite position with respect to the central atoms for centrosymmetric lattice sites, hence the $i + N_p$ notation in formula (3.6) [30]. The centrosymmetric parameter P is close to zero for perfect lattice sites and becomes non-zero for defect atoms.

$$P = \sum_{i=1}^{N_p} \left| \vec{r}_i + \vec{r}_{i+N_p} \right|^2 \tag{3.6}$$

There are $N \times (N-1)/2$ possible neighbor pairs that can contribute to this formula. The quantity in the sum is computed for each, and the N/2 smallest are used, where $\vec{r}_i$ and $\vec{r}_{i+N_p}$ are the position of the pair of perfect atoms around the investigated atom. Generally, the atoms with the Centro-Symmetry Deviation (CSD) parameter included between 0.01 nm^2 < *P* < 0.03 nm^2 correspond to the core of the partial dislocations whereas a CSD parameter *P* > 0.03 nm^2 is associated to the stacking fault area

between the two Shockley partials. The advantages of these visualization methods is that the noise induced by thermal displacements is well-dominate. Moreover, they do not depend on the interatomic potential functions, unlike the energy filtering method.

Energy filtering method is based on the potential energy of an atom to decide whether or not it forms a perfect lattice with its neighbors. As the energy of atoms in a defect position is higher than the perfect lattice, *i.e.* the ground state, defective atoms can be detected using a threshold energy. However, this method presents several shortcomings. The atomic energy levels of perfect and metastable defects atoms can be easily overlapped due to thermal energy. Moreover, the energy is evaluated from the potential energy which is specific to the interaction model and interatomic potential. This is why the structural analysis method is preferred to the energy filtering method.

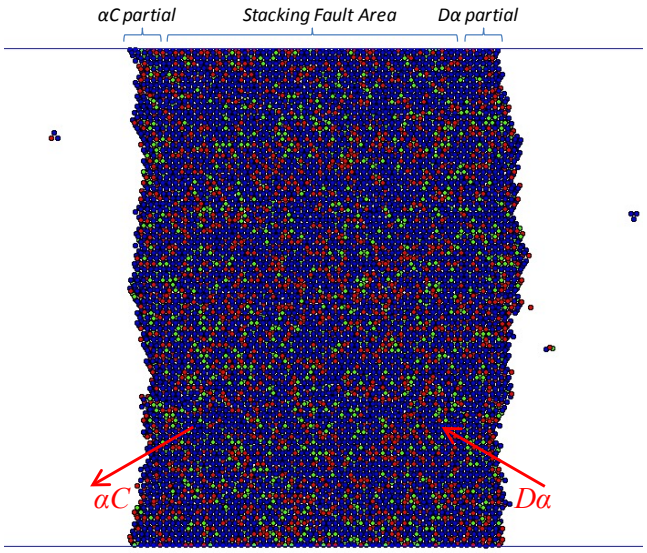

Figure 3.7: Straight edge dislocation dissociated into two partial dislocations with Burgers vectors *αC* and *Dα* bounding by an area of stacking fault revealed with the CSD analysis. Only the atoms in the defect zone are represented. The atoms in the "bulk" are omitted.

3.3.3. Energy model

The interatomic potential reproduces the interactions between particles based on the "hard sphere" model. Interaction energy between atoms has to go infinite when atoms are close to each other, *i.e.* lower than the diameter and zero when the separation distance between particles is infinite. Whereas in a semiconductor or dielectric, electrons are localized, in metals, they are shared with atoms in an electron cloud.

In this PhD, the EAM interaction potential of Bonny *et al.* [9] has been used to describe our Fe-Ni-Cr system. It includes a pair interaction function, *V*, and an embedding energy *F* function dependent on the local electron density, *ρ*. The interatomic potential form is:

$$E = \frac{1}{2}\sum_{\substack{i,\ j=1 \\ j\neq i}}^{N} V_{t_i t_j}\left(r_{ij}\right) + \sum_{i=1}^{N} F_{t_i}\left(\rho_i\right) \tag{3.7}$$

where *N* represents the total number of atoms in the system, r_{ij} is the distance between atoms *i* and *j* and t_i indicates the chemical species (Fe, Ni or Cr). The local electron density around atom *i* is given as:

$$\rho_i = \sum_{\substack{j=1 \\ j \neq i}}^{N} \phi_{t_j}\left(r_{ij}\right) \tag{3.8}$$

where ϕ_{t_j} denotes the electron density function of the element. Thus, in the case of the ternary system, twelve functions need to be defined through the potential as: ϕ_{Fe}, ϕ_{Ni}, ϕ_{Cr}, F_{Fe}, F_{Ni}, F_{Cr}, V_{FeFe}, V_{NiNi}, V_{CrCr}, V_{FeNi},V_{FeCr} and V_{NiCr}.

3.4. Simulation results: bulk properties

3.4.1. Plotting the FeNiCr potential functions

A visualization of the potential functions used to simulate the ternary composition Fe-10Ni-20Cr developed by Bonny *et al.* [9] is represented in Figure 3.8. These figures indicate that the pair-potential, embedded and density functions are smooth and no significant oscillations occur.

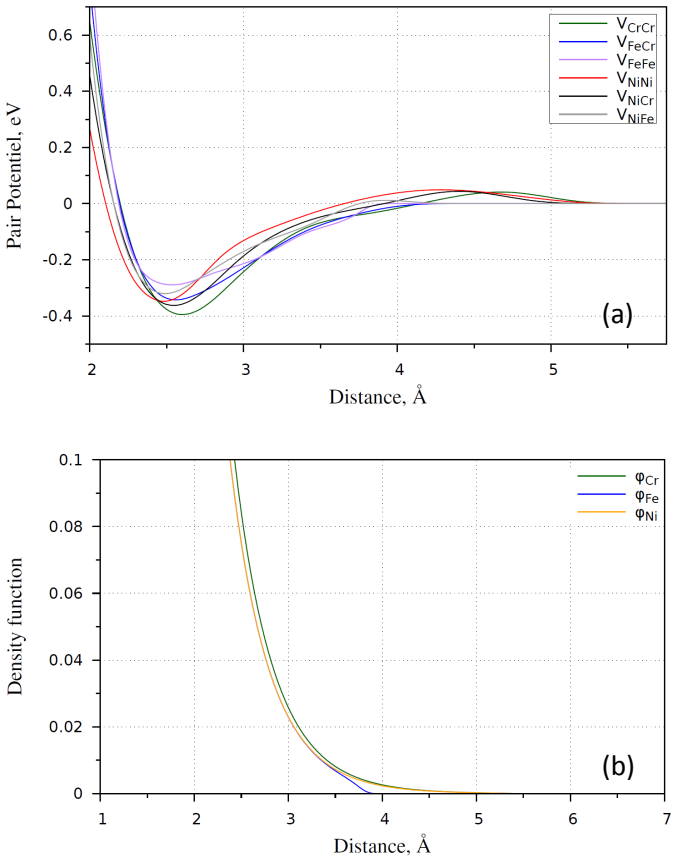

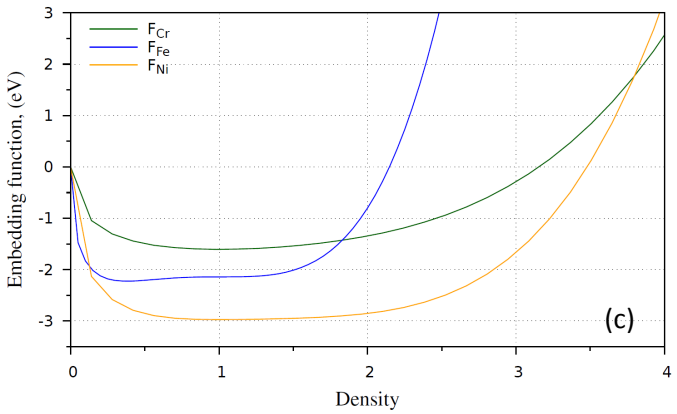

Figure 3.8: Plotting the potential functions: pair potentials (a), density functions (b) and embedding functions (c).

For Ni, the basic properties such as lattice parameter *a* and cohesive energy E_{coh} come from experimental results [31] and Density Functional Theory (DFT) simulations [32]. For Fe and Cr element, the target values come from DFT calculations respectively [33, 34 and 35] and [36]. The materials properties investigated here are the lattice parameter and stable SFE with the influence of the composition and the temperature.

As detailed in Bonny *et al.* [9], the potentials for the pure elements were first fitted considering the stability of different crystallographic structures, their cohesive energy and equilibrium lattice parameter, the elastic constants for the equilibrium lattice and some defect, formation and migration energies, (self-interstitial, dumbbells). Then, for the alloy, the potential functions were fitted to get correct SFE as a function of composition and elastic constants for the Fe-10Ni-20Cr target composition.

3.4.2. Composition and temperature effects on the lattice parameter

The knowledge of the lattice parameter is essential to carry out simulations without any internal stress. The lattice parameter is calculated in static and dynamic conditions on a box of 4000 atoms. PBC are applied in all directions to avoid free surface. The crystal is oriented along $\langle 100 \rangle$, $\langle 010 \rangle$ and $\langle 001 \rangle$ directions. The evolution of the hydrostatic stress with the lattice parameter will give the equilibrium lattice constant in static and/or dynamic conditions: the equilibrium lattice parameter is the one for which hydrostatic stress cancels out.

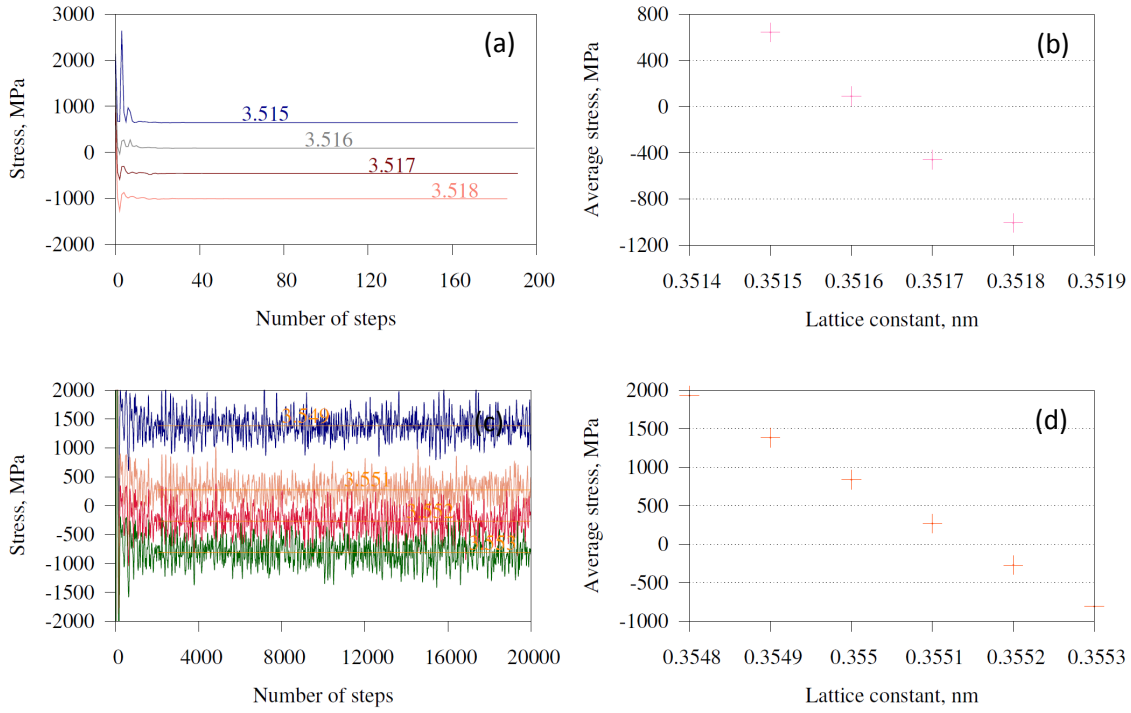

Figure 3.9: Evolution of the average stress in static ((a) and (b)) and in dynamic conditions (600 K) ((c) and (d)) versus numbers of static (conjugate gradient) and dynamic steps. The evolution of the average stress versus lattice parameter is represented in static (b) and in dynamic (d) conditions. The equilibrium lattice parameter is the one for which hydrostatic stress cancels out.

In dynamic conditions, simulations are carried out under NVT ensemble during 2,000 time steps and then under NVE ensemble during the next 18,000 time steps. Stress is then averaged over the whole NVE timespan. It can be seen in Figure 3.9 that the lattice parameter varies almost linearly with temperature in static as well as in dynamic conditions.

In their original contribution, Bonny *et al.* [9] presented the EAM interatomic potential and checked that it did reproduce a lattice constant at 0 K for pure Ni, Cr and Fe. However, in the framework of the present thesis, it is important to check if those potentials correctly reproduce the effect of both temperature and composition on the lattice parameter.

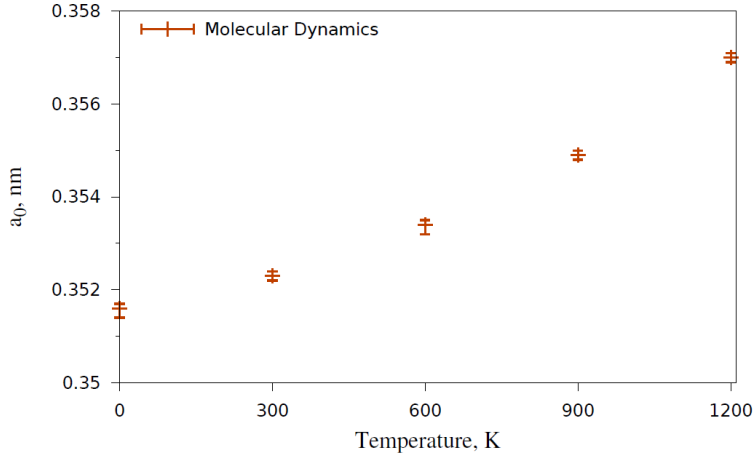

Figure 3.10: Evolution of the equilibrium lattice parameter with the temperature for Target composition: Fe-Ni_{10}-Cr_{20}.

The equilibrium lattice parameter has been calculated as a function of temperature between 0 and 1200 K for an alloy of target composition Fe-Ni_{10}-Cr_{20} for 10 randomly distributed alloying elements (called seed numbers). It is represented in Figure 3.10. The difference between Minima and Maxima are the values obtained for different seed numbers. The dilatation coefficient obtained in the 300-600 K domain is 10.4×10^{-6}/K, which compares well with the experimental one ($\sim20\times10^{-6}$/K [37]), although the calculated value is a bit smaller.

Alloying composition in this study has been chosen to reproduce a ternary composition of Fe-Ni_x-Cr_y alloy, where X=5, 10 or 20% and Y=10, 20 and 40%, which raises 9 compositions to investigate including a target composition close to 304L and 316L austenitic stainless steel. The evolution of the equilibrium lattice parameter versus Ni and Cr concentration in static conditions is represented in Figure 3.11 (a). Ni tends to decrease the lattice parameter whereas Cr tends to increase it. Note that these trends are in contradiction with the atomic masses. Based on alloying composition, Ni and Cr stress effects are well reproduced by the ternary interatomic potential. The linear evolution of the lattice parameter matches with the experimental results obtained by Baeva *et al.* [38] and Beskrovni *et al.* [39], shown in Figure 3.11 (b). However, the influence of Cr on a_0 is 2.10^{-3} nm/at% from experimental measurements and 1.10^{-3}nm/at% from our simulations.

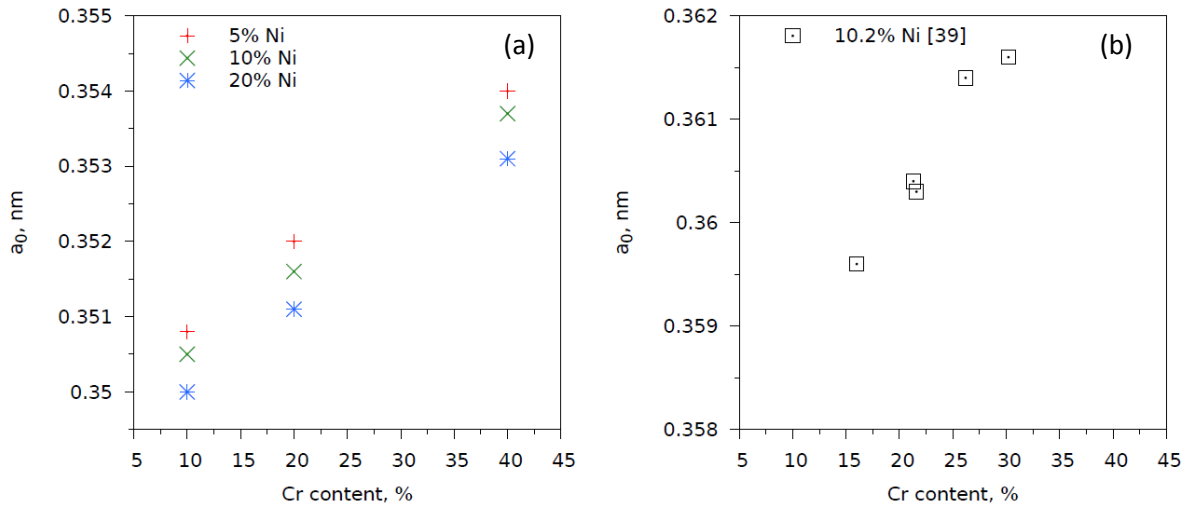

Figure 3.11: Evolution of the equilibrium lattice parameter versus percentage of Ni and Cr in static conditions (a) and in experimental conditions at room temperature (b).

To complete the FeNiCr potential checking, SFE calculation is also a good index to check the reliability of that potential and its possibilities to study the motion of dissociated dislocation.

3.4.3. Stacking Fault Energy evaluation

It is well known that the value of SFE, γ_{SFE}, for FCC material is a crucial factor to determine its physical and mechanical properties. In addition to solute concentrations, temperature is also an important parameter that can have some impact on γ_{SFE}. Experimentally, the node technique, using the theories of Brown and Thölen [10] (see section 3.1.), is applied whereas in MD, there are actually no specific techniques to evaluate it. In this part, we report a solute concentration investigation conducted in static conditions and a temperature influence on γ_{SFE} in dynamic conditions.

The simulation box contains 12000 atoms. Its dimensions are L_x=2.5 nm, L_y=12 nm and L_z=4.3 nm where L_x, L_y and L_z are respectively associated to the $[110]$, $[1\,\bar{1}\,1]$ and $[\bar{1}12]$ directions. The faulted

crystal is separated in two halves in the $[1\,\bar{1}\,1]$ direction to move the upper halve of b_p in the $[\bar{1}\,12]$ direction. The technique used to calculate the Generalized Stacking Fault (GSF) consists in displacing the upper half-crystal in the desired direction. Once the atoms are displaced, they are free to relax only along the $[1\,\bar{1}\,1]$ direction, preventing thus the upper block from returning to its initial equilibrium position or SFE position. The method to evaluate SFE in static and in dynamic conditions is quite similar. In both cases, a perfect and a faulted crystal are generated. As the stacking fault corresponds to a metastable position, all atoms are allowed to relax fully.

The local energy maximum level (saddle point), indicated as γ_{USF}, has to be evaluated as it corresponds to the energy barrier that Shockley partials should overcome to reach the metastable state associated to SFE level. In Figure 3.12 (a), one can see that the energetic path associated to $\langle 110 \rangle$ direction is higher than $\langle 112 \rangle$ direction. Thus, Shockley partial follows the energetic path represented in Figure 3.12 (b) during the motion in the $\langle 110 \rangle \{111\}$ gliding system. The saddle point corresponding to γ_{USF} has been evaluated to 330 mJ/m^2 whereas the local minimum corresponding to γ_{SFE} is around 20 mJ/m^2 for the target composition Fe-Ni_{10}-Cr_{20}.

Figure 3.12 (a) represents a GSF curve for a displacement of the upper block in two $\langle 112 \rangle$ directions. Once the γ_{USF} barrier is crossed, an equilibrium lattice spacing that does not correspond to the bulk equilibrium structure can be found, which is associated to the intrinsic stacking fault. The excess energy associated to this configuration is the SFE. The displacement along the GSF curve in the $\langle 112 \rangle$ directions is the slip direction for partial dislocations in an FCC crystal. The top inset of Figure 3.12 illustrates the evolution of the atomic configuration at the shearing interface during the displacement of the upper half-crystal related to the lower one. An intrinsic stacking fault occurs for a displacement of the upper crystal of $\vec{b}_p$ with $b_p = a/\sqrt{6}$ while the saddle point is reached for a displacement of $\vec{b}_p/2$.

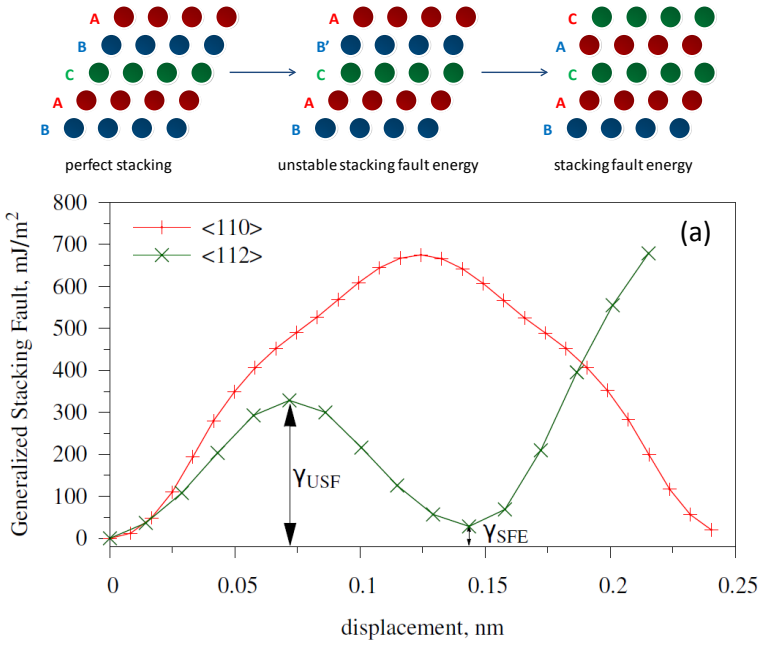

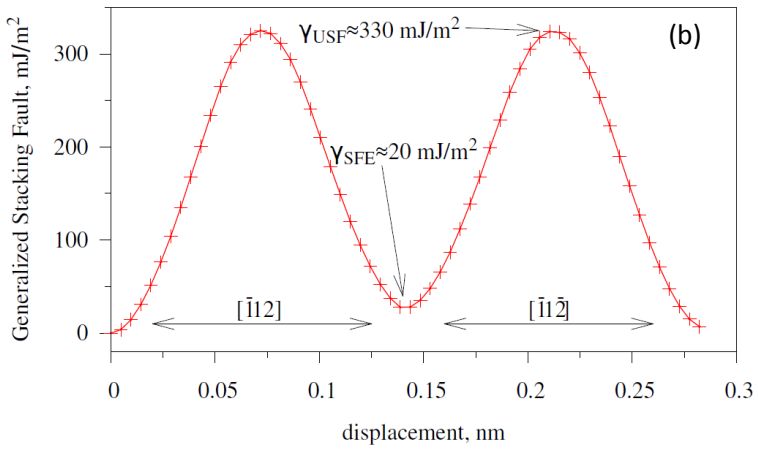

Figure 3.12: (a) Generalized Stacking Fault in the case of target composition for $\langle 110 \rangle$ and $\langle 112 \rangle$ direction (b) energetic path of the dissociated dislocation in the $\{111\}$ plan for alloying content 10% Ni and 20% Cr. The three extreme points are, according to the three corresponding configurations, shown in the top inset. The unstable stacking fault energy (γ_{USF}) and the SFE (γ_{SFE}) are displayed.

The results obtained for this potential are for an alloying content Fe-Ni_X-Cr_Y where X can take 5, 10 or 20% and Y 10, 20 and 40%. Those results are evaluated in static conditions. The calculation of the SFE is based on the potential energy difference between the faulted and perfect crystal (see Figure 3.13).

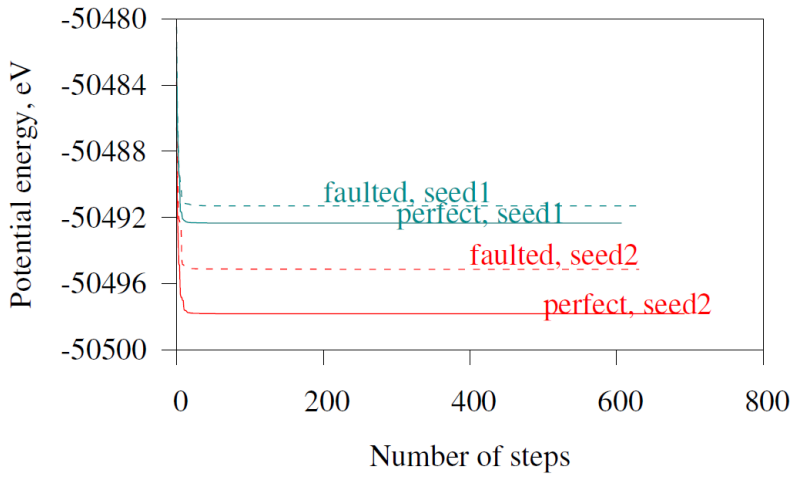

Figure 3.13: Evolution of the potential energy in static during relaxation steps. The energy difference between the faulted and the perfect crystal is represented for two different seeds (Fe-Ni_{20}-Cr_{20}).

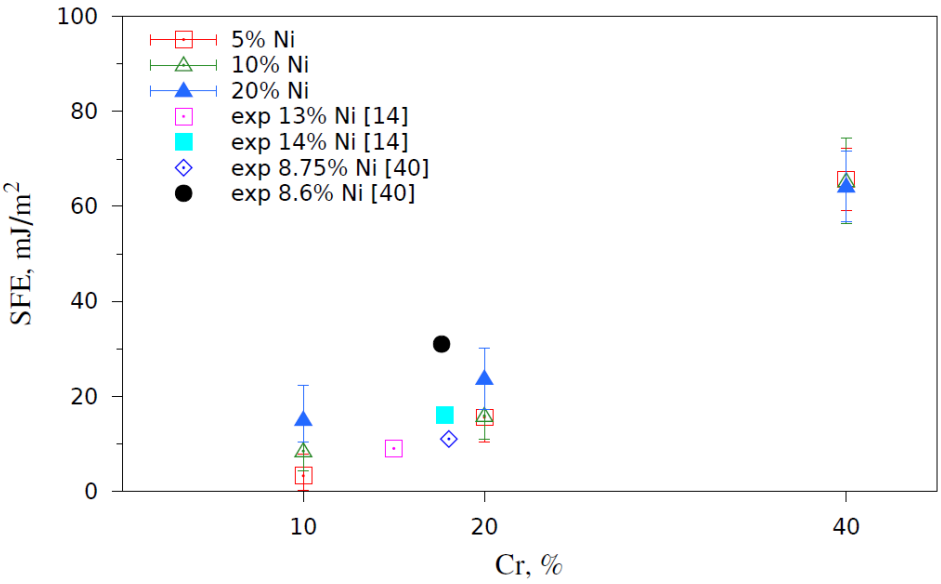

Figure 3.14: Corresponding SFE for alloying content Fe-Ni_X-Cr_Y where X can take 5, 10 or 20 % and Y 10, 20 or 40 % at 0K and comparison with experimental values [14, 40].

From Figure 3.14, we can see that Cr tends to increase SFE whereas Ni has a limited effect: for low Cr content, Ni seems to slightly increase SFE, whereas it has no effect for higher Cr content. In the case of target composition Fe-Ni_{10}-Cr_{20}, the potential gives a SFE value of 18 mJ/m^2. This value falls in the range determined by Li *et al.* [40] where a SFE value of 31 mJ/m^2 is associated to austenitic alloys Fe-$Ni_{8.6}$-$Cr_{17.64}$ and 11 mJ/m^2 for a ternary alloy Fe-$Ni_{8.75}$-$Cr_{18.04}$. Thus, this potential well reproduces low SFE value for a ternary alloy.

The uncertainty seems to be equivalent for all compositions and is only affected by the randomly distributed alloying elements. Negative values of SFE correspond to alloys for which FCC phase is no more ground state, at least locally. In such a case, regarding the local atomic environment, the four HCP platelets are more stable than the FCC structure.

As literature indicates an increase of SFE with the temperature, it is important to evaluate the effect of temperature on SFE for our potential. The simulations were conducted in the NVE canonical ensemble by introducing at the beginning of the simulation a temperature, which is approximately twice as much as the targeted temperature, in order to satisfy the equipartition theorem. Similarly to static conditions, the potential energy is measured and averaged over 9000 time steps. An example of the potential energy variation is represented in Figure 3.15 for a perfect and a faulted crystal. Then, the energy difference between the faulted and the perfect crystal is divided by the surface of the faulted plane.

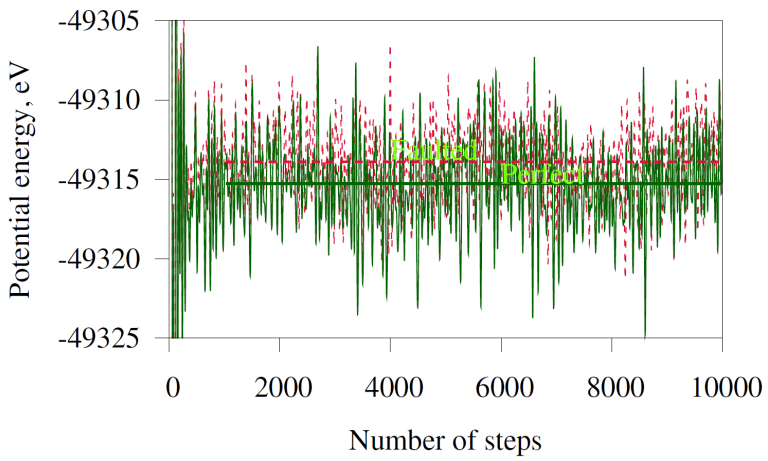

Figure 3.15: Evolution of the potential energy in dynamic conditions during relaxation steps for a perfect and faulted crystal.

The results obtained for target temperatures ranging between 0 and 900 K are represented in Figure 3.16. The SFE seems not to be affected by temperature. This is not in accordance with literature where SFE increases almost linearly until 600 K [12]. Nevertheless, this phenomenon cannot be reproduced with this potential as it is assumed that the increase in temperature of SFE is connected to the relative stability of HCP platelets within the FCC phase at various temperatures. The present potential has indeed never been optimized to reproduce the effect of temperature on the relative stability of HCP and FCC phases.

Moreover, note that the experimental values of SFE are measured with an indirect technique accounting for both SFE, friction (see section 3.1.) and isotropic material.

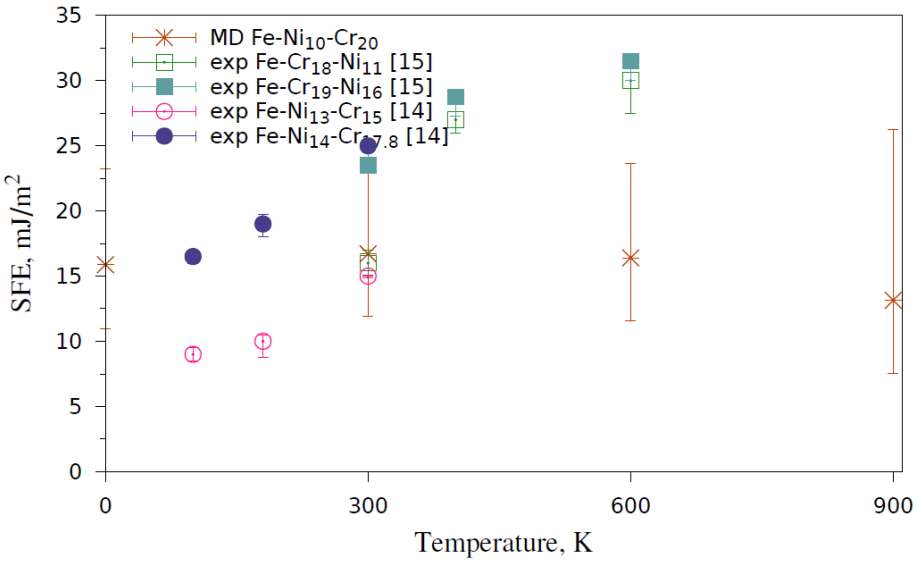

Figure 3.16: Temperature dependence of SFE in the case of target composition Fe-Ni_{10}-Cr_{20} and comparison with some experimental data [14, 15].

Another method that we can consider in determining SFE is based on the measurement of the dissociation distance d_0. These results are reported and detailed in section 3.5.3.. This method, used experimentally, consists in evaluating the ribbon width of a moving dissociated dislocation, *i.e.* when

a stress is applied. Thus, based on the analytical study developed in Chapter II, the SFE for a straight edge dislocation can be expressed as follows (see eq. 2.19 in chapter II):

$$\gamma_{SFE} = \frac{2+\nu}{24\pi(1-\nu)}\frac{\mu b^2}{d_0} \tag{3.9}$$

where ν is the Poisson's ratio and μ the shear modulus (given by Voigt or Reuss averaging elastic constant of the EAM FeNiCr potential [9]). b is the burgers vector and d_0 is the dissociation distance. The edge dislocation moves through the solute solution, both partials are submitted to the same friction stress that cancels out when the dissociation distance is estimated (see section 2.2.). The results are gathered in Figure 3.17.

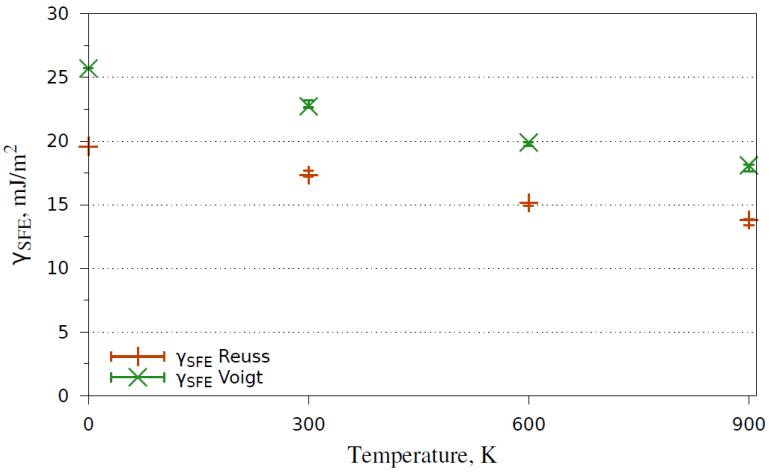

Figure 3.17: γ_{SFE} determined for the two sets of isotropic elastic constants (Reuss and Voigt average) depending on temperature from the dissociation distance measures of section 3.5.3..

The SFE decreases quasi linearly with temperature. The associated SFE to the target composition is included between the Reuss and the Voigt γ_{SFE} values. These results are supposed to be more accurate than those presented in Figure 3.16 where the SFE calculation is local and depends strongly on the alloying content. On the contrary, SFE evaluated in Figure 3.17, based on the d_0 results, is established after the dislocation moves through the entire glide plane, which has been proven to contain strictly 30% of adding elements. Finally, SFE may also have an entropic contribution that would require thermodynamics integration. This analysis would however go far beyond the scope of this thesis.

The potential properties have been investigated through the lattice parameter and SFE. The lattice parameter, a_0, and the SFE are calculated for different compositions and temperatures. In the case of the target composition (Fe-Ni_{10}-Cr_{20}), the influence of temperature on a_0 matches well with the experimental results [37]. The influence of composition on a_0 points out a quasi-linear dependence, which compares well with the experimental data [38, 39].

In static conditions, the SFE calculated for the Fe-Ni_{10}-Cr_{20} composition, is included in the range established by Li and Almazouzi [40] for austenitic stainless steels. The influence of composition reveals an increase of SFE with both Ni and Cr. This last observation is in contradiction with the experimental data gathered by Vitos *et al*. [41] concerning the Cr effect, where the SFE is shown to decrease when Cr content increases. However, Ni effect is correctly reproduced. Thus, Cr stabilizes

the HCP phase whereas Ni destabilizes it relative to the FCC phase. However, in this PhD thesis, all the calculations are conducted on the Fe-Ni_{10}-Cr_{20} material, which well reproduces the experimental SFE of austenitic stainless steel. Thus, the effect of Ni and Cr on SFE should be negligible in our simulations.

The effect of temperature on SFE is calculated with two different methods. The First method is based on the potential energy difference between the faulted and the perfect crystal. The second method is based on the experimental method which consists in evaluating the dissociation distance d_0.These two methods indicate a decrease of SFE with temperature which is not in accordance with the experimental studies [14, 15]. However, some thermodynamic phenomena are not taken into account such as the segregation of alloying elements around the partials, which is supposed to influence the stability of the HCP phase, and on the other hand, a decrease of SFE has been already observed in pure Al [13], but the reasons to explain it have not been clarified yet. Moreover the relative stability of FCC and HCP phase is not considered here.

3.5. Effect of initial conditions, temperature and stress on the dissociation distance

The dissociation distance is one of the possibilities used experimentally to determine the SFE and is representative of the deformation mode, *i.e.* dislocation pileup or twinning. Moreover, it is also a key factor in determining the friction stress of the material (see Chapter II). The dissociation distance depends strongly on SFE. Usually, austenitic stainless steel has a low SFE compared to other materials like aluminum where the SFE is situated between 108 mJ/m^2 [42] and 260 mJ/m^2 [43] that corresponds to a dissociation distance of around 1-3 nm. The SFE in austenitic stainless steel is included between 10-40 mJ/m^2 [40] with a separation distance of 10-15 nm.

3.5.1. Dissociation distance measurements

The dissociation distance of an edge dislocation is measured in a metastable position, in the case of d_- and d_+, and in a stationary motion in the case of d_0 (sees section 3.5.3.). d_- and d_+ are generated respectively with the Rodney's method [27] and the Osetsky's method [26]. d_0 is associated to the dissociation distance at equilibrium (see chapter II), that means the Shockley partials are not in a constrained equilibrium, like d_- and d_+, but in their stable positions associated to the energy minimum *E(d)* of the dislocation core.

The simulation cell is sketched in Figure 3.18 with the associated Thompson tetrahedron. The habit plane of the simulated edge dislocation in this study is the BDC or α plane. The crystallographic orientations were chosen such that a straight edge $a/2\left[\bar{1}\,\bar{1}\,0\right]\left(1\,\bar{1}\,1\right)$ dislocation is introduced in the two central $\left(1\,\bar{1}\,1\right)$ planes of the simulated cell with a line along the $Z=\left[\bar{1}\,1\,2\right]$ axis and perpendicular to the $X=\left[\bar{1}\,\bar{1}\,0\right]$ axis, assimilated to the *CD* Burgers vector direction in the Thompson notation. The *X*, *Y* and *Z* directions have respectively the following dimensions (45x30x20 nm^3). The cell contains 2.59 million of atoms. The use of PBC allows constructing an infinite periodic gliding for the edge dislocation.

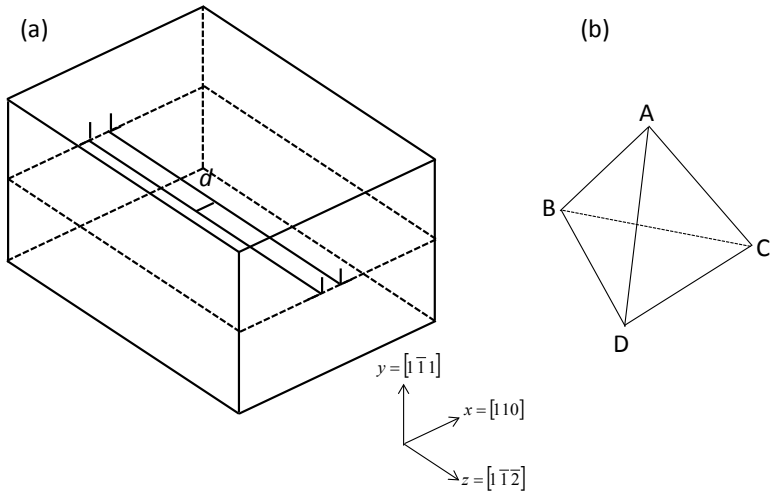

Figure 3.18: (a) Sketch of the simulation cell and (b) the associated Thompson tetrahedron.

The simulation is first conducted without applying any loading on the cell in order to get d_- and d_+ and then by applying shearing on the box to get d_0 with the method described in section 3.3.1.

3.5.2. Dissociation distance measurements at equilibrium

To complete the measurement of d, the coordinates of atoms that constitute the core of the trailing and leading Shockley partial are extracted. The targeted atoms are selected from their CSD number (see section 3.3.2.), *i.e.* atoms which have 10 and 11 perfect FCC first neighbors. Then, the x position of each Shockley is averaged from the x coordinates of their particles. The ribbon width comes from the difference between these two x coordinates.

Dissociation distances measured at various temperatures are gathered in Figure 3.19. It shows that d_+ does not depend on temperature but increases with L_x. Conversely, d_- constitutes a relevant variation of the friction stress with thermal vibration and at first glance, it increases rapidly with temperature. This can indicate that friction stress is rapidly overcome by thermal vibration.

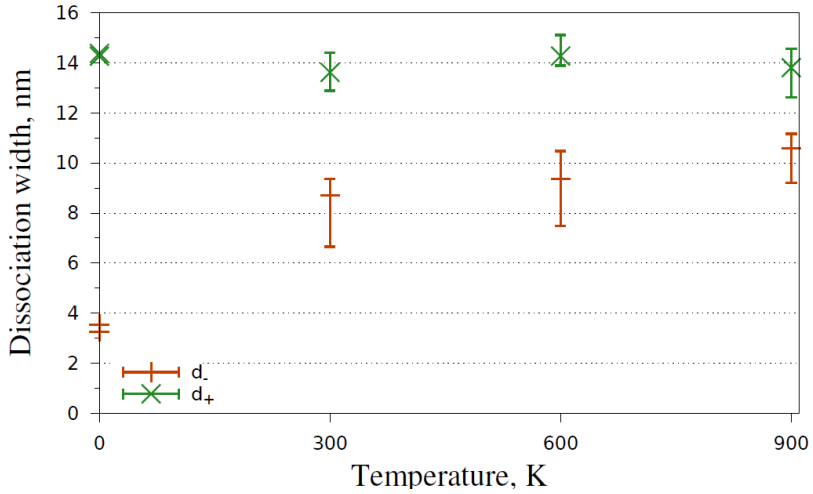

Figure 3.19: Dissociation distance d_- and d_+ versus temperature.

3.5.3. Dissociation distance under stress

As it has been demonstrated by Byun *et al.* [44], there is a huge SFE dependence of the dissociation distance between the two Shockley partials. Thus, the dissociation distance can be used as a

parameter to determine the SFE value in the material. The measurement of the dissociation distance has been conducted at 0 K for the three compositions Fe-Ni_5-Cr_{10}, Fe-Ni_{10}-Cr_{20} and Fe-Ni_{20}-Cr_{40}. For pure FCC Fe, as SFE has been calculated to be negative, the infinite dissociation distance directly leads to a twinning in the material, which implied an infinite distance between the two Shockley partials. The MD results are presented in Figure 3.20. Those results reveal a good correlation with the restoring force and dissociation distance. After a certain rate of deformation, when the dislocation starts to glide, it is observed that dissociation distance oscillated around an equilibrium value.

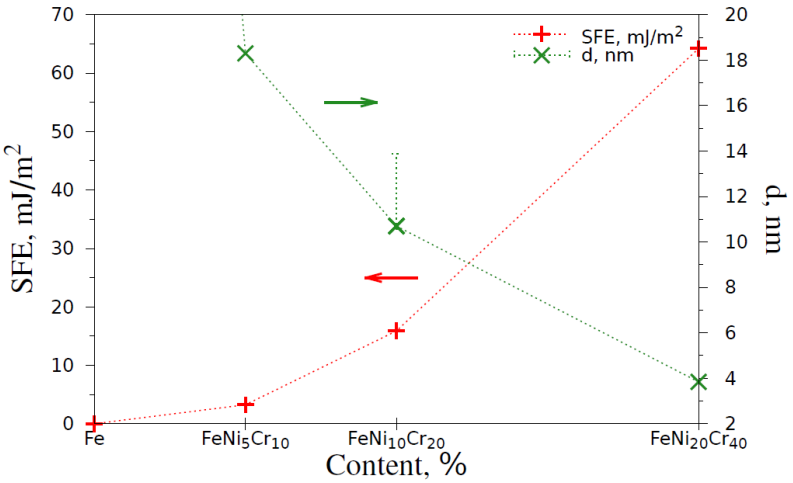

Figure 3.20: Content dependence of SFE and dissociation distance in static conditions. The error bars represent for the Target composition the dissociation distance obtained from the Reuss and Voigt average.

Analytical results established in chapter II show that the stress component τ_{zx} tends to move the dissociation distance into the stable equilibrium position d_0 [45]. This can be achievable with MD by applying a constant strain deformation on the simulation box from a d_+ position. The results are shown in Figure 3.21. The deformation is conducted with 3 different deformation strain-rates to check if there is any effect of dislocation velocity on the dissociation distance, in a case of a Fe-Ni_{10}-Cr_{20} composition. It reveals that the shear rate has no influence on the dissociation distance, which suggests that the stress amount to move the two partials into their stable position can be reached very fast, even if a high strain rate is applied.

Another point to consider is the variation of the dissociation distance regarding the increasing with temperature (see Figure 3.21). One surprising observation is that the dissociation width still continues to evolve at 900 K with, apparently, a linear dependency. Unfortunately, as the potential is not reliable above 900 K and the stability of the FCC phase is not certified, the investigation of the dissociation width cannot be pursued above.

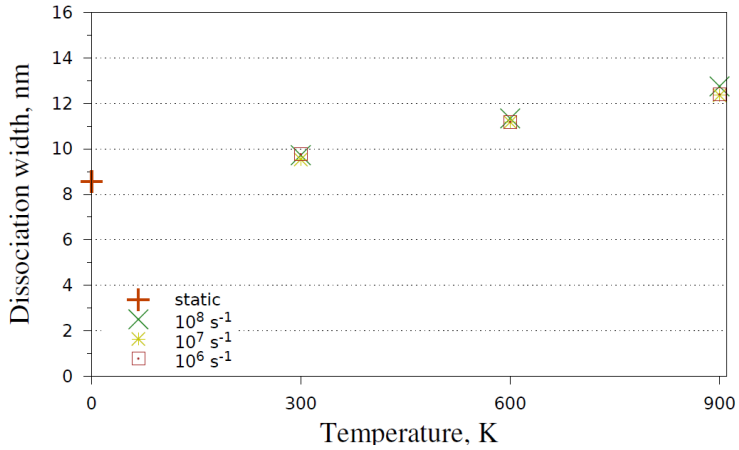

Figure 3.21: Dissociation distance evaluated at equilibrium for three deformation rates depending on temperature.

Figure 3.22 displays snapshots of straight edge dislocations corresponding to the different methods used to insert edge dislocations in the simulated cell. In our simulated alloys, maybe due to local atomic configurations, the shape of trailing and leading partials is wavy. This trend seems to be emphasized when the dissociation distance is lower than the equilibrium distance. Olmsted *et al.* also observed that phenomenon and pointed it out for an Al/Mg solute solution alloy [46]. The visualization of the atomic configuration in Figure 3.22 confirms the solid solution to be random at the scale of the dissociation ribbon. Although the presence of bending on the partial dislocations is high, the effects of dislocation curvature are not considered in our model [45].

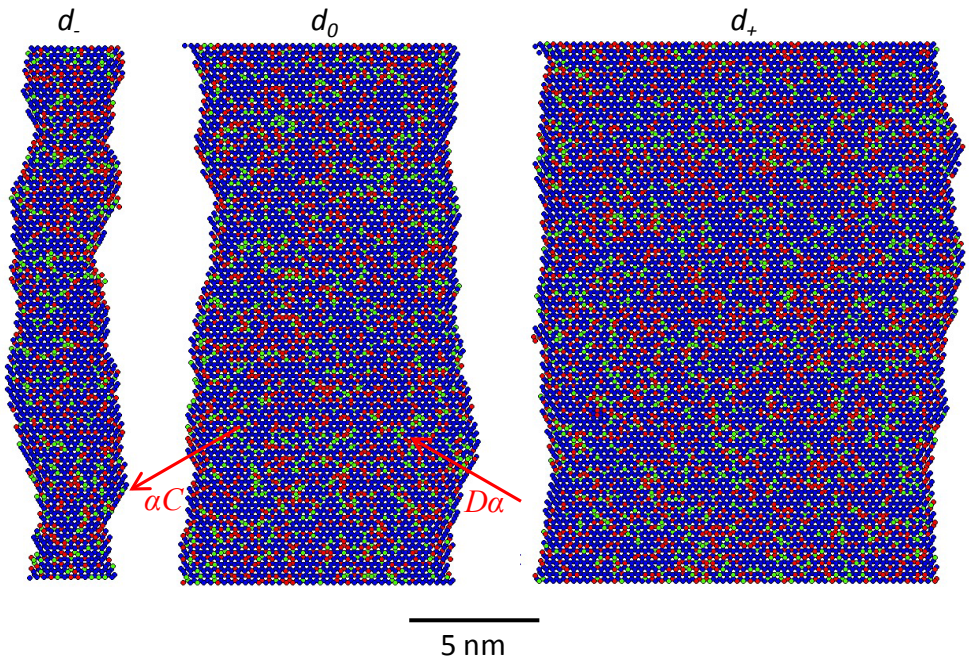

Figure 3.22: Dissociation distance d_-, d_+ and d_0 obtained at 0 K.

The dissociation distance has been investigated here in order to obtain the SFE of our material and the friction stress τ_f, when the dislocation has no velocity. To conduct this study, the edge dislocation is introduced in two different ways, *i.e.* by removing [27] or inserting two extra half-planes [26]. The first method generates a perfect dislocation, *i.e.* non-dissociated, whereas the other one spreads the dislocation core over the whole gliding plane. Thus, when the dissociation distance is lower or higher

than d_0, the equilibrium distance, the dissociation is called d_- or d_+, respectively. The static and dynamic simulations reveal strictly no evolution of d_+, with temperature. By contrast, d_- is highly affected by temperature and increases by a factor of three from 0 to 900 K. d_0 is found to not depend on the strain rate $\dot{\gamma}$, as the stress component applied here is equivalent to the stress component τ_{xz}, developed in Chapter II, which leads to the movement of the whole dislocation.

If the dimensions of the box in the direction of the Burgers vector increases, d_+ increases. These last two observations can highlight that the friction stress has a stronger influence than the image forces. The temperature dependence of d_0 leads to a slight increase which is perfectly enclosed between the corresponding results of d_- and d_+. This separation distance is in accordance with the experimental results which point out ~10 nm (see for example [44]).

3.5.4. Determination of the friction stress

The friction stress, resulting from the presence of alloying elements, induces an important strengthening in 316L stainless steel [47]. Referring to Chapter II, d_-, d_+ and d_0 is key parameters to get the friction stress. This last parameter can be deduced from the following system:

$$\tau_f = \frac{A}{2b}\left[\frac{1}{d_-} - \frac{1}{d_+}\right] \qquad (3.10)$$
$$with\ A = \frac{(2+\nu)}{(1-\nu)}\frac{\mu b^2}{24\pi}$$

by doing so, the calculation of SFE is unnecessary. The resolution of this system can be done from the measurements of dissociation width presented in sections 3.5.2. and 3.5.3. The effect of the average constant can also be highlighted by applying the Reuss Average, where μ=60 GPa and ν=0.32, or the Voigt Average, where μ=88 GPa and ν=0.26. The results are gathered in Figure 3.23. As soon as the system is thermalized, the friction stress decreases almost by factor 10 for the two sets of average constants. Thus, we can assume that τ_f can be neglected at least from 300 K.

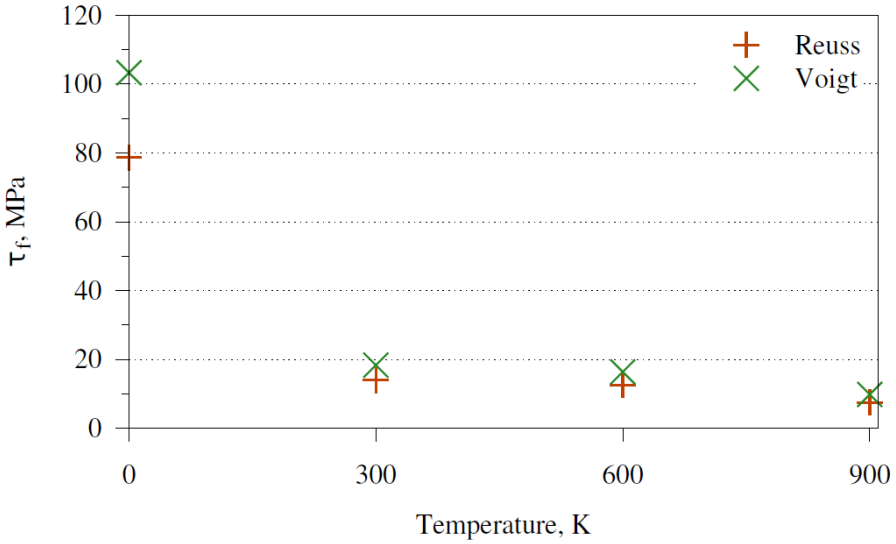

Figure 3.23: Friction stress resolution of τ_f from d_- measurements depending on temperature respectively for (a) Voigt (G=88 GPa, υ=0.26) and (b) Reuss (G=60 GPa, υ=0.32) average.

For this potential, the shear modulus has been determined between 51 and 52 GPa [9] for a temperature range of 0 – 900 K. With eq. (3.10), if the shear modulus is considered to not depend strongly upon temperature, the friction stress τ_f is supposed to decrease near the two curves defined in Figure 3.23 with the Reuss and the Voigt average. τ_f stress can be associated to the friction stress when no permanent deformation is applied, *i.e.* constitutes a limiting case for $\dot{\gamma} = 0$. Moreover, τ_f cannot be neglected even at 900 K, but is strongly influenced by temperature by decreasing by a factor of five from 0 K to 300 K.

The friction stress decreases rapidly with temperature and keeps decreasing above 600 K. The discrepancy obtained for the Reuss and the Voigt average is mainly marked in static conditions. Nevertheless, the friction stress τ_f, determined in static condition, is found to be close to the one experimentally measured by Monnet and Pouchon [48], where it has been evaluated at 95 MPa.

3.6. Mobility of an edge dislocation

The glide of an edge dislocation, in a random solid solution $FeNi_{10}Cr_{20}$ is simulated with MD. The ternary FeNiCr EAM potential is optimized to reproduce correctly the elastic properties C_{11}=214 GPa, C_{12}=136 GPa and C_{44}=129 GPa of 316L steels from experimental data [49]. In addition, the potential provides the stability of the FCC phase for a large deformation. Gliding is here studied at a fixed temperature and strain rate. The temperature range is between 300 – 900 K by applying a constant strain rate ranging between 10^6 and 2×10^8 s^{-1}.

This part is devoted to studying the dislocation glide in concentrated solid solutions of Ni and Cr through an Fe(NiCr) prototype without being disturbed by the thermal diffusion of Ni and Cr in the Fe host matrix, which does not occur in MD where every atom stays in their assigning initial positions. The equilibrium shape of the dislocation results from the interaction between the line tension of the dislocation and the strain field generated by the surrounding solute atoms. The glide of the edge dislocation follows a complex path, made of multiple pinning and unpinning events.

We studied the effect of dislocation velocity, temperature and solute solution contents on the dislocation glide, based on the dislocation position and the stress response resulting from a constant strain deformation. Firstly, some details of the MD technique are presented. Then, the influence of temperature, solute effects and strain rate are successively detailed. From this observation, a constitutive law will be extracted from the models already set and from a new one which is found to best describe the dislocation behavior during gliding.

3.6.1. Effect of temperature on the motion of an edge dislocation motion

The computational cell used here is depicted in Figure 3.24. The L_x, L_y and L_z directions are parallel to $[1\,1\,0]$, $[1\,\bar{1}\,1]$ and $[\bar{1}\,1\,2]$ directions respectively. The $(1\,\bar{1}\,1)$ glide plane is perpendicular to L_y direction. Applied PBC prevail in the *x* and *z* directions, while the movements of the atoms in the upper and lower surfaces are fixed and displaced towards ±*x* directions. All simulations proceed as follows: solute atoms are first distributed randomly, based on the input seed number, on the lattice with the appropriate concentration. The box dimensions are adjusted with an appropriate lattice parameter calculated for each temperature and solute solution to avoid internal stresses.

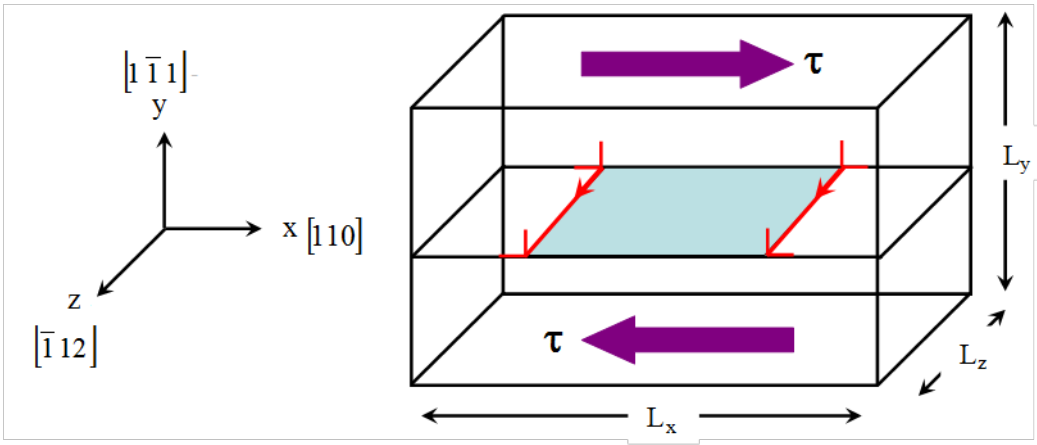

Figure 3.24: Computational cell: the dislocation is decomposed into two Shockley partials in its glide plane; the stacking fault area is represented here in blue between the two red partial dislocations. The shearing direction can be positive or negative depending on the convention.

The configuration obtained is then relaxed in a metastable state with a "quench" algorithm in static conditions and then in the *NVT*. This relaxation locates the dislocation dissociation in the metastable position d_+. The initial velocities are equidistributed on all the particles from a Maxwell distribution and thus a correlative displacement of atoms is forbidden. The time integration is carried out with a Verlet's algorithm at a time step of 1×10^{-15} s. This time step best discretizes the atomic thermal vibration around its position. It has been revealed that during the deformation, temperature increases by 1 or 2 K, which is of course negligible with the targeted temperature. This small variation of temperature allows keeping up the simulation in the *NVE* canonical ensemble. Once the dislocation is relaxed, the strain is applied at a constant strain-rate in the *NVE* canonical ensemble. The external strain is applied parallel to the glide plane on the upper and lower fixed layers.

In order to investigate the role of thermal activation on the gliding mechanism, MD simulations were carried out at least for 3 different strain-rates, in the temperature range of 0-900 K. Figure 3.25 shows an example of stress-strain curves for different temperatures. In all cases, the simulations start with an elastic regime, during which the dislocation is immobile within what can be assimilated to a Peierls valley [50] in the case of pure material. In such a position, the stress increases linearly with the strain at a rate $\dot{\tau}^{XY} = \mu\dot{\gamma}^{XY}_{elastic}$. The stress strain curve exhibits "local maxima", represented by squares in Figure 3.25, that indicate the instantaneous stress required to move the dislocation in its next position. The critical stress τ_c is then defined as the average of all instantaneous *maxima* (each maximum is itself defined by a stress drop of at least 10 MPa).

$$\tau_c = \langle \tau_{\max} \rangle \text{ and } \tau = \tau_{\max} \text{ if } \tau(\gamma + 0.01\%) - \tau(\gamma) > 10 \text{ MPa} \tag{3.11}$$

These successive stress drops observed in Figure 3.25 are associated to a displacement of the dislocation, which is supposed to depend on the Orowan's relation $\dot{\gamma}^{XY}_{plastic} = \rho_D b v_D$. The variation between the different maximum stresses comes from the local atomic configurations around the dislocation core. By combining the two previous relations, the total strain rate $\dot{\gamma}^{XY}$ is:

$$\dot{\gamma}^{XY} = \dot{\gamma}^{XY}_{elastic} + \dot{\gamma}^{XY}_{plastic} = \dot{\tau}^{XY} / \mu + \rho_D b v_D \tag{3.12}$$

The strain rate can be developed into an elastic term $\dot{\gamma}^{XY}_{elastic}$ that produces the stress and a plastic term $\dot{\gamma}^{XY}_{plastic}$ related to the dislocation motion. μ is the shear modulus, $\rho_D = 1/(L_X L_Y)$ the dislocation density, *b* the Burgers vector and v_D the instantaneous dislocation velocity. When the stress reaches a critical value, that can be associated to a local critical stress, the dislocation undergoes a first jump from its initial "solute valley" to a next one. This displacement produces a plastic strain given by the Orowan's relation $\Delta\gamma^{XY}_{plastic} = \rho_D b\bar{d}$, where $\bar{d}$ is the average distance crossed by one dislocation jump. Usually, in pure material, $\bar{d}$ is assimilated to Burgers vector *b*. This average distance $\bar{d}$ is calculated as the ratio between the total distance crossed by the dislocation, represented in Figure 3.26, and the number of jumps of the dislocation core after an unpinning period, *i.e.* when there is strictly no evolution of the dislocation core in time. Once the dislocation jumps, the elastic deformation is then converted into plastic deformation, *i.e.* $\dot{\gamma}^{XY} = 0$. In this way, the following relation can be assumed as:

$$\frac{\Delta\tau^{XY}}{\mu} = -\rho_D b\bar{d} \tag{3.13}$$

From the equation (3.13), we see that an instantaneous plastic strain increment leads to a stress drop of $\Delta\tau^{XY} = \mu\Delta\gamma^{XY}_{plastic}$. In our case ($\mu$=60 GPa or 88 GPa respectively for the Reuss and the Voigt average, *b*=0.2486 nm, $\bar{d}$=4.07 nm and ρ_D=1/(L_xL_y)=7.1×10^{14} m^{-2}), which gives a $\Delta\tau^{xy}$=43.3 MPa and 63.6 MPa (at *T*=300 K) depending on the shear modulus considered. The $\Delta\tau^{XY}$ obtained with the Reuss average (μ=60 MPa) is consistent with the serrations visible in Figure 3.25. The rest of the simulation is composed of elastic periods where the stress increases linearly, separated by plastic events marked by a stress drop when the dislocation changes its metastable position.

As it can be seen in Figure 3.26, the dislocation usually advances through multiple "solute valleys" at a time, but not just one valley as it can be encountered in pure material [50]. The dislocation may jumps over several valleys in one plastic deformation. We see from Figure 3.26 that the dislocation adopts an averaged velocity given from the Orowan's law: $\langle v_D \rangle = \dot{\gamma}^{XY}/\rho_D b$ which gives 5.67 $m.s^{-1}$ in our case. This equation is verified as the average elastic strain rate is zero and the average plastic strain rate is equal to the imposed strain rate, as it appears in Figure 3.26.

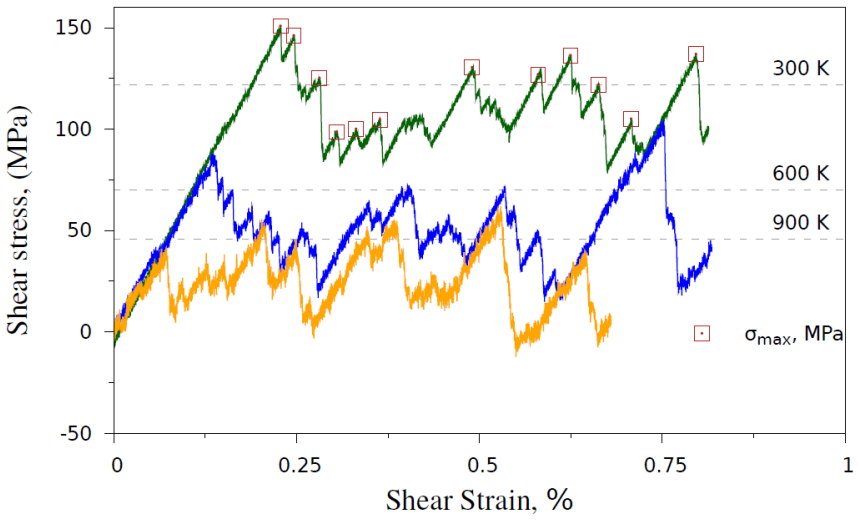

Figure 3.25: Stress-strain dependence obtained by a dynamic modeling of dislocation motion under applied strain for different temperatures at a 10^6 s^{-1} strain rate.

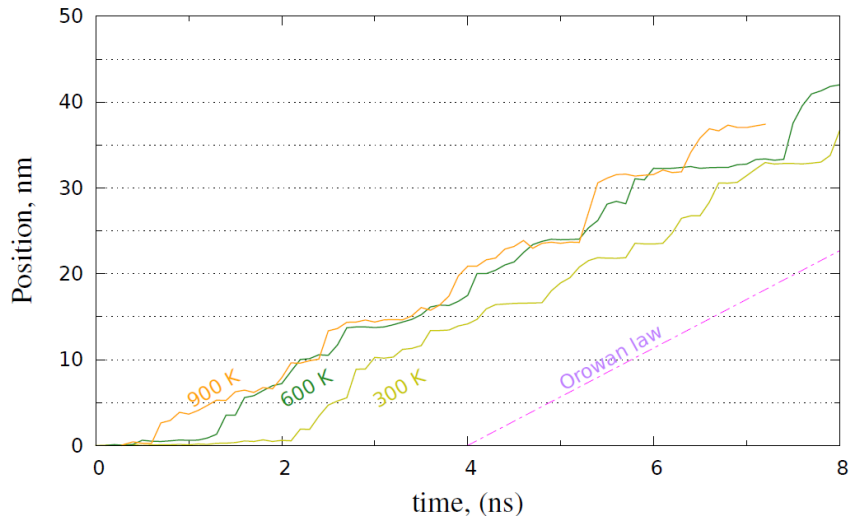

Figure 3.26: Position of the dislocation during constant strain-rate simulations (10^6 s^{-1}) at different temperatures.

The time dependence of the dislocation position reveals that the edge dislocation complied with the Orowan's relation for all temperatures. However, the first unpinning event occurs more rapidly over time at 900 K than at 300 K, which indicates a decrease of critical stress τ_c with temperature.

3.6.2. Effect of solute solution composition at 600 K

For low solute concentrations, the strongest configuration is when two solute atoms form a dimer above the dislocation glide plane [51]. The order of magnitude of pinning force associated to that dimer is more than twice as high as single solute atoms. The second order pinning effect is due to an equivalent dimer configuration in the slip plane of the dislocation. However, the Fe-Ni_{10}-Cr_{20} material is defined as a strong solid solution alloy and thus, can contain stronger configurations than simple dimers.

In this section, as we are in a highly concentrated alloy (30%), it is difficult to distinguish the pinning cluster from single solute elements. In fact the number of configurations present in the simulated cell is wide and the dislocation motion cannot be paced by a pseudo-period of Ni-Cr clusters. Anyway, a

comparison is realized of a stress-strain response for a strain-rate $\dot{\gamma}_0 = 10^6\ s^{-1}$ in a case of the target composition and for two other extreme contents Fe-Ni_5-Cr_{10} and Fe-Ni_{20}-Cr_{40}, respectively a lower and a higher content. The simulations are conducted at 600 K.

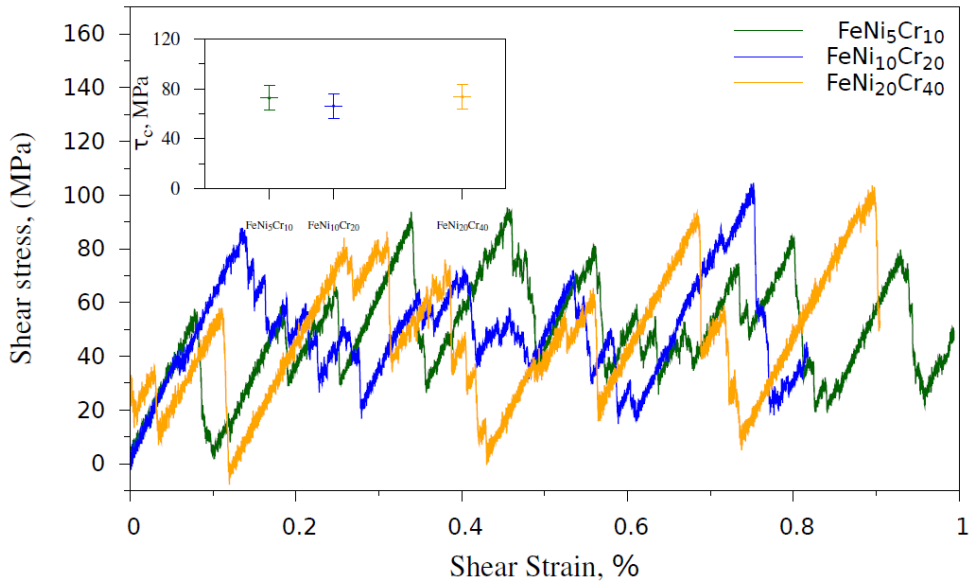

Figure 3.27: Stress-strain curves for three alloying contents under a strain rate of 10^6 s^{-1} at 600 K. The top inset indicates the evolution of the Critical stress with the alloying content.

Figure 3.27 reveals that the variation of alloying content in Ni and Cr does not have strong influences on the dislocation motion at 600 K. This observation is reinforced by the top inset of Figure 3.27 where the evolution of τ_c depending on the alloying content has strictly no influence. The decreasing or increasing alloying content does not increase or decrease the critical stress or the stress jumps $\Delta\tau$ of the dislocation from a "solute valley" to another. This observation is an insight that at a sufficiently high temperature, the variation of the solute concentration has no effect on the stress response.

The investigation of the solute solution effect has been conducted at 600 K, which is the averaged operating temperature of internals in RPVs, and shows no influence of alloying content on the stress response for three alloying compositions: $FeNi_5Cr_{10}$, $FeNi_{10}Cr_{20}$ and $FeNi_{20}Cr_{40}$ in a case of a dislocation velocity ~5.5 $m.s^{-1}$. The chosen compositions being extreme compositions, this can mean that at 600 K the critical stress is no longer influenced by the alloying content.

3.6.3. Effect of Strain-rate effect on dislocation mobility for $FeNi_{10}Cr_{20}$

In this part, we focused on the gliding behavior of an edge dislocation under different velocities for the target composition Fe-Ni_{10}-Cr_{20} at 300 K. Firstly, we investigate the distance traveled by the dislocation as a function of time. Secondly, the evolution of dissociation distance versus time is described. Finally, we end this part with a summary on the evolution of the critical stress depending on both temperature and strain-rate.

As the dislocation tries to get unpinned from its solute field, the remaining pinned segment experiences forces due to the curvature of the non-pinned segment, as it is shown in Figure 3.28 (a) in a case of a minima strain rate of 10^6 s^{-1}, whereas for a high strain rate (10^8 s^{-1}), the dislocation seems to move continuously, as it can be observed in Figure 3.28 (b). Classical analyses (see for example [52, 53 and 54]) have shown the strengthening induced by solute elements is a function of

the atomic solute concentration *c*, the spatial configurations of solutes, the spatial range of the solute-dislocations interaction and the dislocation line tension. In literature, two kinds of interactions are considered. The first one considers solute atoms as obstacles with an associated strength to overcome to be able to release the dislocation from its pinning points. This force accounts for the critical angle α at the pinning point. The second case considers the cluster as an additional stress field added to the external stress and can be expressed by the Peach-Koehler equation [55]. The equilibrium shape of the dislocation results from a balance between the dislocation line tension, the interaction between both partials, the interaction between partials and the stress field of solute atoms as well as the interaction between partials and the external stress field. Thus, in our case, the dislocation glide can be assimilated to a succession of metastable configurations separated by saddle points of variable energies. Contrary to other studies (see for example [56, 57 and 58]) where the theory of double-kink mechanism described the atomic level of the dislocation motion, here, the dislocation motion seems to be ruled by strong pinning and unpinning events due to solute solution.

For a relatively low MD strain rate, the motion of partials can be assimilated to a "stop and go" motion (see for example: [59, 60 and 61]) where the dislocation, after displacing for a few "solute valleys", is once again pinned because of the presence of clusters along the dislocation line.

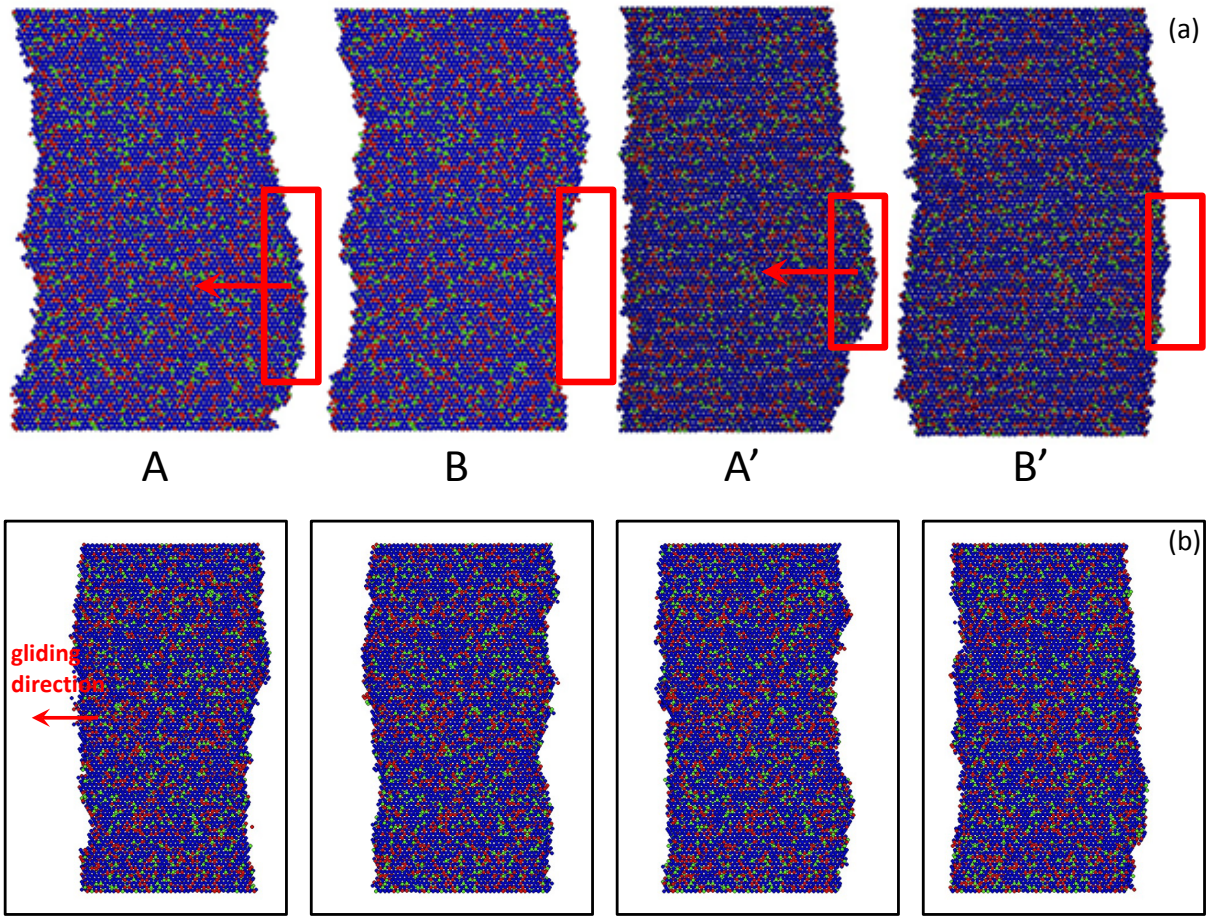

Figure 3.28: (a) Two sets of successive snapshots (A/B and A'/B') of the edge dislocation gliding during a stress drop for a strain rate of 10^6 s^{-1} with a time window of 100 ps between each frame. (b) Four successive snapshots associated to a 10^8 s^{-1} strain rate with a time window of 1 ps between each frame.

The displacement of the partials between two consecutive frames as a function of time is represented in Figure 3.29. Three cases are studied: (a) a dislocation velocity of 534 $m.s^{-1}$ and a time

window between each frame of 1 ps, (b) a velocity of 53.2 m.s^{-1} and a time window of 10 ps, (c) a velocity of 5.3 m.s^{-1} and a time window of 100 ps.

In this study, MD succeeds in reproducing correctly a "stop and go" motion for low velocities. For high dislocation velocity (534 m.s^{-1}), the displacement of the dislocation core is firstly incremental before reaching a stable displacement in time, which may mean that the dislocation core moves continuously and the pinning effect of the surrounding clusters is not strong enough to stop the motion. However, an extension or compression of the dissociated core can occur around the averaging displacement. Moreover, these variations seem to be equivalent for the leading and trailing partials.

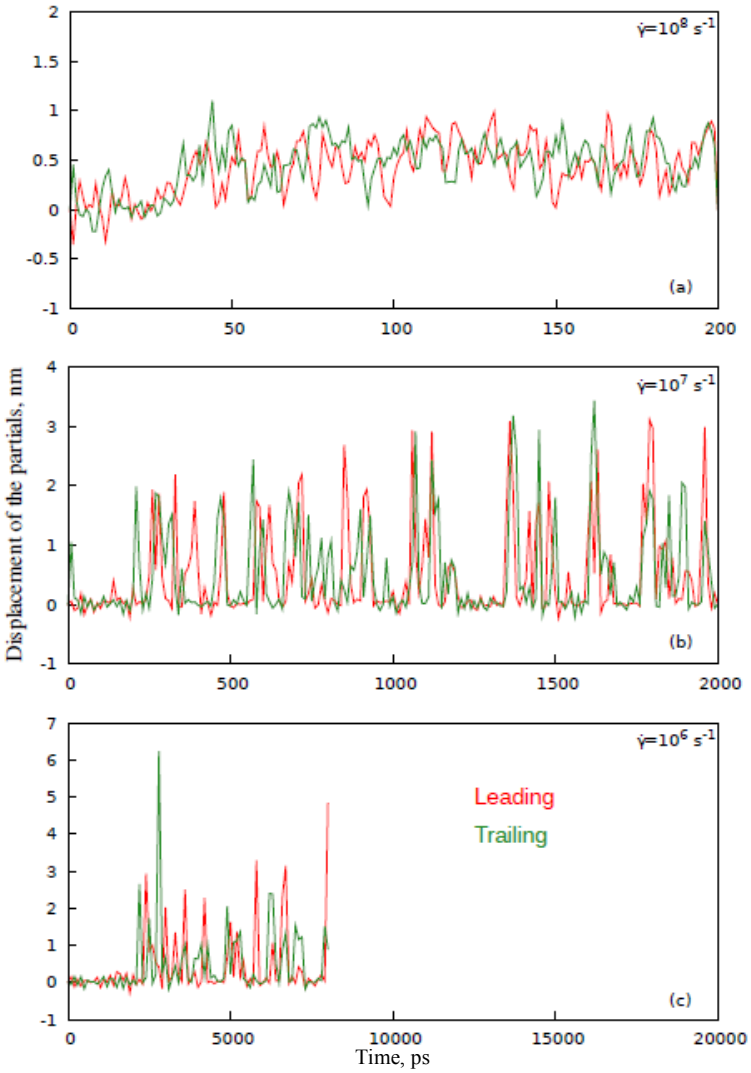

Figure 3.29: Displacement of Shockley partials for each unpinning event depending on time at 300 K for a dislocation velocity and frame interval respectively of 534 m.s^{-1} and 1000 steps (a), 53 m.s^{-1} and 10000 steps (b) and 5,3 m.s^{-1} and 100000 steps (c) [62].

We can observe that the first displacement is made by the trailing partial toward the leading one. This observation is in accordance with the elastic theory which predicts an impossibility of the leading partial displacement in the case of d_+ position. Thus, in such a case, the stacking fault area is higher than the equilibrium one and based on the direction of the applied stress, the leading partial

is unable to extend this non-equilibrium stacking fault area which can only be reduced by the motion of the trailing Shockley partial.

The simulation parameters which are supposed to affect the dissociation distance are the atomic configuration and the temperature. Indeed, the dislocation velocity affects neither d_0 nor the amplitude of the oscillations around the equilibrium position as it can be seen in Figure 3.30 where the dissociation distance is measured during deformation. On the other hand, the dissociation distance starts to decrease once the dislocation core starts to glide but, referring to Figure 3.30, the equilibrium position is reached when the crystal is sheared until ≈ 0.5% of deformation. This amount of deformation is independent of the dislocation velocity and temperature and can be assimilated to an incubation time to make the dissociated core reach d_0 once the dislocation starts to glide. The dissociation distance is intimately correlated to the distance crossed by the dislocation and it is clear when the dislocation starts gliding, that the dissociation distance decreases by ≈30% at 300 K and ≈15% at 900 K. This is in agreement with a temperature dependence of the SFE, as proposed in section 3.4.3. Another point is that the amplitude of oscillation around the equilibrium position seems also not to be affected by temperature.

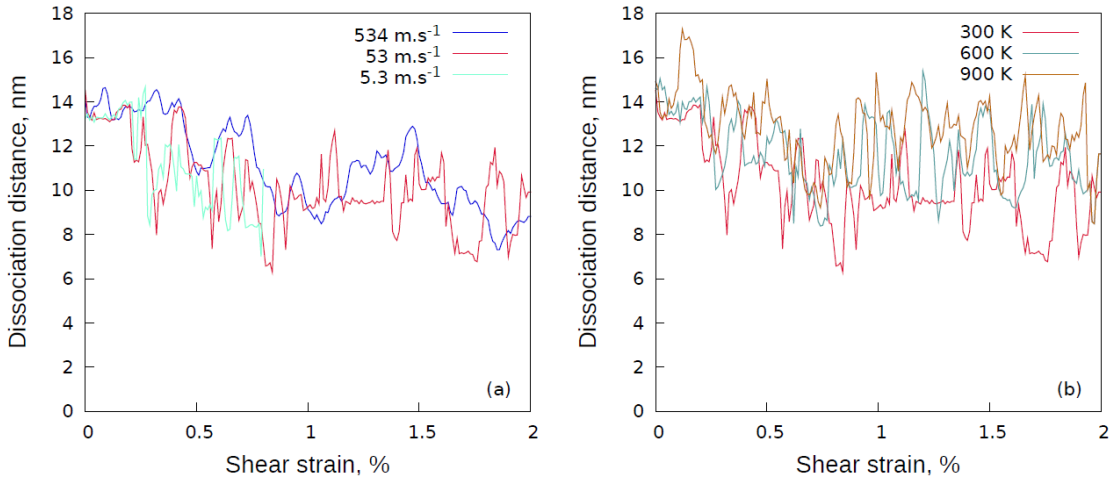

Figure 3.30: Dissociation distance evolution during deformation for different dislocation velocities at 300 K (a) and depending on temperature for a dislocation velocity of ≈55 m.s^{-1} (b) [62].

Regarding Figure 3.31, where the evolution of the position of the dislocation is plotted versus simulation time, in a case of a "stop and go" motion, pinning time seems also to decrease with $\dot{\gamma}$.

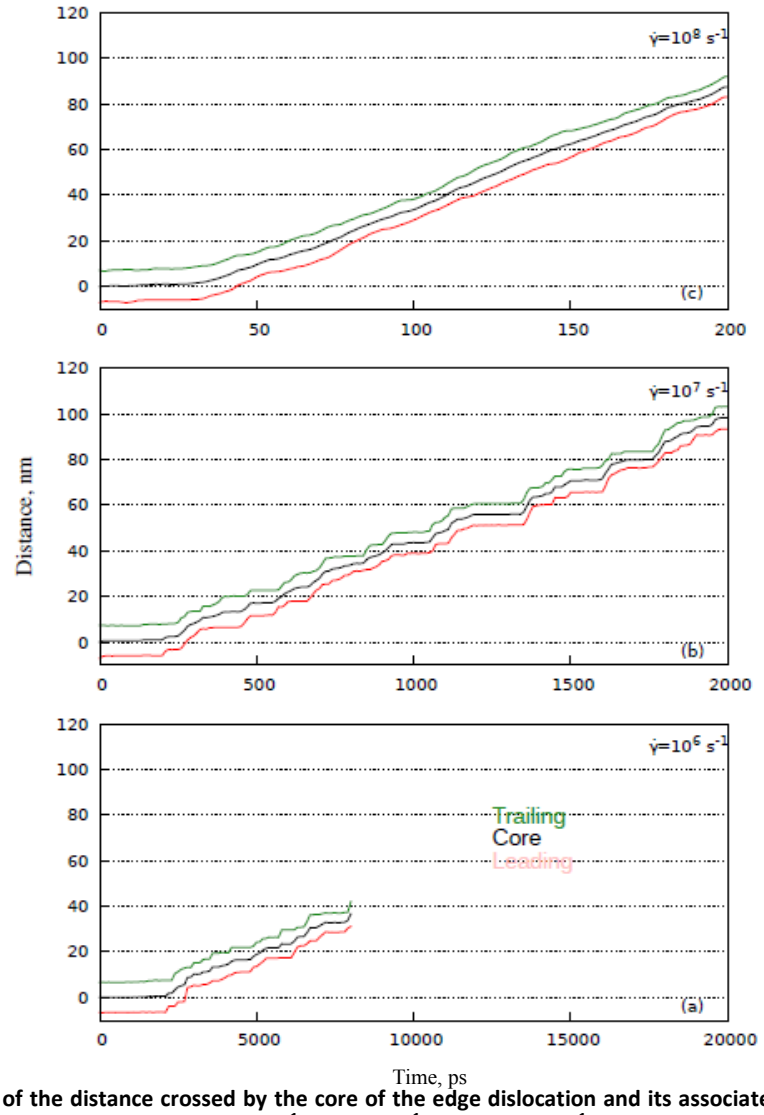

Figure 3.31: Evolution of the distance crossed by the core of the edge dislocation and its associated leading and trailing partial at 300 K for a dislocation velocity of 534 m.s^{-1} (a), 53 m.s^{-1} (b) and 5,3 m.s^{-1} (c) [62].

The temperature-dependence of critical stress τ_c is plotted in Figure 3.32 for three values of $\dot{\gamma}$. This critical stress is evaluated from the different stress peaks associated to the dislocation jumps. τ_c decreases strongly with temperature for low temperatures, as $\tau_{c,0K}$ has been evaluated at 620 MPa in quasi-static conditions. A comparison is made with the friction stress τ_f, associated here to a zero dislocation velocity.

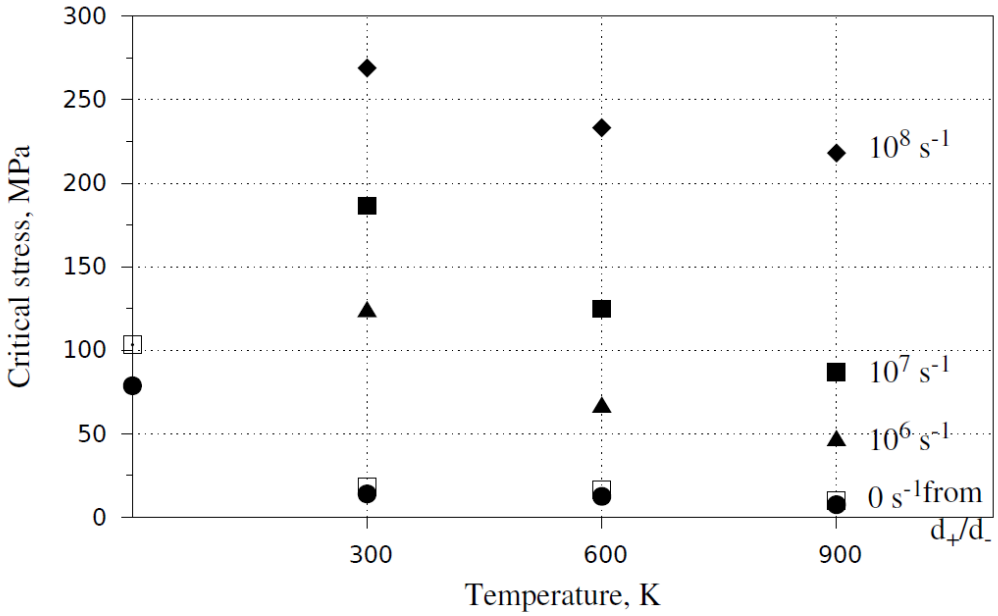

Figure 3.32: Evolution of the effective critical stress on the $(1\,\bar{1}\,1)$ plane as a function of temperature and fixed strain rate. The "zero velocity" corresponds to the friction stress results presented in section 3.5.4.

The critical stress has been evaluated for three strain rates and three temperatures. This trend reveals a strong dependence of the dislocation velocity in temperature which is apparently consistent with the experimental results developed. Note that the critical stress evaluated in static conditions is around 620 MPa. The calculated τ_c are equivalent to the 304 and 316 annealed materials used by Byun *et al.* in [63] at 300 K and, for higher temperatures (600 and 900 K), the τ_c determined at a strain rate of 10^8 s^{-1} are overestimated. Moreover, this effect of temperature is apparently emphasized for low strain rates. This temperature dependence can reveal a strong difficulty to nucleate and propagate extra-segments of Shockley partials, whereas once the system becomes dynamic, only the nucleation of these extra-segments is thermally activated, which makes the dislocation gliding easier.

3.6.4. Constitutive law

One of the main aims of this study is to provide fundamental data to a larger simulation scale, *i.e.* Discrete Dislocation Dynamics (DDD). It involves predicting the dislocation velocity in accordance with the stress. For this reason, it is necessary to establish a constitutive law, based on the empirical rule and previous models. Orowan links the shear rate to the dislocation velocity with the following law: the shear rate $\dot{\gamma}_0$ is proportional to the dislocation velocity v_D, the Burgers vector b and the density ρ_D of dislocations in such a way that

$$\dot{\gamma}_0 = \rho_D b v_D \tag{3.14}$$

The stress dependence of the dislocation velocity is obtained in random solid solutions and plotted in Figure 3.33. Once the local YS is reached, the dislocation starts to move in a more or less smooth manner regarding the position of the partials. It appears that from a given velocity, the dislocation motion is more continuous without any presence of pinning points (this last assumption depends on the time window taken between each frame of atoms). In that case, the dislocation velocity is near ≈0.1 C_s, where C_s is the sound velocity in austenitic stainless steel (C_s≈5000 m.s^{-1}) and glides in a much

less smooth manner. The two apparent velocity domains are separated at a ≈200 $m.s^{-1}$ dislocation velocity for 300 K. However, these two domains are clearly less identified at 600 and 900 K.

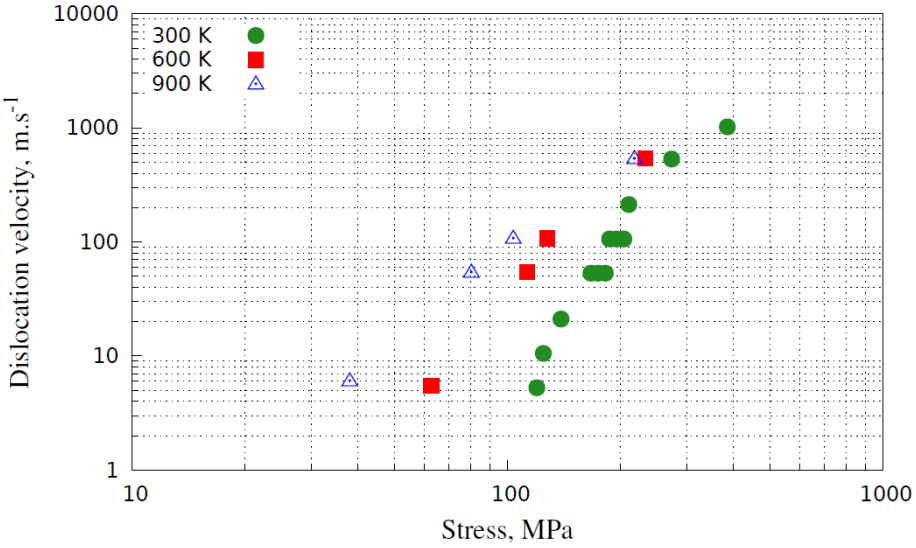

Figure 3.33: Effective glide velocity as a function of the applied stress depending on temperature.

The stress dependence of dislocation velocity above and below 200 $m.s^{-1}$ indicates a mobility law which seems to obey a power law function. The effect of seed numbers, although we are studying a random solid solution, leads to an equivalent shift to all velocities at a higher or lower stress. It is known that dislocations move by gliding at velocities which depend on the applied shear stress, alloying and impurities content of the crystal, temperature and orientation of the dislocation. By modifying the strain levels, the variation of the velocity as a function of the stress is identified. Experimentally, in the range of velocities between 10^{-9} and 10^{-3} $m.s^{-1}$, the variation has been found to be linear depending on the logarithm of the applied stress [21]. One possibility to define the stress dependence of dislocation velocity is the following power law formula, presented in section 3.2:

$$\upsilon_D = \upsilon_s(T)\left(\frac{\tau}{\tau_s}\right)^{n(T)} \tag{3.15}$$

where υ_s and τ_s are scaling factors, τ is the stress response measured and n is an exponent parameter. Figure 3.34 shows the dislocation velocity results as a function of the applied stress based on the constitutive law (3.15). In Figure 3.34, the raw (a) and rescaled data (b) are plotted versus stress response. The parameters determined in Figure 3.34 (c) and (d) are applied to the raw data of Figure 3.34 (a) to obtain the rescaled data of Figure 3.34 (b). The n parameter has been found to decrease linearly according to the temperature. From the fact that the parameters n and v_s vary with temperature and are not fixed, we must consider another type of law where the temperature effect is clearly stated. Thus, we choose to apply an exponential law to our model where the activation and temperature are taken into account.

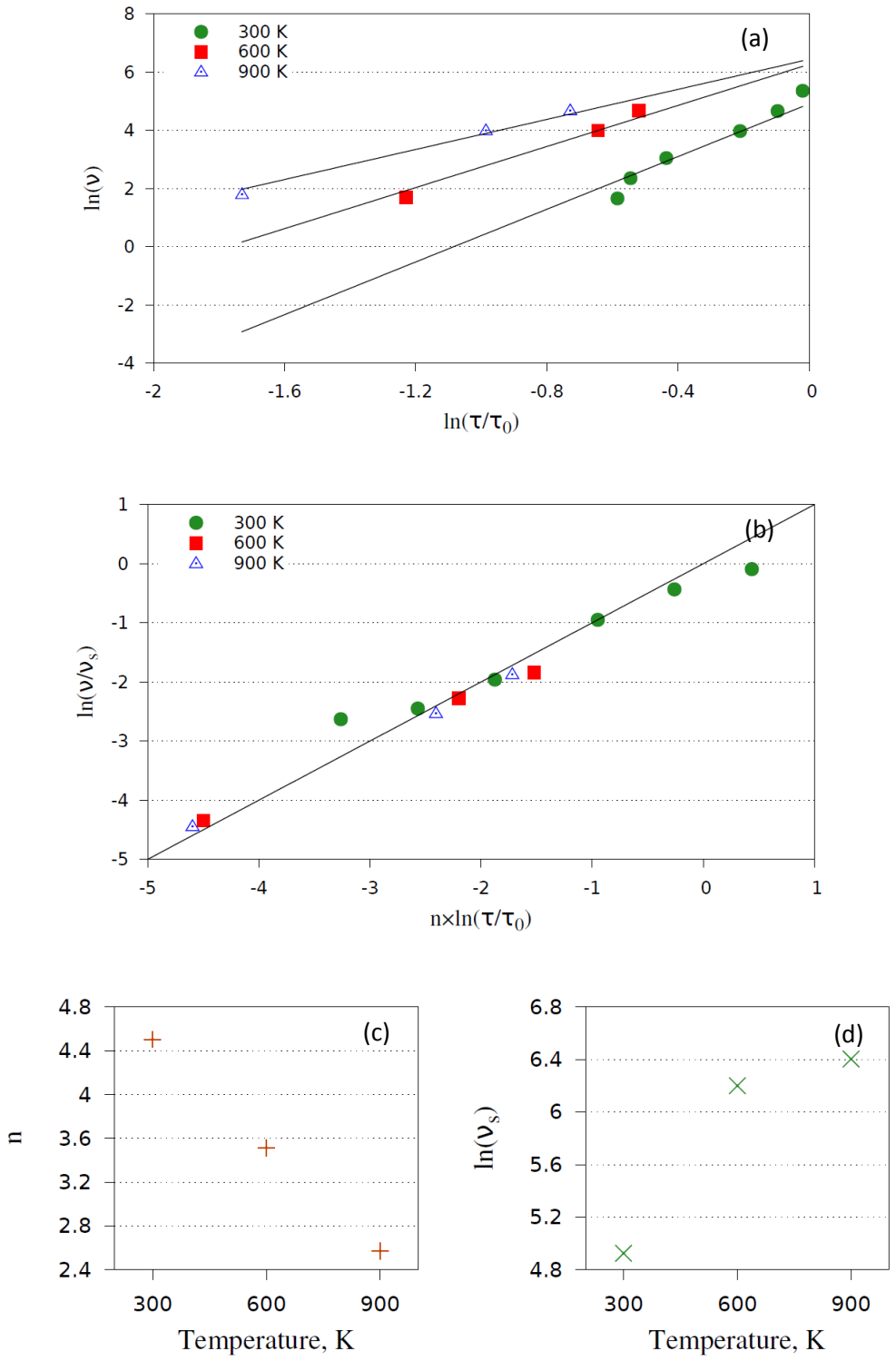

Figure 3.34: Stress dependence of dislocation velocity in the case of constitutive law (3.11). The first graph (a) represents the rough data and in the second graph (b) the rescaled data with the parameters deduced from (a) and represented in (c) and (d) in function of temperature.

Based on previous study using similar simulation technique (see for example Rodary *et al.* [64]), an exponential law, defined in section 3.2, is set to describe the motion of the edge dislocation. When the activation volume is constant, the velocity can be given by:

$$\nu_D = \nu_0 \exp\left(\frac{(\tau - \tau_0)V}{k_b T}\right) = \nu_0 \exp\left(-\frac{Q - \tau V}{k_b T}\right) \quad (3.16)$$

where V is the activation volume, T the temperature and k_b the Boltzmann's constant. τ_0 and ν_0 are rescaling factors.

The results obtained with the constitutive law defined in eq. (3.16) are represented in Figure 3.35 (a) using a different set of V and ν_0 at each temperature. The two fitting parameters, V and ν_0, are represented depending on temperature in Figure 3.35 (c) and (d). τ_0 is obtained by optimizing ν_0 and V parameters (see Figure 3.35).These parameters are used to fit the data represented in Figure 3.35 (b). By definition, V is not supposed to depend on temperature and should be constant.

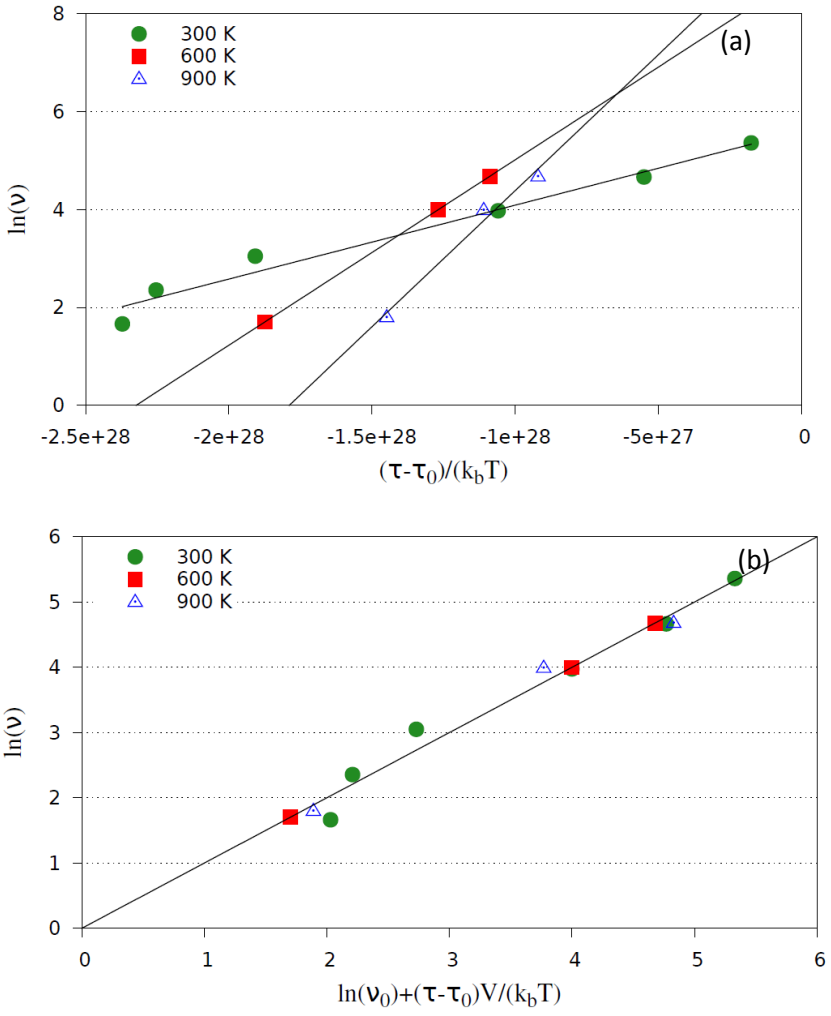

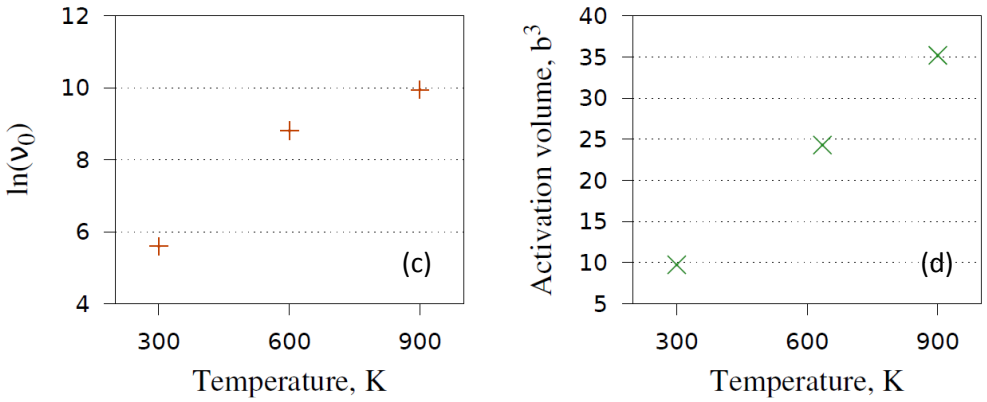

Figure 3.35: Stress dependence of dislocation velocity in the case of constitutive law (3.12). The first graph (a) represents the rough data. In (b) the data are fitted with the parameters represented in (c) and (d) depending on temperature.

The activation volume V and $\ln(v_0)$ are found to increase quasi-linearly with temperature. These parameters, once injected in the eq. (3.16), reveal a good alignment for the different temperatures. Basically, the power law model is strictly empirical and does not integrate any physical interpretations of the dislocation motion. Moreover the effect of temperature is not taken into account, which is not the case for the exponential law model. Thus, based on the assumption that the activation volume should be a parameter that is supposed to be fixed, the data are rescaled with a targeted V^*, τ_0 and $ln(v_0)$ for which the alignment is optimized. The data are represented in Figure 3.36. This gives an activation volume of ~11.6 b^3. However, the discrepancy between Figure 3.35 and Figure 3.36 is not so wide, which indicates the possibility to use the constitutive law (3.16), with the optimized parameters $\ln(v_0)$, τ_0 and V^*, for the next simulation scale, *i.e.* DDD (v_0=396 $m.s^{-1}$ and τ_0=218 MPa).

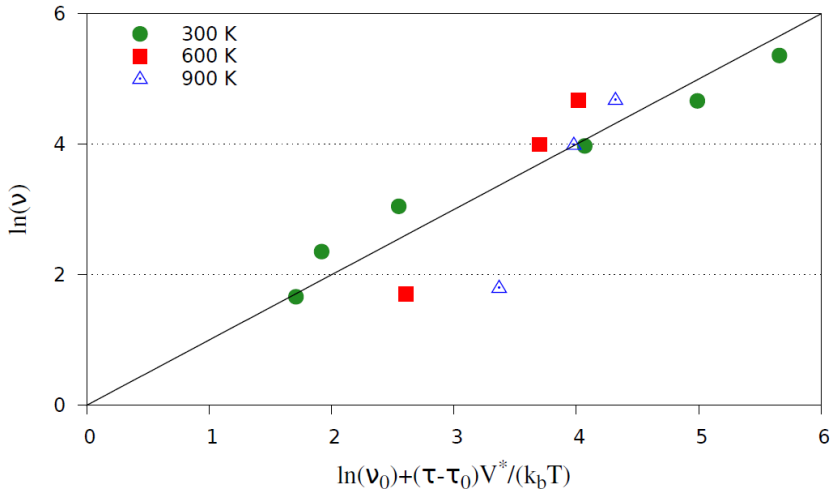

Figure 3.36: Stress dependence of dislocation velocity in the case of constitutive law (3.12) with an adjusted activation volume V^*=11.6 b^3.

The stress dependence of the edge dislocation velocity is similar to the one determined by Rodary *et al.* [64] where a saturation of the dislocation velocity shows up for very high value of stress and is linear for intermediate value. However, their two velocity domains are delimited by a dislocation velocity (~2000 $m.s^{-1}$) which is higher by a factor of 10 compare to our case (~200 $m.s^{-1}$). Two constitutive laws are applied to describe the motion of the edge dislocation. The aim of these

constitutive laws is to best reproduce the stress dependence of the dislocation velocity. The first constitutive law is a power law inspired from experimental models (see for example [24]), where the stress response is quite similar to the one observed in this study, *i.e.* there is apparently two different regimes of dislocation velocity. This power law integrates an exponent parameter n and two rescaling factors, τ_s and v_s. It appears that there is a temperature dependence of both v_s and n. However, this type of constitutive law is purely empirical. The other model involves temperature T, the rescaling factors v_0 and τ_0 and the activation volume V. It is important to note that there is no links between τ_0, τ_s and the friction stress τ_f. Although there is an apparent evolution of the activation volume with temperature, this last observation is not in contradiction with literature, where some authors exhibit a temperature and strain rate dependence of V, where V increased with temperature and decreased with the strain rate, as in this PhD thesis (see for example [22]). For this last model, an optimization of v_0, τ_0 and V leads to an accurate fit where the discrepancy between the different temperatures is minimized. The activation volume optimized here is $V \sim 11.6$ b^3. This value is quite elevated to experimental values which are lower than 8 b^3 in the case of austenitic stainless steels.

3.7. Conclusion

As an initial step, the potential properties have been investigated through lattice parameters and SFE for different compositions and temperatures. The lattice parameter is correctly reproduced, although the calculated values are quite underestimated compared to the experimental ones. The SFE value associated to the Fe-Ni_{10}-Cr_{20} composition matches well with the experimental results in static condition but decreases with temperature, which is not in accordance with the data available where an increase of this parameter is pointed out. The influence of alloying elements is limited in this study to static conditions where Ni and Cr increase SFE. This last observation is observed experimentally for Ni but not for Cr.

Secondly, the dissociation distance has been measured and used to determine the friction stress τ_f of the Fe-Ni_{10}-Cr_{20} material with an equation system that implies d_0, d_+ and d_- for two sets of effective isotropic elastic constants, the Voigt and the Reuss average. The temperature dependence of τ_f shows a strong influence (τ_f decreased by almost five from 0 to 300 K). In static conditions, τ_f is similar to the experimental value.

In a third part, the dislocation position dependence in time reveals two kinds of glide processes, if we consider the reliable time window. Under high shear strains, we observe that the dislocation glides continuously without any pinning events and under low shear strains, the dislocation motion is a succession of pinning and unpinning events where the dislocation jump from what can be assimilated to a "solute valley" to another. The two domains are delimited at 300 K by a dislocation velocity of 200 $m.s^{-1}$. This velocity is not clearly marked off at 600 and 900 K. Referring to the time dependence of the crossed distance, the dislocation well follows the Orowan's law. The strengthening due to solute solution appears to be rapidly overcome at 600 K, as demonstrated by the evolution of τ_c with alloying content.

Finally, to predict and describe the dislocation motion, two types of constitutive laws are applied to our model. The first one is a power law, purely empirical, and the second one is an exponential law where temperature is explicitly taken into account. The last one attests to the fact that it reproduces the stress dependence of the edge dislocation velocity and could be used in DDD to predict the motion of edge dislocation under a defined stress.

References

- CHAPTER III -

[1] D. J. Bacon, Y. N. Osetsky, **Dislocations in Solids**, J. P. Hirth and L. Kubin, Chap. 88.
[2] Y. N. Osetsky, A. Serra, V. Priego, **Interactions between mobile dislocation loops in Cu and α-Fe**, J. Nucl. Mater., 276 (2000) 202-212.
[3] M. Chassagne, M. Legros, D. Rodney, **Atomic-scale simulation of screw dislocation/coherent twin boundary interaction in Al, Au, Cu and Ni**, Acta Mater., 59 (2011) 1456-1463.
[4] R. Meyer, **PhD thesis** (1998) University of Duisburg.
[5] C. Becquart, **Report F16O-CT-2003-508840**, PERFECT IP Lille (2005) 22p.
[6] R. A. Johnson, **Alloy models with the embedded-atom method**, Phys. Rev., B 39 (1989) 12554.
[7] R. A. Johnson, D. J. Oh, **Analytic embedded atom method model for bcc metals**, J. Mater. Res., 4 (1989) 1195.
[8] R. A. Johnson, **Phase stability of fcc alloys with the embedded-atom method**, Phys. Rev., B 41 (1990) 9717.
[9] G. Bonny, D. Terentyev, R. C. Pasiannot, S. Poncé, A.Bakaev, **Interatomic potential to study plasticity in stainless steels: the FeNiCr model alloy**, Modelling Simul. Mater. Sci. Eng., 19 (2011) 085008.0000
[10] L. M. Brown, A. Thölen, **Shape of three-fold extended nodes**, Disc. Faraday Soc., 38 (1964) 35.
[11] I. M. Robertson, **The effect of hydrogen on dislocation dynamics**, 64 (1999) 649-673.
[12] L. Rémy, A. Pineau, B. Thomas, **Temperature Dependence of Stacking fault energy in close-packed metals and alloys**, Mater. Sci. Eng., 36 (1978) 47.
[13] H. Saka, T. Iwata, T. Imura, **Temperature dependence of the stacking-fault energy in pure Silver**, Phil. Mag., 37 (1978) 291-296.
[14] F. Lecroisey, B. Thomas, **On the variation of intrinsic stacking fault energy with temperature in Fe-18Cr-12Ni alloys**, Phys. Stat. Sol., 2 (1970) 217.
[15] R. M. Latanasion, A. W. Ruff, **The temperature dependence of stacking fault energy in Fe-Cr-Ni alloys**, Metall. Trans., 2 (1971) 505.
[16] C. G. Rhodes, A. W. Thompson, **The composition dependence of stacking fault energy in austenitic stainless steels**, Mettalurgical transactions A, 8 A (1997) 1901.
[17] A. P. Miodownik, **The calculation of stacking fault energies in Fe Ni Cr alloys**, CALPHAD 2 (1978).
[18] D. Goodchild, W. T. Roberts, D. V. Wilson, **Plastic deformation and phase transformation in textured austenitic stainless steel**, Acta Metall., 18 (1970) 1137.
[19] A. Kelly, G. W. Groves, **Crystallography and Crystal Defects**, ed. J. D. Arrowsmith, chapter 8, 255.
[20] R. W. Hertzberg, **Deformation and Fracture Mechanics of Engineering Materials**, 3rd edn (New York: Wiley) 67.
[21] D. Hull, D. J. Bacon, **Introduction to dislocations**, Butterworth-Heineman; 2001.
[22] W. S. Lee, T. H. Chen, C. F. Lin, W. Z. Luo, **Dynamic mechanical response of biomedical 316L stainless steel as function of strain rate and temperature**, Bioinorganic chemistry and applications, 2011 (2011) 13 pages.
[23] D. Rodney, **Activation enthalpy for kink-pair nucleation on dislocations: Comparison between static and dynamic atomic-scale simulations**, Phys. Rev., B 76 (2007) 144108.
[24] P. S. Follansbee, **An internal state variable constitutive model for deformation of austenitic stainless steels**, J. Eng. Mater. Technol., 134 (2012) 041007-10.
[25] F. J. Clauss, **Engineer's guide o high temperature material**, Addison-Wesley, Reading, MA.
[26] Y. N. Osetsky, D. J. Bacon, **An atomic-level model for studying the dynamics of edge dislocations in metals**, Modelling Simul. Mater. Sci. Eng., 11 (2003) 427-446.
[27] D. Rodney, G. Martin, **Dislocation pinning by small Interstitial loops: a molecular dynamics study**, Phys. Rev. Lett., 82 (1999) 3272-3275.
[28] V. V. Bulatov, W. Cai, **Computer Simulations of dislocations**, Oxford University Press, (2006).

[29] D. Rodney, **Molecular dynamics simulation of screw dislocations interacting with interstitial Frank loops in a model FCC crystal**, Acta Mater., 52 (2004) 607-614.
[30] C. L. Kelchner, S. J. Plimpton, J. C. Hamilton, **Dislocation nucleation and defect structure during surface indentation**, Phys. Rev., B 58 (1998) 11085-11088.
[31] P. Ehrhart, **Atomic Defects in Metals**, (NewYork: Springer, 1991) p 88.
[32] Y. Mishin, M. J. Mehl, D. A. Papaconstantopoulos, **Phase stability in the Fe-Ni system: Investigation by first-principles calculations and atomistic simulations**, Acta Mater., 53 (2005) 4029-4041.
[33] L. Malerba, G. J. Ackland, C. S. Becquart, C. Domain, S. L. Duradev, C.-C. Fu, D. Hepburn, M. C. Marinica, P. Olsson, R. C. Pasianot, J. M. Raulot, F. Soisson, D. Terentyev, E. Vincent, F. Willaime, **Ab initio calculations and interatomic potentials for iron and iron alloys: Achievements within the Perfect Project**, J. Nucl. Mater., 406 (2010) 7-18.
[34] J. D. Tucker, R. Najafabadi, T. R. Allen, D. Morgan, **Ab initio-based diffusion theory and tracer diffusion in Ni-Cr and Ni-Fe alloys**, J. Nucl. Mater., 405 (2010) 216-234.
[35] T. P. C. Klaver, G. J. Ackland, D. J. Hepburn, **Defect and solute properties in dilute Fe-Ni-Cr austenitic alloys: ab initio study**, Phys. Rev., B 85 (2012) 174111.
[36] P. Olsson, C. Domain (2011) **private communication**.
[37] F. Christien, M. T. F. Telling, K. S. Knight, **A comparison of dilatometry and in-situ neutron diffraction in tracking bulk phase transformations in a martensitic stainless steel**, materials characterization, 82 (2013) 50-57.
[38] M. Baeva, A. Beskrovni, S. Danilkin, E. Jadrovski, **X-Ray Diffraction and Neutron Diffraction Study of Fe-(15 to 29)Cr-11Ni-0.5N**, J. Mater. Sci. Lett., 17 (1998) 1169-1171.
[39] A. Beskrovni, S. Danilkin, H. Fuess, E. Jadowski, M. Neava-Baeva, T. Wielder, **Effect of Cr content on the crystal structure and lattice dynamics**, J. of Alloys Comp., 291 (1999) 262-268.
[40] X. Li, A. Almazouzi, **Deformation and microstructure of neutron irradiated stainless steels with different stacking fault energy**, J. Nucl. Mater., 385 (2009) 329-333.
[41] L. Vitos, J.-O. Nilsson, B. Johansson, **Alloying effects on the stacking fault energy in austenitic steels from first-principles theory**, Acta Mater., 54 (2006) 3821-3826.
[42] A. F. Wright, M. S. Daw, C. Y. Fong., **Theoretical investigations of (111) Stacking Faults in Aluminium**, Phil. Mag., A 66 (1992) 387-404.
[43] J. Xu, W. Lin, A. J. Freeman, **Twin Boundary and Stacking-Fault Energies in Al and Pd**, Phys. Rev, B 43 (1991) 2018-2024.
[44] T. S. Byun, **On the stress dependence of partial dislocation separation and deformation microstructure in austenitic stainless steels**, Acta Mater., 51 (2003) 3063-3071.
[45] J. B. Baudouin, G. Monnet, M. Perez, C. Domain, A. Nomoto, **Effect of the stress and the friction stress on the dislocation dissociation in face centered cubic metals**, Mater. Lett., 97 (2013) 93-96.
[46] D. L. Olmsted, L. G. Hector Jr., W. A. Curtin, **Molecular dynamics study of solute strengthening in Al/Mg alloys**, J. Mech. Phys. Solids, 54 (2006) 1762-1788.
[47] K. H. Lo, C. H. Shek, J. K. L. Lai, **Recent developments in stainless steels**, Mater. Sci. Eng., 65 (2009) 39-104.
[48] G. Monnet, M. A. Pouchon, **Determination of the critical stress resolved shear stress and the friction stress in austenitic stainless steels by compression of pillars extracted from single grains**, Materials Letters, 98 (2013) 128-130.
[49] M. C. Mangalick, N. F. Fiore, **Orientation Dependence of Dislocation Damping and Elastic Constants in Fe-18Cr-Ni Single Crystals**, Trans. Metall. Soc. AIME, 242 (1968) 2363-2364.
[50] R. Peierls, **The size of a dislocation**, Proceedings of the Physical Society, 52 (1940) 34-37.
[51] D. L. Olmsted, L. G. Hector Jr., W. A. Curtin, **Molecular dynamics study of solute strengthening in Al/Mg alloys**, J. Mech. Phys. Solids, 54 (2006) 1762-1788.
[52] N. F. Mott, F. R. N. Nabarro, **Report of a Conference on Strength of Solids**, The Physical Society, London, (1948) 1-19.
[53] J. Friedel, **Les Dislocations**, Gauthier-Villars, Paris (1956).

[54] U. F. Kocks, **A statistical theory of flow stress and work-hardening**, Phil. Mag., 13 (1966) 541-566.
[55] M. Peach, J. S. Koehler, **The Forces Exerted on Dislocations and the Stress Fields Produced by Them**, Phys. Rev., 80 (1950) 436-439.
[56] C. Domain, G. Monnet, **Simulation of Screw Dislocation Motion in Iron by Molecular Dynamics Simulations**, Phys. Rev. Lett., 95 (2005) 215506.
[57] J. Chang, W. Cai, V. Bulatov, S. Yip, **Molecular dynamics simulations of motion of edge and screw dislocations in a metal**, Computational Materials Science, 23 (2002) 111-115.
[58] W. Cai, V. Bulatov, S. Yip, A. S. Argon, **Kinetic Monte Carlo modeling of dislocation motion in BCC metals**, Materials Science and Engineering, A 309-310 (2001) 270-273.
[59] M. A. Lebyodkin, Y. Bréchet, Y. Estrin, L. P. Kubin, **Statistics of the Catastrophic Slip Events in the Portevin-Le Châtelier Effect.**, Phys. Rev. Lett., 74 (1995) 4758-4761.
[60] M. S. Bharati, M. Lebyodkin, G. Ananthakrishna, C. Fressengeas, L. P. Kubin, **The hidden order behind jerky flow**, Acta Mater., 51 (2002) 2813-2824.
[61] B. Devincre, L. P. Kubin, **Scale transitions in crystal plasticity by dislocation dynamics simulations**, Comptes Rendues Physique, 11 (2010) 274-284.
[62] A. Nomoto: **internal report MAI** (2013).
[63] T. S. Byun, N. Hashimoto, K. Farrell, **Temperature dependence of strain hardening and plastic instability behaviors in austenitic stainless steels**, Acta Mater., 52 (2004) 3889-3899.
[64] E. Rodary, D. Rodney, L. Proville, Y. Bréchet, G. Martin, **Dislocation glide in model Ni(Al) solid solutions by molecular dynamics**, Phys. Rev., B 70 (2004) 054111.

Chapter 4. Atomic scale study of irradiation hardening by interstitial Frank loops in a Fe-Ni_{10}-Cr_{20} model alloy.

The irradiation of reactor pressure vessel internals by neutrons during the operating time of nuclear power plants induces modifications of the microstructure resulting in the formation of black dots, Frank loops and voids/cavities [1]. These defects act as obstacles to the dislocation glide, causing hardening and embrittlement [2], thus limiting the lifetime of the component. In the case of PWR, the irradiated microstructure is composed mainly of Frank loops with a Burgers vector equal to $1/3\langle 111\rangle$ with a mean diameter of a few nm [3, 4, 5]. The plastic deformation leads to the emergence of channels or free defect areas [5]. The size and density of these channels were found to depend on SFE. The interaction of dislocations with Frank loops is certainly at the origin of the formation of these channels. However the mechanism leading to the formation of defect free zone need to be better understood. These channels indeed strongly influence the plastic deformation mechanisms and lead to plastic localization (until eventual failure) of irradiated stainless steels. The interaction mechanism between Frank loops and dislocations has already been investigated with Molecular Dynamics (MD) by Nogaret *et al.* [6] with a pure Cu EAM potential and by Terentyev et al. [7] with a FeNi EAM potential. Both potentials well reproduce SFE of austenitic stainless steels. However, a pure Cu potential does not take into account the Alloying effect, which cannot be limited to Ni. The alloying effect is here extended to Cr. MD simulations will be used here to study the precise interaction mechanism between a dislocation and a Frank loop in an FeNiCr model alloy. This contribution will shed some light on the formation of these channels.

This chapter is divided into two parts. In the first part, we recall briefly the effect of irradiation on the microstructure and on mechanical properties of austenitic stainless steels. Then we describe from the atomic scale to the macroscopic scale the mechanisms responsible for the hardening and the embrittlement of the internals. The second part deals with the description of interactions between an edge dislocation and a Frank loop through (i) a description of resulting configurations of both the Frank loop and the dislocation and, (ii) the strength and the resistance of the obstacle associated to this interaction. Finally, in a third part, we discuss the correlation between the interaction type and the associated resistance or strength of the obstacle.

4.1. Irradiation hardening mechanism: a multi-scale phenomenon

Neutron-irradiation of austenitic stainless steels conducts to generate irradiation defects in the materials. These obstacles have a strong pinning effect on dislocation gliding which induces an increase of the Yield Stress (YS) and Ultimate Tensile Stress (UTS) and simultaneously decreases the ductility of the material. Among the defect population, Frank loops are mainly responsible for the hardening, although cavities have the most pinning effect, their presence is revealed only for a high temperature of irradiation. So in the next section we will focus on mechanisms of interaction between Frank loops and dislocations, clear paths assimilated to clear bands formation due to this interaction and the mechanical macroscopic response.

4.1.1. Atomic scale

4.1.1.1. Description of the Frank loop

Irradiation conducts to generate defects of nanometric size which will interact with dislocations during deformation. The source of creation of these defects is due to some interaction between incident particles, in our case neutron, and atoms of the crystals. Two types of these interactions exist:

- inelastic interaction, between particles and electrons of the crystal. During this interaction, the particle loses its kinetic energy which move on to an excited state. The particle is slowed down by friction interaction, its trajectory is straight and the energy is dissipated in the form of heat. This mechanism does not create permanent defects in the material.

- elastic interaction, between incident particles and atomic nucleuses of the crystal. During this interaction, there is a direct transfer of energy, the slowdown is high and the incident particle is highly deviated from its initial trajectory.

In the case of elastic interaction, if the energy transmitted to the atom is higher than the threshold energy for displacement, the atom will be ejected. This energy is required to break bonds, displace atoms and relax crystal around the vacancy site. It has been evaluated to 15-40 eV for usual metals. In that case, a vacancy and an interstitial atom are created. Otherwise, the knocked atom stays on its site and energy is transmitted through phonons. The ejected atom can occupy another vacancy or interstitial site or knock other atoms. If its energy is sufficient, it can eject another atom and provoke a displacement cascade [8, 9].

In the core of the cascade, the temperature is highly elevated, and a lot of recombination occurred, leading to 70 to 90% of vacancy and interstitial recombinations [10, 11]. The remaining vacancies and interstitials will migrate to annihilate or constitute vacancy or interstitial clusters of a nanometric size.

The evolution of the population of irradiation defects can be observed by TEM when they have a nanometric size, but not for a displacement cascade which creates defects of sub-nanometric size for hundreds of picoseconds. The cascades can be studied by MD as the size and their life time are accessible to this modelization technique [12]. Then vacancies, interstitials and clusters obtained by MD can be used for a multi scale approach with the Monte Carlo method to study the coalescence of defects over a longer period, around hundreds of nanoseconds [13].

The irradiation of FCC metals by neutron particles induces atomic collision cascades, where self-interstitials and vacancies, migrate and coalesce to form point defect clusters. One of the formed clusters are hexagonal dislocation loops called Frank loops containing a stacking fault with the Burgers vector $\frac{1}{3}\langle 111 \rangle$ perpendicular to their habit plane. A schematic drawing of vacancy and interstitial Frank loop is represented on Figure 4.1.

The vacancy Frank loops are created by a condensation of vacancy in $\{111\}$ planes. The lacking plan creates an intrinsic stacking fault and inserts a faulted plan which disturbs the ternary perfect

sequence plan "abc" of $\{111\}$ planes in FCC. The interstitial loops are formed through a condensation of interstitial atoms between two $\{111\}$ plans, which conduct to insert a new $\{111\}$ plan, for example an "a" plan between a "c" and a "b" plan. This creates an extrinsic stacking fault composed by two $\{111\}$ successive plans. We can assume that the sides of interstitial Frank loops align with $\langle 112 \rangle$ directions according to the TEM observations made by Boulanger *et al.* [14], whereas the vacancy type is assumed to have its sides in the $\langle 110 \rangle$ directions according to the TEM observations conducted by Strudel *et al.* [15].

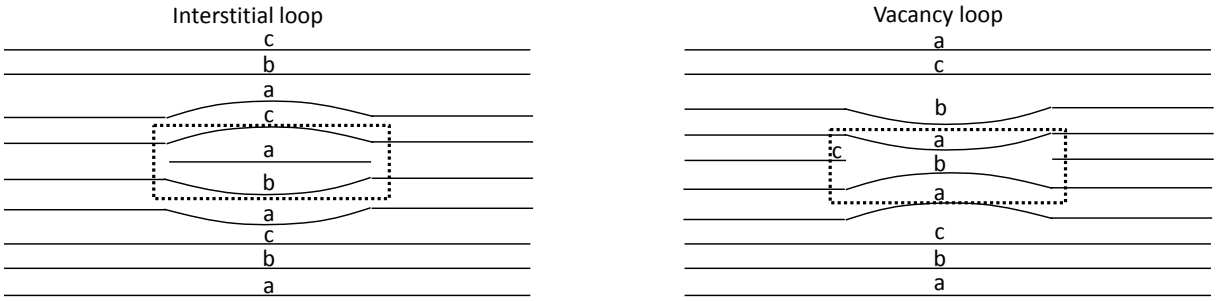

Figure 4.1: Schematic representation of two types of faulted loops.

Because Frank loops include an extrinsic or intrinsic stacking faults, they are sessile contrary to perfect loops, which are glissile. The stable character of Frank loops depends on the radius of the loop [16]. The nucleation and the growth of the dislocation loop can turn the faulted loop into a perfect loop. Inversely, a perfect loop can be decomposed into a faulted loop. This process depends on the variation of the energy *W* function as a function of the radius *r* of the perfect loop [16]

$$W(r) = \frac{\mu b_{FL}^2}{4\pi(1-\nu)} 2\pi r \log\frac{r}{b_0} - \pi r^2 \gamma + \pi b_0^2 \gamma \tag{4.1}$$

Where μ is the elastic modulus, ν is the Poisson's ratio, b_0=2(b_{FL}+b_{PL}), with b_{FL} the Burgers vector of the Frank loop and b_{PL} the Burgers vector of the perfect loop, r the radius of the perfect loop and γ the SFE. The variation of the energy *W* is represented in Figure 4.2. *W* becomes negative for $r > R_c$. In that case, the perfect loop is a stable solution. However, the Frank loop can constitute a metastable solution. When the SFE $\gamma < \gamma_c$, the energy *W(r)* shows a minimum for $r < b_0$ and a maximum at $r=r_c$. The first has no physical meaning, whereas the second is associated to a physical barrier of energy $W(r_c)$

$$W(r_c) = \pi r_c^2 \gamma - \frac{\mu b_1^2}{2(1-\nu)} r_c + \pi b_0^2 \gamma \tag{4.2}$$

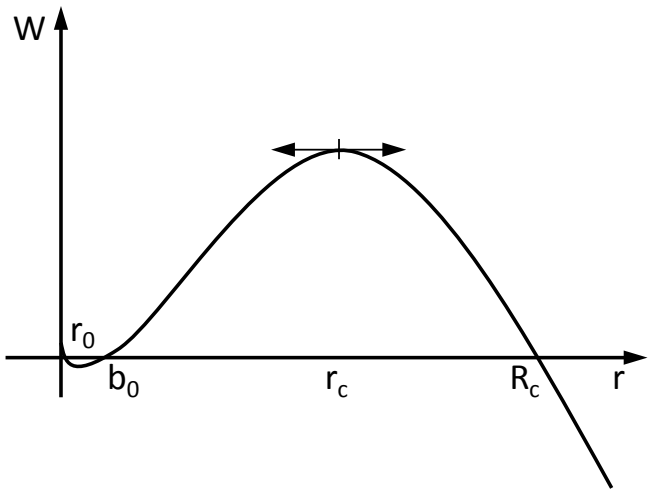

Figure 4.2: Variation of the energy *W* of a perfect glissile loop depending on the radius *r* when $\gamma < \gamma_c$ from [17].

Nevertheless, when the radius *r* of the loop is less than r_c the faulted type is more stable than the perfect loop and inversely when *r* is higher than r_c . Nevertheless, the probability to form a perfect loop at a lower radius is higher than the probability to form a faulted loop at a higher radius, especially when $R >> r_c$.

Observations of interstitial and vacancy Frank loops by the electron microscopy show that some of them are unfaulted, *i.e.* the stacking fault inside a loop is removed and a sessile Frank loop of the Burgers vector $\frac{1}{3}\langle 111 \rangle$ is transformed into a perfect glissile dislocation loop of $\frac{1}{2}\langle 110 \rangle$ type. In some cases like in aluminum, due to the high SFE value, the perfect loop is favorable energetically for any size of dislocation loop [16, 18]. The mechanism for the transformation into a perfect dislocation loop is predicted theoretically: a Shockley partial is created and sweeps across the loop to remove the stacking fault. In a case of a vacancy Frank loop, only one partial is needed to eliminate the fault, while two partials are required for an interstitial Frank loop. An observation of the unfaulting process has been done by Kadoyoshi *et al.* [19] for both vacancy and interstitial Frank loops under shear strain rate conditions. The initiation of the unfaulting process is similar to the theoretical mechanism proposed by Kuhlmann-Wilsdorf [20]. The unfaulting mechanism is represented on Figure 4.3.

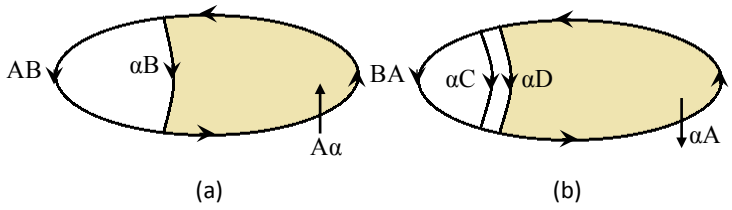

Figure 4.3: Unfaulting mechanism for a (a) vacancy and (b) interstitial type.

For a vacancy Frank loop, the unfaulting mechanism required only one partial moving along the faulted area with the following reaction: $A\alpha \rightarrow \alpha B + AB$. So the partial dislocation sweeps the intrinsic fault and turns the Frank loop into a perfect prismatic loop of AB Burgers vector. Considering the unfaulting mechanism for interstitial Frank loop, two partials are required to remove the faulted area with the following reaction: $\alpha C + \alpha D + BA = \alpha A$.

4.1.1.2. Description of perfect loops

As shown in section 4.1.1.1., Frank loops can turn into a perfect dislocation loop with a Burger vector of $\frac{1}{2}\langle 110 \rangle$ after one or two Shockley partials with a Burgers vector of $\frac{1}{6}\langle 112 \rangle$, which lie in the Frank loop plane, remove the stacking fault. This loop is bounded by a perfect loop and is glissile. The perfect loop tries to align along the $\langle 110 \rangle$ directions which are favorable in the FCC system. The atom positions, after the unfaulting process of a vacancy and interstitial Frank loop, are represented in Figure 4.4.

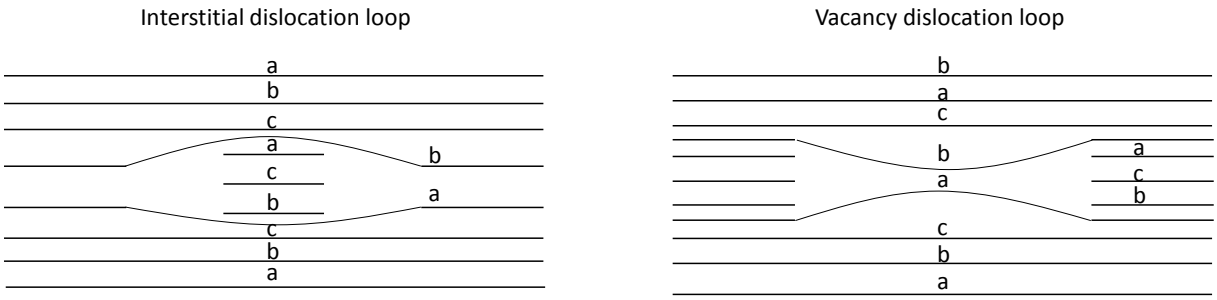

Figure 4.4: Perfect loops formed by the unfaulting reactions.

4.1.1.3. Description of Cavities

During irradiation, point defects can be eliminated on "fixed gaps". When interstitials are preferentially eliminated on dislocations, it can result a supplementary vacancy flux on small vacancy clusters. If these clusters are tridimensional, cavities can be generated and induce swelling in the material. The stability of cavities has been observed by the presence of insoluble helium bubble gas, which comes from the nuclear reaction. When the helium pressure inside the cavities is elevated, the cavities turn into helium bubbles.

Thus, the production rate of helium is a parameter which can affect significantly the swelling of the material. The evolution of swelling is characterized by two successive phases:

-cavities can nucleate inside the microstructure, which constitute the incubation period;

-a second phase which consist in a swelling at constant speed directly linked to the growth of cavities and their coalescence.

Nevertheless, swelling required a high temperature of irradiation, which explains why this phenomenon has been studied in austenitic stainless steel in fast neutron reactors, but not in PWR.

4.1.1.4. Interaction between dislocation and irradiation defects

Mobile dislocations interact with the irradiation defects. These interactions have been studied by Strudel *et al.* with TEM in the case of vacancy loops [15] and by Boulanger *et al.* [14] in the case of interstitial loops. These interactions have been simulated in pure material by Rodney *et al.* [21, 22] and Nogaret *et al.* [6]. Cavities interaction with dislocations has been widely studied in α-Fe [23, 24, 25, 26]. Concerning the FCC system, only few studies have been conducted with pure Cu potential [27, 28]. These studies reveal that the core of the dislocation plays a key role in the mechanical response, especially for dissociated dislocation. When the size of the void is less than the dissociated distance, the Critical Resolved Shear Stress (CRSS) is lower in Cu than in α-Fe where the

core of the dislocation is non-dissociated. When the size of the void is higher or equal to the dissociation width, the CRSS response is similar to a CRSS response of a perfect dislocation.

Four types of interactions have been identified by Bacon *et al.* [29] based on the character of the dislocation and on whether the Frank loop is unchanged, absorbed or unfaulted after the passage of the dislocation. Moreover, two other types of interactions have been identified (see recent studies [7, 30]). Some reactions which are detailed here are specific to Frank loops and are not observed for other type of defect like Stacking Fault Tetrahedron (SFT) (see for example [31]).

Reaction R1: the Franck loop is crossed by the dislocation and both are unchanged

The Frank loop is sheared by the dislocation and is left behind as it was unchanged. A step can be created at the edge of the defect but as it is highly mobile, it disappears or recombines. This reaction has been observed for both screw and edge characters. The requirement to observe this mechanism is a low temperature and a low shear strain $\dot{\varepsilon}$ (*i.e.* the dislocation velocity v_D). Apparently, the stress response associated to this reaction is a low stress τ_c.

Reaction R2: the Frank loop is modified and the dislocation is unchanged

This occurs in two instances. First, the step which is created at the edge of the Frank loop is stable. Secondly, loops can be transformed into a mixed loop with two different Burgers vectors. Some of the loops in Body Centered Cubic (BCC) metals are turned into both faulted and perfect ones, *i.e.* mixed loops [32].

Reaction R3: the Frank loop is partially or completely absorbed by the edge dislocation which acquired a double superjog

The reaction occurs for loops in two situations. b_L of small loops changes on contact with the dislocation to adopt the same Burgers vector as the dislocation. This reaction occurs when the Frank loop is close to the glide plane and small and is favored with a high temperature *T* and a low velocity v_D of the dislocation. Another possibility of this mechanism is when a segment of the Frank loop is on the glide plane of the edge dislocation. At that moment, the dislocation absorbs a part of the Frank loop after the Burgers vector b_L of this part becomes similar to the Burgers vector of the dislocation.

Reaction R4: interaction without any contact

This mechanism has been observed by Strudel *et al.* in TEM [15]. They have identified a perfect loop which has reached the surface by prismatic glide. So sometimes an imperfect loop is converted into a perfect loop and can glide without interacting and without any contact with the moving dislocation. This can be explained by the strong strain field which is generated by the dislocation. This strain field induces an elastic interaction between the dislocations and the Frank loop and unfaults the loop. MD simulations have not succeeded in reproducing this mechanism, because this is a thermally activated mechanism, such that the incubation time cannot be reached through MD.

Reaction R5: Unfaulting of the loop after interaction with the dislocation.

This interaction has been identified by Strudel *et al.* [15], where the dislocation does not lie in the same plane as the Frank loop. The Burgers vector of the dislocation is dissociated in its slip plane and two nodes N_1 and N_2 are created between the Frank loop and the dissociated dislocation. If the

dislocation is then pulled away from the previous sessile Frank loop, this last one is changed to a perfect prismatic loop type. The final Burgers vector of the loop will be either CB or DC (see Figure 4.5).

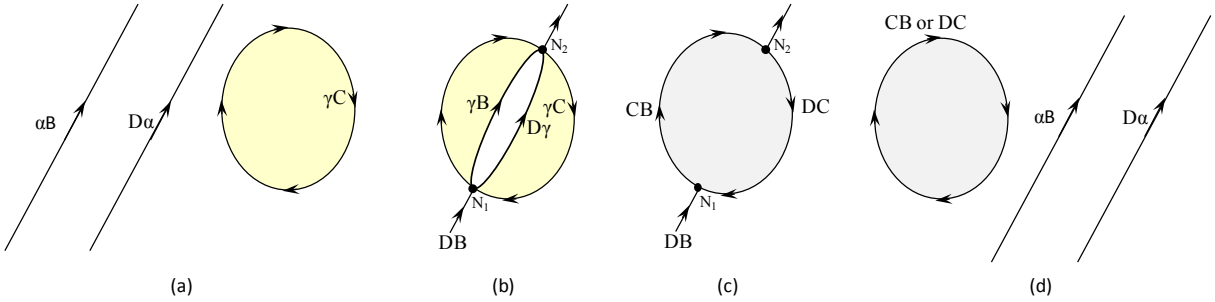

Figure 4.5: Reaction R5: Unfaulting of a Frank loop when the dislocation does not lie in the same plane of the dislocation.

Reaction R6: unfaulting of the loop and partial or complete absorption by the dislocation.

This mechanism is similar to mechanism R5 except that one part or the entire defect is absorbed. If we consider reaction R4, a part or the total absorption of the dislocation can be observed by the mechanism represented on Figure 4.6.

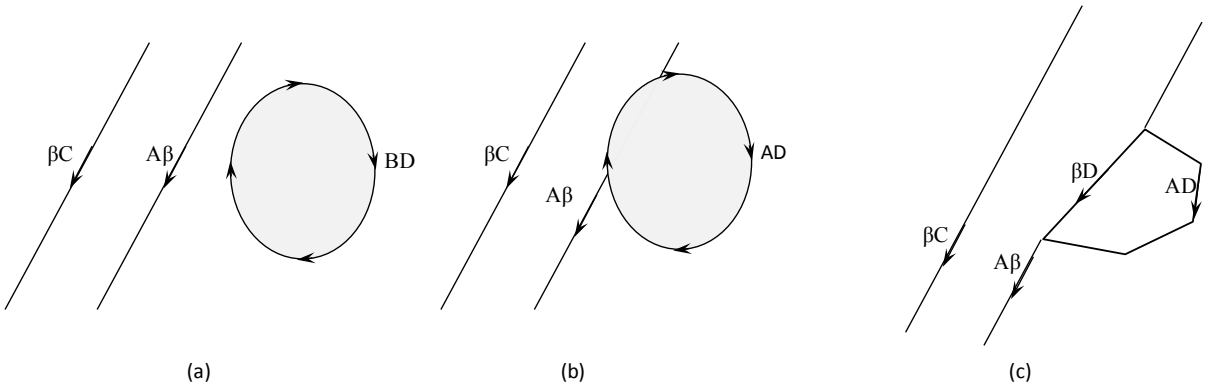

Figure 4.6: Reaction R6: Dislocation structure after absorption of a perfect interstitial loop and corresponding Burgers vector geometry.

The cluster glides when it is attracted by the dislocation and stops when it reaches the dislocation core. The Burgers vector of the perfect interstitial loop slips to another direction due to a rotation of the Dumbbell from an initial direction of $\langle 100 \rangle$ to a new $\langle 100 \rangle$ direction. This slipping depends on the orientation of the partial Burgers vector. A junction is then created between the partial Burgers vector and the perfect dislocation loop. This reaction has been observed only in simulation by Rodney *et al.* [33].

Another possibility of absorption is similar to reaction R5 except that after unfaulting, a part of the unfaulted interstitial Frank loop is absorbed by the dislocation. In this case, after the partial has swept the upper and lower part of the faulted interstitial loop, two perfect dislocation loops of different Burgers vectors are generated.

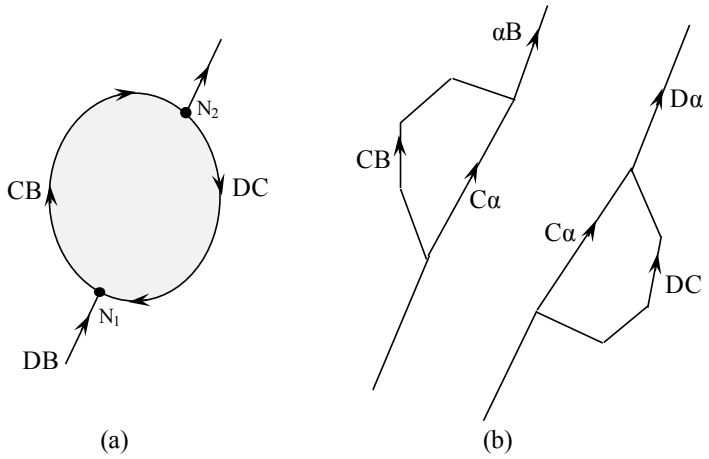

Figure 4.7: Reaction R6: Absorption of the perfect dislocation on both partials after Frank loop has been unfaulted by the mechanism R4.

The two different halves of perfect loops from the unfaulted loop are glissile but in different directions corresponding to their respective Burgers vector. Thus, as the dislocation proceeds, the two halves are dragged in opposite directions and end up being separated attached to the core of the dislocation on their associated leading or trailing partial.

4.1.2. Grain scale: structure and formation of clear bands

The absorption of the defects has been observed to occur in a specific area according to TEM observations. These areas are cleared of defects and constitute a specific zone for the dislocation to glide. These specific zones are called "clear bands" and accomodate all the deformation in the material. These clear bands have been observed in many irradiated and deformed materials and among these materials, austenitic stainless steel has been subjected to investigation by Byun *et al.* [34] and Lee *et al.* [35].

Clear bands have a multi-scale structure, which starts from slip lines where 25 nm steps are created at the surface. These lines are packed around 5 and 10 lines spaced by 10 nm. These slip bands are merged in 5 or 10 bands spaced by 1 µm which conduct to form slip band bundles. Neuhauser *et al.* [36] assume that the slip bands thickened through the nucleation of a new slip line from a previous slip line.

Clear bands, from TEM observations, have been demonstrated to spread along all the grain and have a constant width which is around 25 nm for an austenitic stainless steel [37]. During deformation, strain is confined in the channel and is uniformly distributed in the channel through the width. Since the $\{111\}$ interplanar distance for stainless steel is 0.206 nm, these dimensions indicate that channeling involves ~120 adjacent $\{111\}$ planes.

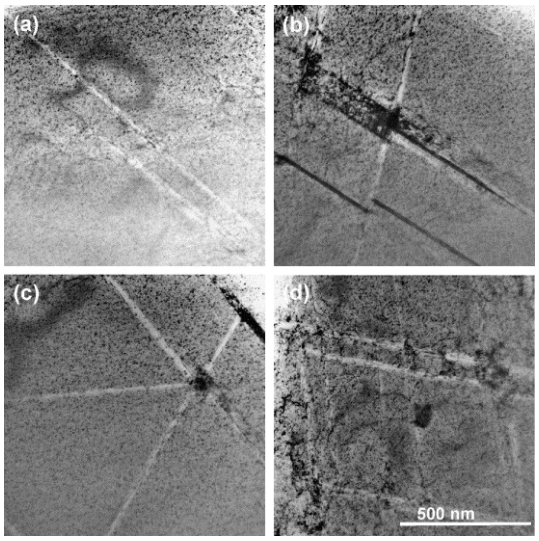

Figure 4.8: Channelled microstructure in 316 stainless steel after neutron irradiation to 0.78 dpa at low-temperature (a) 2%, (b) and (c) 5% and (d) 32% strains [37].

Clear bands are formed by the successive passage of the dislocation on specific bands which have conducted to absorb the remaining irradiation defects. A formation of clear bands has been observed by TEM.

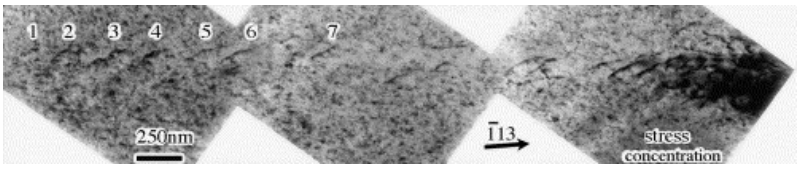

Figure 4.9: Dislocation emission from a propagating crack and the formation of a defect-free channel [38].

The micrography on Figure 4.9 has been realised by TEM by Robertson *et al.* [38]. It shows a clear band formed by the successive gliding and stacking of seven dislocations emitted from a crack.

Clear band formation has been simulated by Nogaret *et al.* [39] in austenitic stainless steel thanks to Dislocation Dynamics (DD). The gliding of the dislocations has been conducted in a random population of Frank loops. They revealed that the absorption of Frank loops in a helical turn is the heart of the process of clear band formation. Moreover, one dislocation cannot create a clear band as the clearing process would be limited to one $\{111\}$ primary plane. Thus, a pile-up of the dislocation is requested. Nevertheless, due to computation time, only the first stage of the clear band formation was simulated in a small grain.

4.1.3. Multigrain scale

The mechanism required initiating channels, or clear bands, and their subsequent evolution as a function of the strain is not well understood [40]. Some of the channels have been observed to propagate through the twin and grain boundaries, but in some cases, they are stopped at such obstacles. Due to these interactions, clear bands are known to promote grain boundary crack initiation and propagation. As it has been evidenced by TEM observations, the channel length *L* is usually the size of the grain size.

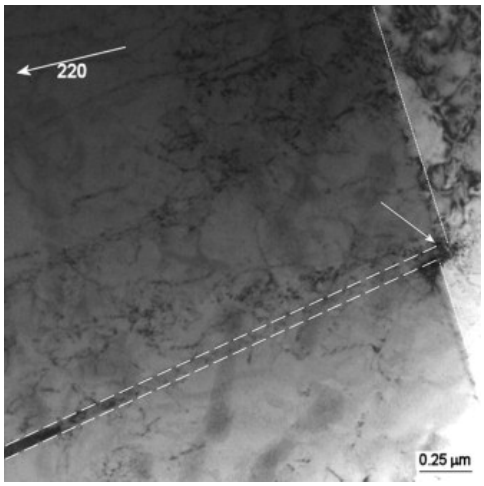

Figure 4.10: Interaction between a channel and a grain boundary (see the white arrow). The grain boundary is sheared because of the channel glide [41].

Figure 4.10 shows the interaction of a channel with a grain boundary which is deformed due the channel glide. Finite Elements (FE) computations are simulation methods which allow comparing the channel slip at the free surface, where no constraint effect occurs, and at the grain boundaries. Sauzay *et al.* [41] used both plane stress or plane strain conditions, with a mesh width which is either very small or very large. The meshes are 3D ones, made of tetrahedral. The CRSS is adjusted from the experimental data such as YS and hardening curve, and physically based models like MD from the literature. It appears that the surface slip depends linearly on the ratio L/h, with *L* the grain size of the material and *h* the channel thickness. The matrix CRSS, the channel and the ratio L/h have been demonstrated to be the most influential material parameters on the grain boundary slip.

4.2. Effect of irradiation

4.2.1. Microstructure evolution

Dislocation loops and cavities formation has focused great attention. However, only few contributions study the formation of these defects in real conditions of irradiation (temperature, flux, irradiation type). For example, Pokor *et al.* [42] has measured the density and size of Frank loops after neutron irradiation at 320°C and 375°C (~10 dpa) in the experimental BOR-60 reactor. Pokor observed the microstructure of a 304 annealed material and 316 cold-worked stainless steel with a Transmission Electronic Microscope (TEM) (see Figure 4.11).

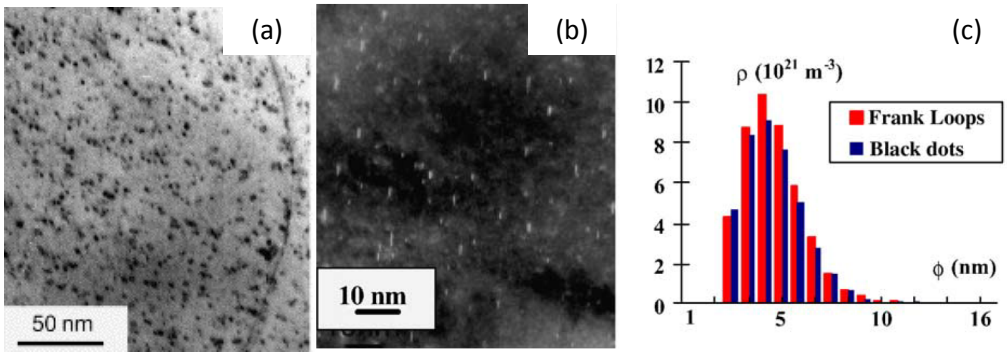

Figure 4.11: Microstructure of the 304 alloys irradiated at 330 °C with 0.8 dpa (from [42]).

A typical microstructure of irradiated stainless steel is shown in Figure 4.11. TEM bright field image (a) shows black dots whereas dark field (b) image reveals Frank loops. From the comparison of the

size distribution of black dots and Frank loops (see Figure 4.11 (c)), Pokor *et al.* assumed that these two objects were one single defect. However, there is a controversy in the literature concerning these black dots: some studies [3, 4, 43 and 44] claim that black dots are small Frank loops of a diameter less than 2 nm. Cavities or bubbles are also observed after large irradiation dose (see Figure 4.12 from [42]).

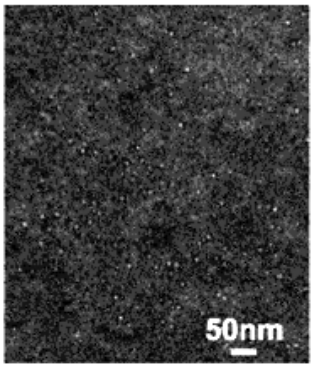

Figure 4.12: Microstructure image of cavities/bubbles in a CW 316 bolt neutron irradiated at 365 °C for a dose of 13 dpa [42].

Dislocation loops and cavities are the main defects observed after neutron irradiation of stainless steel. We report here the characterization of the irradiation defects from a few studies [6, 45, 46 and 47]. The Number density and size of dislocation loop and voids are represented in Table 4.1. Note that many authors assume dislocation loop and Frank loop are the same.

Table 4.1: Measurements of dislocation loop and void characteristics in neutron irradiated 316SS.

Ref.	Dose (dpa)	T (°C)	Frank Loop diameter (nm)	Frank Loop density (m^{-3})	Void diameter (nm)	Void density (m^{-3})
[42]	8	375	12.1	3.2×10^{22}	n.m.	n.m.
	10	375	12.2	3.2×10^{22}	4.6	few
	10	330	7.5	6.0×10^{22}	n.o.	n.o.
	20	330	7.4	4.4×10^{22}	n. o.	n.o.
[45]	12	360	n.m.	n.m.	10	2.3×10^{21}
[46]	19.5	320	6.9	9.2×10^{22}	<2	$<10^{20}$
	12.2	343	9.5	8.5×10^{22}	8.6	6.1×10^{21}
	7.5	333	12.5	1.2×10^{23}	7.7	1.0×10^{22}
[47]	13.3	275	9.4	1.9×10^{23}	-	-

(n.m.) Not measured, (n.o.) not observed, (-) not mentioned

The higher the temperature, the lower the dislocation loop density is. Concerning void, the size is affected by the dose and void density adopts the same trend as dislocation loop with temperature and dose.

The chemical analyses on 316 stainless steels, extracted from a PWR, have been carried out using Atom Probe Tomography (APT). These analyses show that irradiation has a strong effect on the

distribution of solute atoms [45]. More particularly, the Frank loops can be enriched in Ni and Si which can be explained with the Radiation Induce Segregation (RIS) mechanism. This phenomenon has also been observed by A. Volgin on a FeNiCr and FeNiCrSi materials [48] where Ni and Ni-Si atmospheres are formed around dislocation loops.

4.2.2. Mechanical properties evolution

Figure 4.13 displays typical engineering stress-strain curves from ref. [49]. The transition from elastic to plastic deformations occurred smoothly in a non-irradiated specimen. This transition appears sharper after irradiation. The total strain hardening during uniform deformation decreased with the increasing dose, while the Yield Stress (YS) increased proportionally with the decreasing of the total strain with irradiation dose. Generally, radiation induces an increase in YS associated to a loss of ductility in reference to the non-irradiated material.

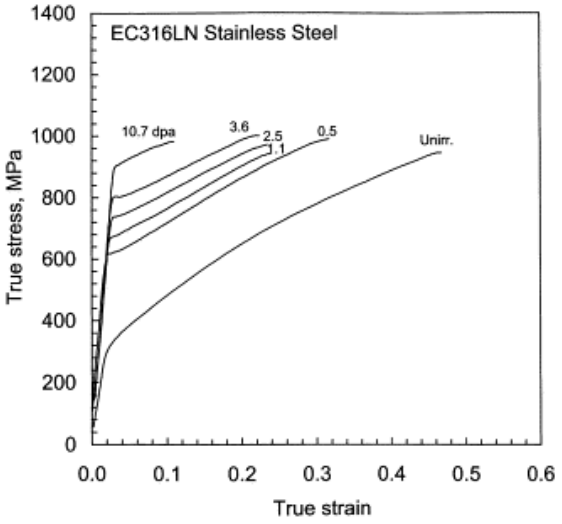

Figure 4.13: True stress strain curves of an annealed 316 stainless steel after irradiation to labeled doses in a spallation environment [49].

For austenitic stainless steel, like for other vessel internals of PWR, in the temperature ranges included between 300 and 350°C, neutron-irradiation induces high modifications of the microstructure. Irradiation dose can reach 80 dpa in most irradiated zones after 40 years of services. Depending on the irradiated temperature, the following intragranular microstructural obstacles are observed:

-Frank loops are sessile with an asymptotic evolution and saturation, which is reached for a certain dose depending on temperature. As the temperature increases, the loops density decreases whereas the size increases;

-creation of cavities or gas bubbles;

-segregation and inducing precipitation under irradiation like γ' Ni_3Si type.

4.2.3. Bibliography summary

Austenitic stainless steels are used as internals in a PWR and suffer from neutron irradiations at around 300 °C. These irradiations lead to the formation of interstitial Frank loops with sizes ranging from 7 nm to 13 nm and a saturation density of 10^{23} m^{-3}. The TEM observations confirmed that irradiated austenitic stainless steels deform with the gliding of dislocations and their interactions

with the irradiation defect. These interactions conduct to absorb the obstacle and form bands free of defects, called clear bands or channels. The plasticity of irradiated austenitic stainless steels is a multi-scale phenomenon where deformation is located in the channels. Many studies have highlighted the possible mechanisms of interactions at the atomic scale but few are dedicated to the effect of alloying elements in FCC system. However, the previous results have revealed three resulting interaction mechanisms, namely shearing, unfaulting and absorption, the latter being responsible for clear bands.

4.3. Interactions between faulted Frank loop and edge dislocation

As Frank loop is the basis of irradiation damage, it requires qualitative data. The previous studies [22, 6, 33, 51] have been done on pure material (Ni and Cu) or binary alloy [7]. One of the major contributions of this study is the combined effect of Ni and Cr. Moreover, contrary to previous studies, a special attention is paid to the resistance of the obstacle. In this part, austenitic 304 and 316 stainless steels are modeled with a random solute solution Fe-Ni_{10}-Cr_{20}. This chapter focuses on the interaction mechanisms of an edge dislocation and a Frank loop depending on the four different possible $\langle 1\,1\,1 \rangle$ orientations that Frank loop can adopt, at three temperatures (300 K, 600 K and 900 K) and for three random alloying configurations. To investigate the dose level received by the material, the reactions are conducted for 2 Frank loop sizes which are 2 nm and 10 nm. In this section, two kinds of data are supplied, the resulting configurations and the maximum stresses resulting of these interactions. The elastic theory can be an effective tool to determine the interaction energy between dislocation and Frank loop. However, MD allows investigating the effect of plasticity on the Frank loop structure.

4.3.1. Simulation cell

The MD technique used in this study is similar to that of the dislocation single gliding simulations in chapter 3. A constant strain rate is applied to the simulation box using the method of Osetsky *et al.* [52]. The reactions occur over a time scale of a few tens of ps and for strain rate levels of 10^7 s^{-1}, which means a dislocation velocity of ~55 m.s^{-1}.

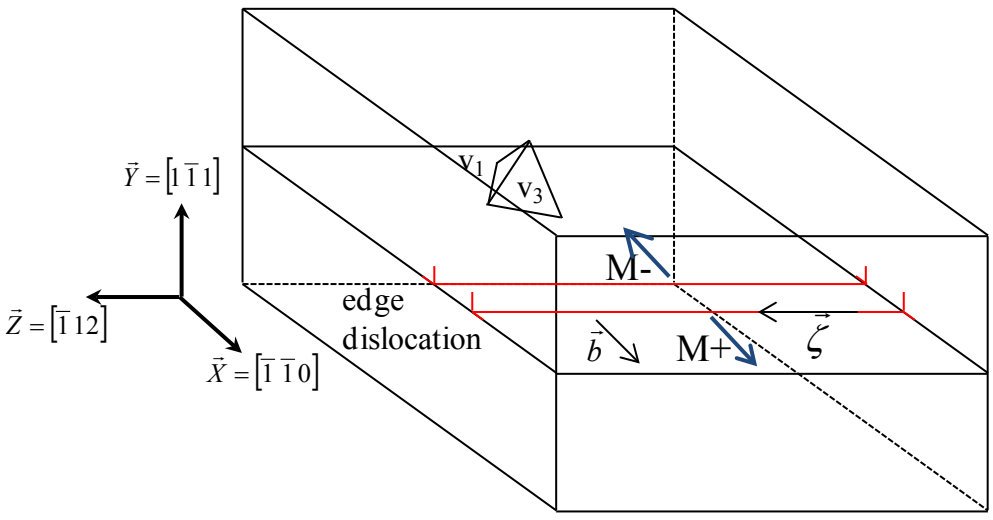

Figure 4.14: Schematic representation of the simulation cell.

The simulation cell is sketched in Figure 4.14 including a Thompson tetrahedron to denote Frank loop orientation gathered in Figure 4.15. The FCC crystal is oriented along $\vec{X} = [\bar{1}\,\bar{1}\,0]$, $\vec{Y} = [1\,\bar{1}\,1]$ and

$\vec{Z} = [\bar{1}\,12]$. The perfect edge dislocation is introduced in the cell with a Burgers vector $a/2[\bar{1}\,\bar{1}\,0]$ parallel to the $\vec{X}$ axis and a dislocation line $\vec{\zeta}$ parallel to the $\vec{Z}$ axis. The edge dislocation glides along the $\vec{X}$ axis in a positive (*M+*) or negative (*M-*) direction of gliding. PBC are applied in the $\vec{X}$ and $\vec{Z}$ directions whereas fixed boundary conditions are applied on three $\vec{Y}$ upper and lower $(1\,\bar{1}\,1)$ atomic layers. The thickness of the grips is slightly higher than the cut-off radius of the ternary interatomic potential. The cell size in the $\vec{X}$ direction makes sure that the dissociation distance (~10 nm) becomes independent of this dimension box size. The time step is 10^{-15} s for all the simulations. The energy of the system is firstly minimized with a quench algorithm during 50 time steps. The quenched configuration is then relaxed for 2×10^{-2} ns in the NVT ensemble for thermalization (with a Nose-Hoover Thermostat). The temperature attributed to the system is 300, 600 or 900 K. After this procedure, the shearing of the simulation box starts by displacing the upper and lower grips. Depending on the thermal expansion, the crystal is scaled up with the appropriate lattice parameter for minimizing the internal pressure.

The Frank loop is introduced at the beginning of the simulations following the building of the edge dislocation in the simulated cell with a central position in the glide plane. The extra disc is introduced in the SFE position. The Frank loop considered here has initially a circular shape and is an interstitial type. Once the system is relaxed, the Frank loop adopts the hexagonal shape with edges in the $\langle 110 \rangle$ directions for a diameter of 2 nm except for the higher diameter (10 nm) where the circular shape is conserved. Due to PBC, the interloop distance in the $\vec{Z}$ direction corresponds to the box size. It has been set to 20 nm for the Frank loop size of 2 nm. The glide distance fixed at 45 nm and the height of the cell at 32 nm. For a Frank loop diameter of 10 nm, the box size in the $\vec{Z}$ direction (interloop distance) is fixed at 40 nm with a height of 43 nm to avoid inherent surface effect.

For the 2 nm and 10 nm size, the simulation cell contains respectively about 2.6 M mobile atoms and ~7 M mobile atoms. The simulations are conducted with a MD code developed in the Central Research Institute of Electric Power Industry (CRIEPI). The simulations have been run on supercomputer "Ivanoe" with 576 and 729 processors. The usual time to achieve one simulation is 4 days. After that and if the Frank loop has not been absorbed, the simulation is pursued thanks to the restart files. Thus, for a reason of computer time consuming, each interaction is carried out for 3 random alloying generators.

Table 4.2: Comparison between interloop distance used here and experimental measurements on austenitic stainless steels 304 and 316.

Diameter (nm)	Mean interloop distance (nm)	Density (m^{-3})
10	57	31×10^{21} [42]
4.7	69	45×10^{21} [42]
11.2	23	1.7×10^{23} [47]
4.6	49	0.9×10^{23} [47]

The loop is set beyond the critical distance from the nearest partial dislocation, called the capture distance of the dislocation. The loop is separated by a distance of 15 nm from the center of the dislocation core and relaxes during the minimization energy to form the expected loop without any direct contacts with the nearest Shockley partial. Below a critical distance, called capture distance

[22], the loop is unstable and glides towards the edge dislocation. This phenomenon is supposed to increase with temperature and the loop size. But in this study, this kind of absorption is not observed, even for a higher loop diameter nor at 900 K. Thus, we supposed the capture distance should be situated around 3 nm and should not vary so much with the temperature and loop size.

4.3.2. Configurations

All possible configurations between edge dislocation and Frank loop are investigated. Figure 4.15 details the orientation of Frank Loop based on the Thompson tetrahedron notation seen from the side of Y coordinates. This is the same Tetrahedron used in Figure 4.14. The edge dislocation has a CD Burgers vector and lying in the $(1\,\bar{1}\,1)$ habit plane. The Frank loop is extended in a $\{1\,1\,1\}$ plane and can adopt one of the four planes proposed by the tetrahedron (noted V_1 through V_4 here), including the habit plane of the edge dislocation. The dislocation can approach Frank loop from two sides depending on the shearing conditions with a *M+* or *M-* motion direction. The habit plane between the edge dislocation and the Frank loop is equivalent in the case of the V_4 orientation with a Burgers vector of $1/3[\bar{1}\,1\,\bar{1}]$.

A configuration is thus characterized by 2 main variables: the motion direction (*M-* or *M+*) and the orientation of Frank loop (V_1, V_2, V_3 and V_4). The combination generates 8 interactions as detailed in Table 4.3. Moreover, as the simulations are carried out in a random alloying environment, three different seed numbers are chosen for the random number generators and applied to each combination of the 2 main variables. This gives a total of 24 configurations for each temperature.

Table 4.3: Resulting Burgers vector of the 8 non-equivalent interactions between Shockley partial and Frank Loop.

Shockley partial		$\vec{b}_1$ $1/6[\bar{2}\,\bar{1}\,1]$ (*M+*)	$\vec{b}_2$ $1/6[\bar{1}\,\bar{2}\,\bar{1}]$ (*M-*)
Frank loop	V_1 $1/3[1\,1\,1]$	$1/6[0\,1\,3]$	$1/6[1\,0\,1]$
	V_2 $1/3[1\,\bar{1}\,\bar{1}]$	$1/6[0\,\bar{3}\,\bar{1}]$	$1/6[1\,\bar{4}\,\bar{3}]$
	V_3 $1/3[\bar{1}\,\bar{1}\,1]$	$1/6[\bar{4}\,\bar{3}\,3]$	$1/6[\bar{3}\,\bar{4}\,1]$
	V_4 $1/3[\bar{1}\,1\,\bar{1}]$	$1/2[\bar{4}\,1\,\bar{1}]$	$1/6[\bar{3}\,0\,\bar{3}]$

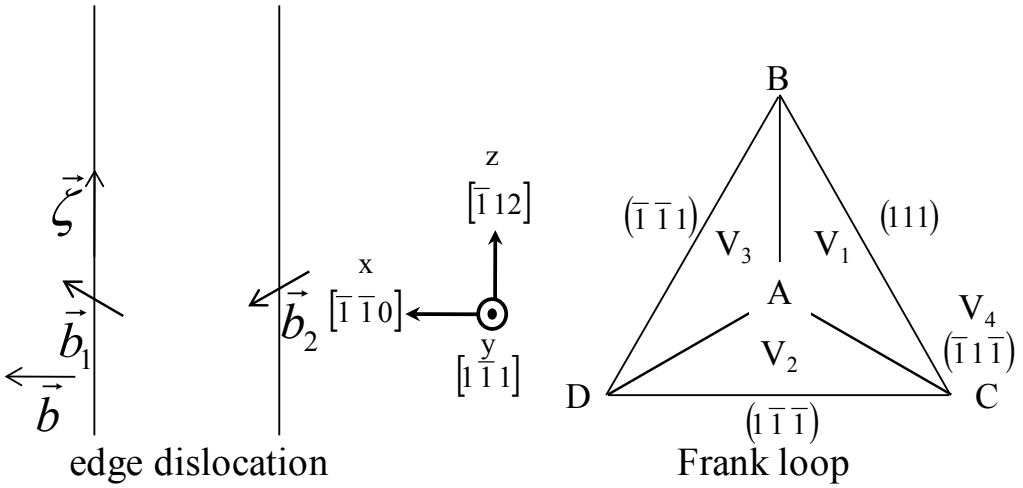

Figure 4.15: Configurations used here to denote the orientations and configurations of the Frank loop and the edge dislocation.

4.3.3. Interaction with a 2 nm Frank loop

Depending on the initial configurations between the edge dislocation and the Frank loop, three main resulting configurations are observed which is in accordance with the previous studies in FCC. The different reactions are presented depending on the new configuration adopted by the Frank loop. First a structural analysis is developed based on the new shape of the dislocation and the character of the loop. Secondly, a critical stress, necessary to unpin the dislocation from the Frank loop, is reported.

The MD simulations are performed at three temperatures (300 K, 600 K and 900 K). The configurations adopted by Frank loop after the interaction with the edge dislocation core can be classified into three main categories:

1. Shearing: the dislocation shears the Frank loops creating a step at its surface. This reaction mechanism is detailed in Figure 4.16;

2. Unfaulting: the Frank fault is removed due to the interaction with the dislocation and the loop becomes a perfect loop. Different types of unfaulting have been identified. The Frank loop can be unfaulted: with the formation of a bridge segment (see Figure 4.17), after the unpinning (see Figure 4.18), into a new habit plane (see Figure 4.19), and after being dragged along short distance (see Figure 4.20);

3. Absorption: a part or the whole Frank loop is integrated to the dislocation core. Different types of absorption have been identified. The Frank loop can be absorbed on a Shockley partial (see Figure 4.21), with the formation of a "Superjog" (see Figure 4.22), and with the formation of a double "Superjogs" (see Figure 4.23).

Table 4.4 gathers the reaction outcome depending on the temperature, the orientation of the Frank loop and the alloying random generator for a positive shearing *M+* of the crystal. We can see that unfaulting is the main interaction mechanism. Absorption can be sub-categorized into two configurations where the Frank loop can be completely or partially absorbed, on one or two partials, or completely as a double superjog [33] by the dislocation core. The absorption mechanism is the second main resulting configuration obtained after the first passage of the edge dislocation on the Frank loop. Only four cases of shearing are observed. This observation is in contradiction with the result obtained by Terentyev *et al.* [7], where a decrease of SFE enhanced formation of shearing to the expense of unfaulting for high SFE material. Those three mechanisms have also been identified by Nogaret *et al.* [6] with a pure copper potential with associated SFE similar to the one of austenitic stainless steel. The absorption can be done into a glissile superjog [53] on straight edge dislocation. The unfaulting mechanism is mainly controlled by a cross-slip process. Contrary to previous studies, unfaulting mechanism occurs only after being into contact with the loop, maybe because a low SFE reduced the probability to initiate partial segments inside Frank loop. Two Shockley partial dislocation segments are supposed to be initiated and propagate at the loop surface. The propagation of those partials removes the fault to turn the Frank loop into a perfect loop of Burgers vector $\vec{b} = 1/2\langle 110 \rangle$.

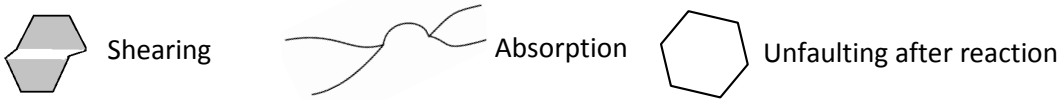

Movement *M+*	Temperature	Orientation of Frank loop	V_1	V_2	V_3	V_4
	300 K	Seed #1				
		Seed #2				
		Seed #3				
	600 K	Seed #1				
		Seed #2				
		Seed #3				
	900 K	Seed #1				
		Seed #2				
		Seed #3				

Table 4.4: Resulting configurations between edge dislocation and Frank loop (*D*=2 nm) for the first passage with a *M+* dislocation motion. The above legend indicates the notation used in the table. The reaction is conducted at 300 K, 600 K and 900 K for three alloying random configurations. The loops have a $\langle 110 \rangle$ side and are hexagonal.

Table 4.5 gathers the new configurations of the Frank loop after the first interaction with the two partials in a negative shearing *M-* of the crystal. At 300 K, Contrary to the positive motion *M+*, the predominant reaction between the Frank loop and the edge dislocation is the shearing mechanism except for V_1 orientation where unfaulting is the predominant mechanism. This observation is in accordance with the result obtained by Terentyev *et al.* [7] where absorption of the loop is a process thermally activated with an alternative unfaullting mechanism at 600 K. For both shearing directions (*M+* and *M-*), the random number generator for solute distribution seems to affect strongly the reaction mechanism. There are for example two cases where the three mechanisms are observed for one orientation and one temperature. This can point out that considering the size of the loop (2 nm), the mechanism of interaction is very localized and depends strongly on the alloying content around the Frank loop. However, the composition effect has not been deeply investigated in this study as it is difficult to define a radius of measurement around the interstitial defect and set which atoms have an influence on the interaction mechanism.

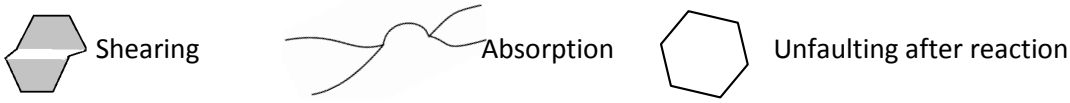

Movement *M*-	Temperature	Orientation of Frank loop	V_1	V_2	V_3	V_4
	300 K	Seed #1				
		Seed #2				
		Seed #3				
	600 K	Seed #1				
		Seed #2				
		Seed #3				
	900 K	Seed #1				
		Seed #2				
		Seed #3				

Table 4.5: Resulting configuration between edge dislocation and Frank loop (*D*=2 nm) for the first passage with an *M*- dislocation motion. The above legend indicates the notation used in the table. The reaction is conducted at 300 K, 600 K and 900 K for three alloying random configurations. The loops have a $\langle 110 \rangle$ side and are hexagonal.

4.3.4. Detailed mechanisms of interactions: shearing, unfaulting and absorption

Shearing (Figure 4.16)

Shearing produces steps that can emerge on one side of the loop or within the faulted loop depending on its orientation towards the edge dislocation. However, the life-time of this step is usually lower than 5 ps, the time window used here. For the first passage of the edge dislocation in the case of an *M+* dislocation motion, shearing is observed for V_1 at 300 K, V_3 at 600 K and V_4 orientation at 300 K and 600 K. Figure 4.16 represents the shearing reaction between V_1 Frank loop and edge dislocation at 300 K. The maximum stress associated to this interaction is evaluated at 273 MPa corresponds to the snapshot (b). The pinning event is made on leading dislocation contrary to the three other cases where the trailing partial bows out. During the second and the third passage of the dislocation due to the PBC, the shearing is observed only on two cases which have already been sheared and thus is maintained for dislocations that have been previously sheared at low temperatures. In all cases the step created after the passage of the two partials is recombined and the Frank loop recovers its planar surface almost immediately. At the beginning of the interaction

and for V_1 and V_3 orientations, the leading partial is repelled by the defect and first contacts are made between the small segment of the leading partial and the $\langle 110 \rangle$ edges of the Frank loop. In the case of an *M+* motion, for all the shearing cases, no permanent damage is observed and the Frank loop keeps its interstitial type at 300 K. However, the position of the Frank loop is slightly translated of 1-2 *b* after the passage of the two partials.

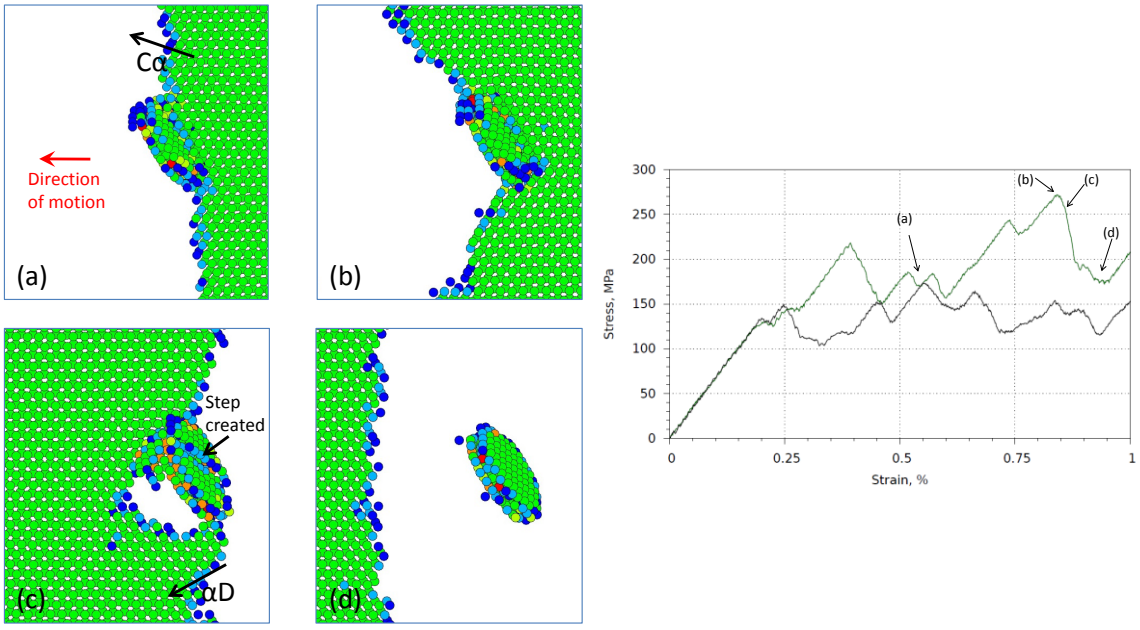

Figure 4.16: Configuration V_1/*M+* at 300 K: snapshots are shown at 182 MPa, 650 ps (a), 273 MPa (Critical stress), 850 ps (b), 238 MPa, 875 ps (c) and 192 MPa, 910 ps (d). The associated Stress-Strain curve is plotted on the right with the single edge dislocation response.

When a negative strain is applied, the shearing mechanism is quite similar to the opposite motion of shearing *M+*. A step is generated on the side of the loop in the case of V_1, V_2 and V_3 orientation and on the loop surface for V_4. The only main difference with the opposite motion is that the dislocation is consistently attracted by the loop surface once the separation distance between the two defects is around 3-4 *b*. The dislocation pursues its gliding in its habit plane with a planar shape and left behind the faulted Frank loop with its previous orientation.

Unfaulting with the formation of a bridge segment (Figure 4.17)

Depending on the orientation of the loop, the unfaulting mechanism can happen with a bridge created between the leading partial and the Frank loop. The removal of the faulted surface is made with the propagation of this segment all around the loop. On the other hand, when there is no such segment between the two defects, the successive passage of the leading and trailing partial on the Frank Loop conducts to a perfect loop of Burgers vector $\vec{b} = 1/2\langle 110 \rangle$. Specific cases where the Frank loop and the dislocation lied in the same habit plane conduct to change the habit plane of the former Frank loop.

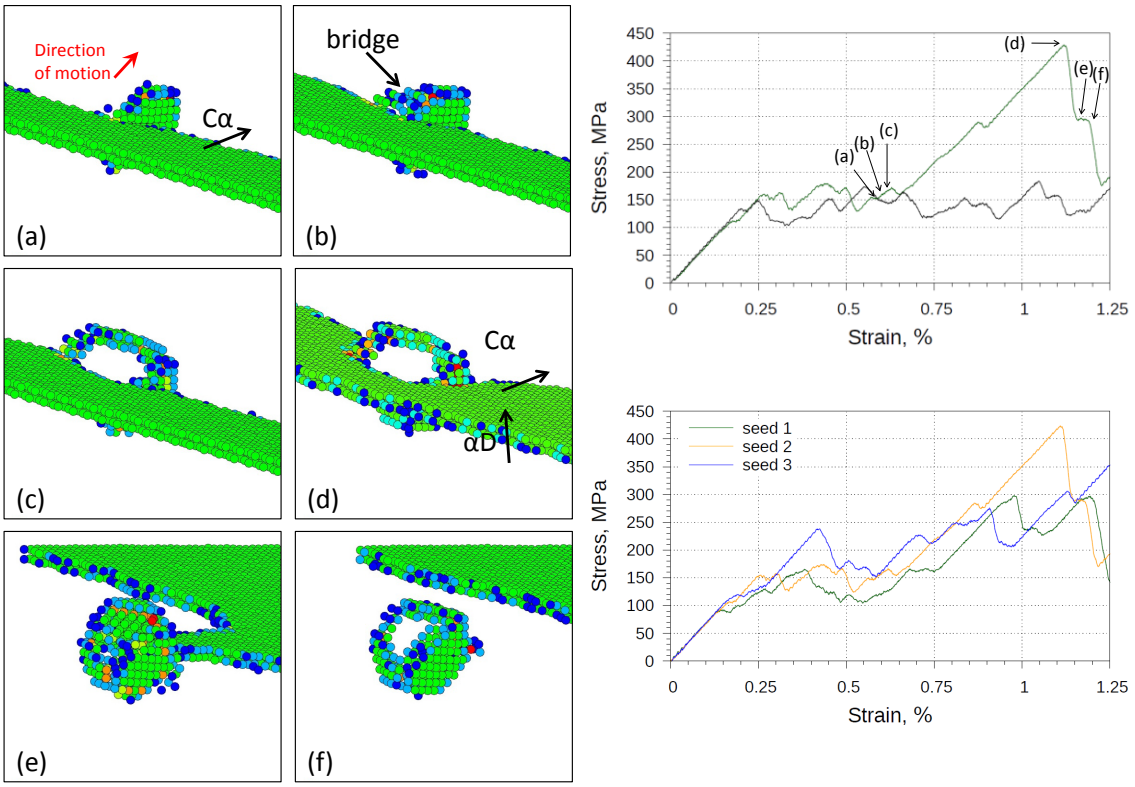

Figure 4.17: Configuration *V_2/M+* at 300 K: snapshots are shown at 160 MPa, 605 ps (a), 166 MPa, 620 ps (b), 169 MPa, 625 ps (c), 430 MPa (Critical stress), 1.12 ns (d), 291 MPa, 1.19 ns (e) and 281 MPa, 1.20 ns (f). The associated Stress-Strain curve is plotted on the right with the single edge dislocation response. A comparison with to other seed is plotted above, for an equivalent orientation of Frank loop and a similar mechanism (unfaulting).

This reaction is represented in Figure 4.17. The leading partial approaches the loop with the applied stress. The first contact is established with the nearest side of the Frank loop. A bridge is created between the left arm of the leading partial and the top $\langle 110 \rangle$ edge of the loop. This junction is apparently constituted of multiple cross slipped segments. With the increasing stress, this bridge sweeps the upper loop when simultaneously the edge dislocation starts to bend. The remaining loop interacts with the trailing partial. The maximum stress due to pinning is associated to the configuration represented in Figure 4.17 (d) when a constriction around the two nodes is formed. In Figure 4.17 (d), we can see that the lower part of the Frank loop has already its perfect behavior whereas the upper part has been turned into what appears to be a SFT. This temporary configuration is consistent with the MD simulations realized by Kadoyoshi *et al.* [19] who established under stresses the formation of an incomplete SFT from a scalene hexagonal loop. This configuration induces a strong pinning on the trailing partial when the retaining forces appear with the bowing. The dislocation core is released from the new perfect loop with $\vec{b} = 1/2\langle 110 \rangle$ and conserves a planar shape and its initial habit plane.

Unfaulting after the unpinning (Figure 4.18)

The loop is first repelled by the Frank loop and does not enter into contact with the loop surface before a constriction is formed. The leading partial adopts a screw behavior on the right and left arm with the increasing stress and forms a dipole that closes behind the loop. The Frank loop has still its interstitial type and interacts with the trailing partial in the same way as it is described above. The upper part of the Frank loop is transformed into a SFT whereas the lower part is unfaulted. This configuration induces a strong pinning on the trailing partial which strongly bows out. At the end of

the interaction, the trailing partial is unpinned from the obstacle and a perfect loop of $\vec{b} = 1/2\langle 110 \rangle$ is left behind.

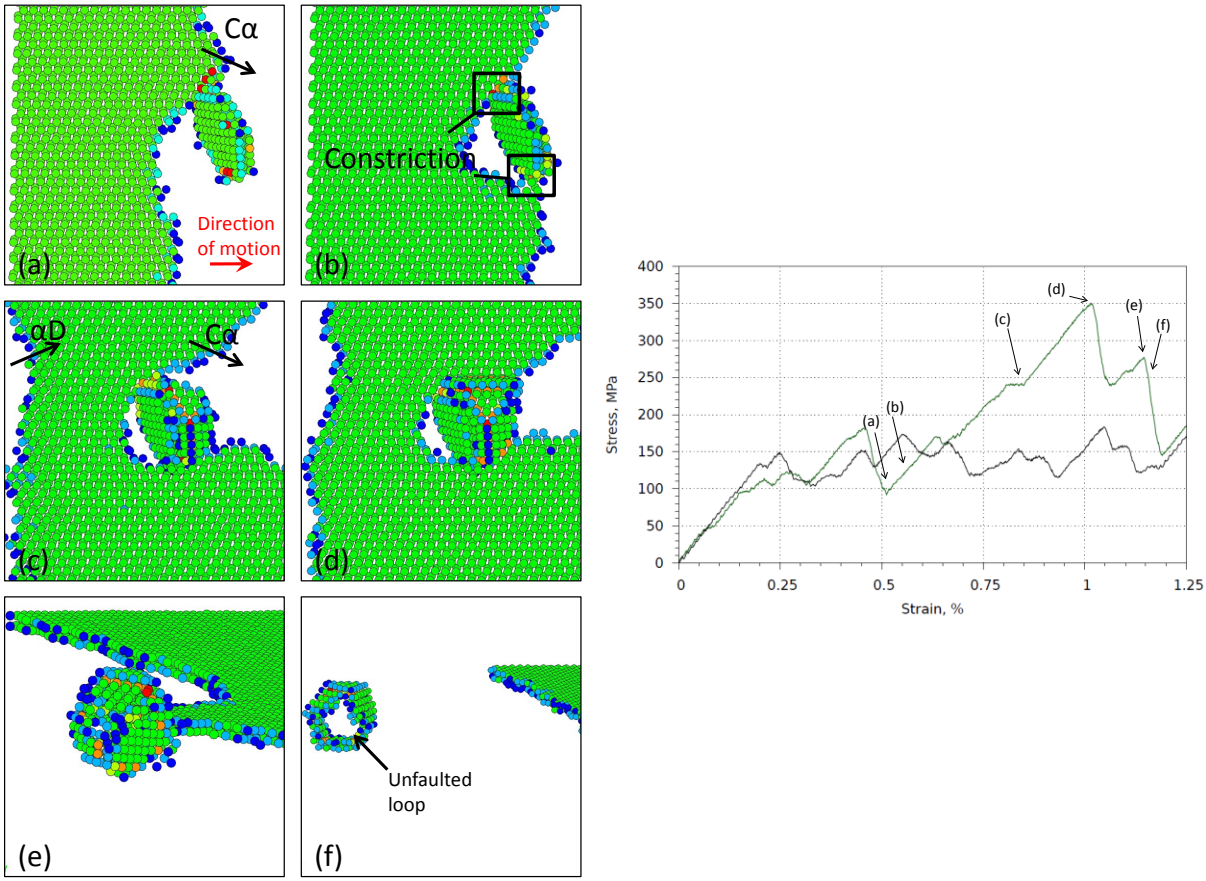

Figure 4.18: Configuration *V_3/M+* at 300 K: snapshots are shown at 120 MPa, 545 ps (a), 132 MPa, 660 ps (b), 251 MPa, 860 ns (c), 363 MPa (Critical stress), 1.03 ns (d) 287 MPa, 1.16 ns with a different viewing angle (e) and 280 MPa, 1.17 ns (f). The associated Stress-Strain curve is plotted on the right with the single edge dislocation response.

Unfaulting into a new habit plane (Figure 4.19)

Contrary to the two previous orientations, the leading partial is attracted by the Frank loop in the two nearest edges of the loop. The trailing partial slightly bows out under the stress applied and is unpinned from the loop. The dislocation core crossed the defect without any configuration changes and both stay planar. The maximum stress is reached once the trailing partial starts to interact with the Frank loop, which is firstly unfaulted and removed into a new habit plane. The center of the defect is also switched to an upper position. The perfect loop remains stable in this configuration up to the point of the next interaction during the second passage.

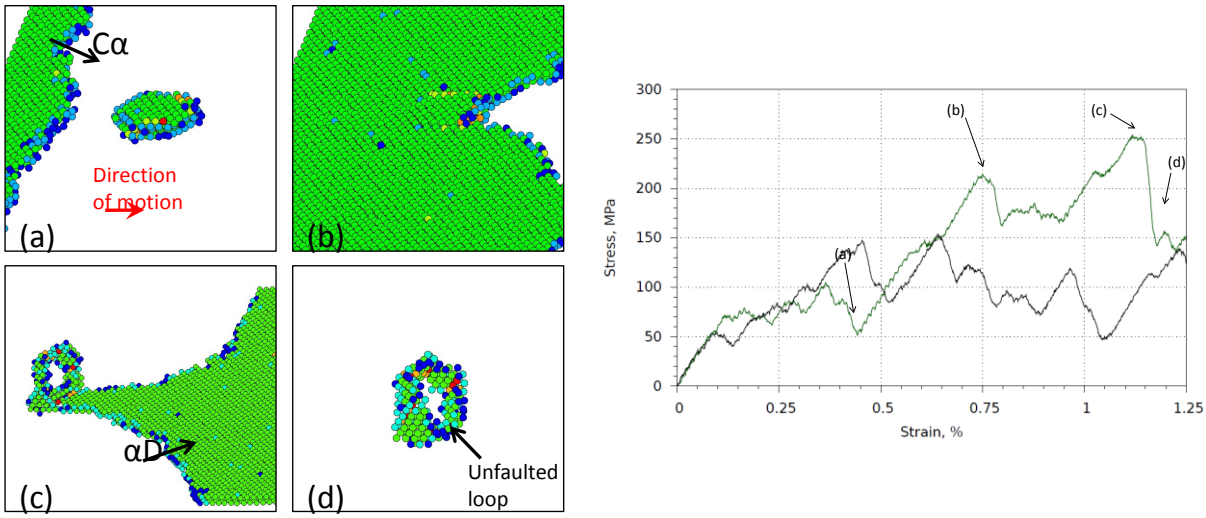

Figure 4.19: Configuration *V_4/M+* at 600 K: snapshots are shown at 83 MPa, 430 ps (a), 210 MPa, 780 ps (b), 257 MPa (Critical Stress), 1.15 ns (c), 176 MPa, 1.18 ns (d). The associated Stress-Strain curve is plotted on the right with the single edge dislocation response.

Unfaulting and drag along short distance (Figure 4. 20)

In this configuration, the loop is unfaulted with the creation and propagation of a "bridge" segment between the left arm of the leading partial and the top segment of the Frank loop. Once the Frank loop is unfaulted, the configuration adopted by the Frank loop can be assimilated to a helix along the leading partial. In this case, this new combination can be summarized as follows:

$$\alpha D \rightarrow \alpha B + DB \tag{4.3}$$

As the stress increases, it propagates along the three top segments of the loop to generate a perfect loop which is glissile [54] (see Figure 4.20 (b)). Corresponding to its new Burgers vector, the perfect loop glides in the direction pointed out by the new Burgers vector direction $\vec{b} = \frac{1}{2}\langle 110 \rangle$. The perfect loop is attached to the leading partial and is dragged during the gliding of the dislocation along the leading partial for a distance of ~40 *b*. the constriction [55] occurs and conducts to a distance of ~5-10 *b* between the leading and the trailing partial. The configuration adopted by the Frank loop is similar to the one observed in Figure 4.17 (e). With the increasing stress, the trailing partial is released from the perfect loop and left behind the unfaulted glissile loop with the same orientation equivalent to the one adopted during the dragging.

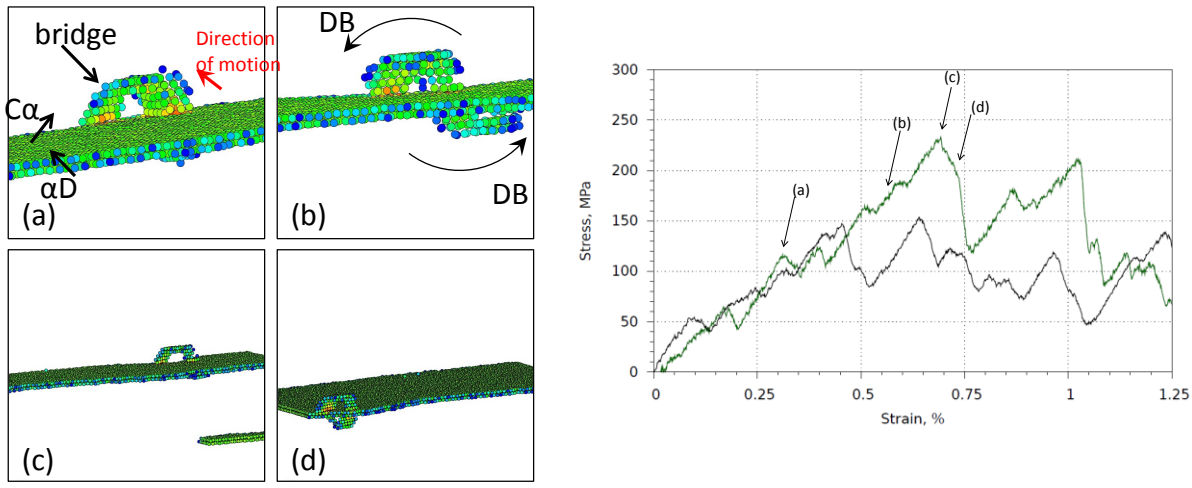

Figure 4.20: Configuration *V_2/M+* at 600 K: snapshots are shown at 100 MPa, 345 ps (a), 109 MPa, 545 ps (b), 232 MPa (Critical Stress), 880 ps (c), 167 MPa, 900 ps (d). The associated Stress-Strain curve is plotted on the right with the single edge dislocation response.

Absorption on a Shockley partial (Figure 4.21)

Absorption is the third mechanism observed in the interaction between edge dislocation and Frank loop. This interaction is always preceded by the unfaulting of the Frank loop with a "bridge" segment which is created between the right or left arm of the leading partial dislocation depending on the motion direction and/or the new configuration adopted by the loop into a helix. Multiple types of absorption have been identified, maybe due to the chemical composition around the loop and the orientation of the Frank loop towards the edge dislocation. In this case, a perfect loop is dragged as it has been first identified by Rodney *et al.* [33]. Depending on the orientation of the new $\frac{1}{2}\langle 110 \rangle$ perfect loop, it can move in the gliding direction or along the Shockley partial. The partial absorption can also be done with the formation of a "superjog". The Frank loop can also be completely absorbed by the dislocation core into a "superjog" or "double superjog". The three main interaction types will be detailed here depending on the absorption types on the edge dislocation.

The interaction process is illustrated in Figure 4.21 in the case of a *M+* motion. In this configuration, the leading partial is attracted to the surface of the Frank loop. The Frank loop is then separated into two distinct upper and lower parts. The upper part has flipped in a $\frac{1}{2}\langle 110 \rangle$ direction equivalent to the one of the edge dislocation and has glided in the same direction. This flipping can be summarized with the Thompson notation as:

$$\alpha D + CD \rightarrow C\alpha \tag{4.4}$$

With the increasing stress, the edge dislocation acquires a screw character near the junctions and generates a screw dipole. Then, the lower part is crossed by the two Shockley partials with a double cross slip mechanism. Once the trailing partial has reached the lower part, the second unfaulting occurs. The edge dislocation is pinned for 110 ps and then is released after a strong bowing out of the trailing partial arms. Thus, the initial Frank loop has been turned into perfect loops of BD and CD Burgers vector respectively after reaction with the αD and Cα Shockley partials. The perfect loop CD continues to glide in the equivalent direction as the edge dislocation and remained attached to the loop until the next interaction.

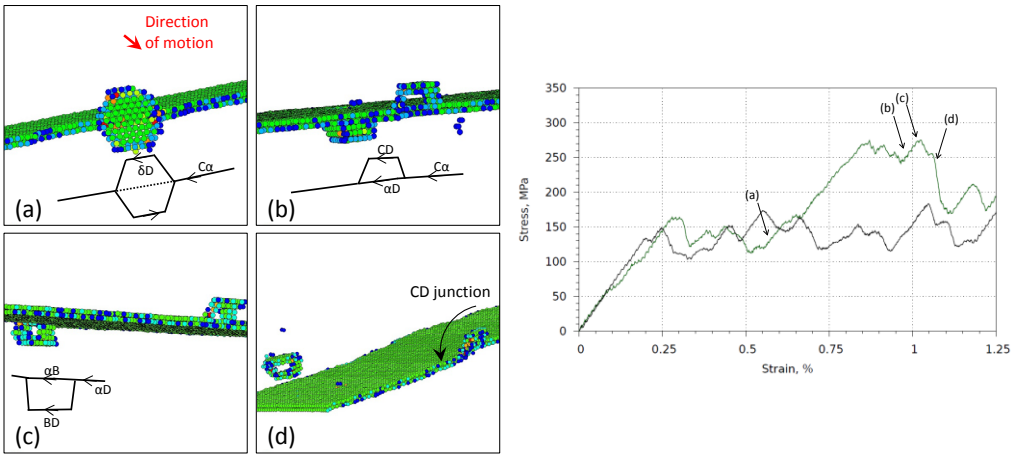

Figure 4.21: Configuration V_1/M+ at 300 K: snapshots are shown at 136 MPa, 555 ps(a), 284 MPa, 920 ps (b), 290 MPa (Critical stress), 1.04 ns (c), 253 MPa, 1.08 ns (d). The associated Stress-Strain curve is plotted on the right with the single edge dislocation response.

Absorption into a "Superjog" (Figure 4.22)

In this configuration, the upper part of the loop is absorbed with the creation of two junctions between the two partials and edges of the loop. The superjogs generated in this study are typically of acute type [53]. The orientation of the Frank loop (V_1) promotes the attraction of the leading partial by the defect surface. Then the Frank loop is divided into two parts where the lower part is orientated in the BD direction and the upper part in the CD direction. Those two loops are connected by the leading partial following reaction in the Thompson notation:

$$C\alpha \rightarrow \alpha D + CD \rightarrow \alpha B + CD + BD \tag{4.5}$$

After the interaction, the "superjog" remains dragged in its original configuration. One of the superjog is dissociated in its ADC glide plane while the other is constricted in the AB segment. The segment between the "superjogs" has climbed by 6 $(1\,\bar{1}\,1)$ planes and is extended in its new BCD glide plane. The dissociation of the extended "superjog" produces one βα/CD Lomer-Cottrell stair-rod segments, visible on the right part of Figure 4.22 (d).

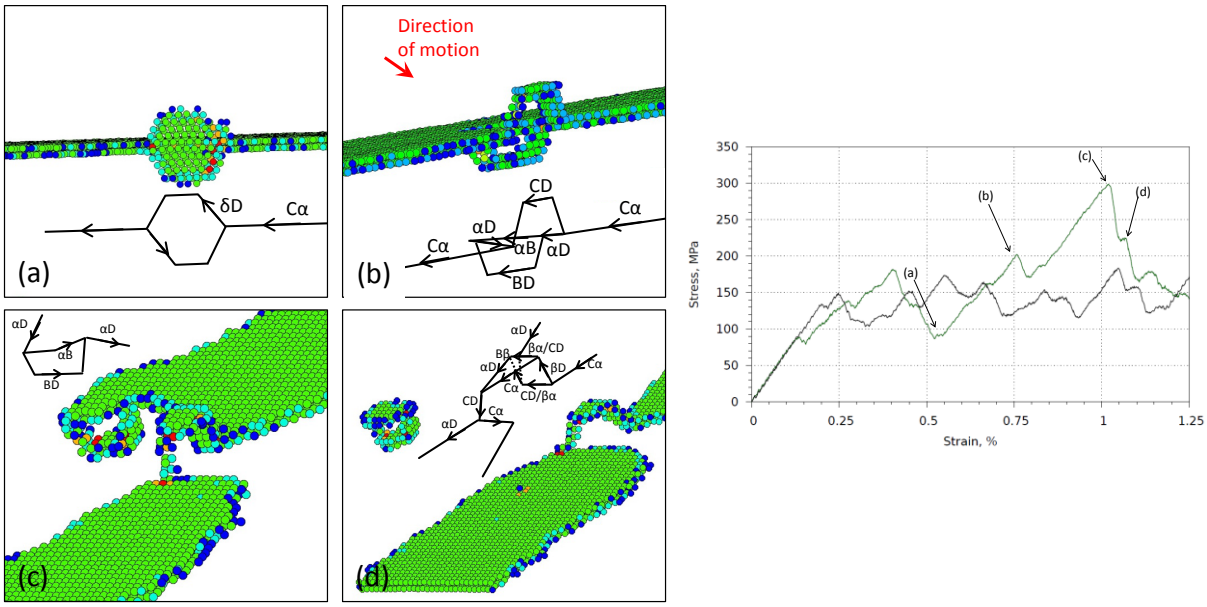

Figure 4.22: Configuration V_1/M+ at 300 K: snapshots are shown at 113 MPa, 520 ps (a) 217 MPa, 770 ps (b), 309 MPa (Critical stress), 1.02 ns (c) 239 MPa, 1.07 ns (d). The associated Stress-Strain curve is plotted on the right with its single edge dislocation response.

Absorption into a double "superjogs" (Figure 4.23)

The interaction process lasts 360 ps and is difficult to identify at the atomic level due to high temperature at 900 K. However, the final configuration can be interpreted in term of "superjogs" notation in the following way. The configuration of the initial faulted loop repels the leading partial dislocation and forces the interaction with the left and right $\langle 110 \rangle$ sides. After a strong pinning of 280 ps on the leading partial dislocation, the loop becomes unfaulted and climbs by 5 $\{111\}$ planes. The dumbbells rotate in the CD direction (Figure 4.23 (b)) and create a junction:

$$C\alpha \rightarrow \alpha D + CD \tag{4.6}$$

A constriction then occurs with the increasing stress. The relaxed and stable configuration obtained is represented on Figure 4.23(c). The shape of the cluster has changed during the interaction and has been transformed into a double "superjog" on the dislocation. One "superjog" appears to be extended while the other one is constricted and then dissociated to form a Lomer segment with the edge dislocation. The two jogs are extended in the ADC glide plane. The dissociation of the extended superjog in its ADC plane produces two βα Lomer-Cottrell stair-rod dislocations, visible on the left and right side. The structure of the left "superjogs" is rather more complicated. The upper part is constricted along the AB segment and then cross slip to be redissociated in the ADC plane with the creation of a Lomer segment.The particularity of the reaction is the complete removing of the defect without any debris left behind. However, the total absorption of the defect can also be done only on the leading or trailing partial. It appears that absorption is the mechanism which is thermally activated and becomes predominant at 900 K, specifically for the *M*- motion where the probability of complete absorption is higher.

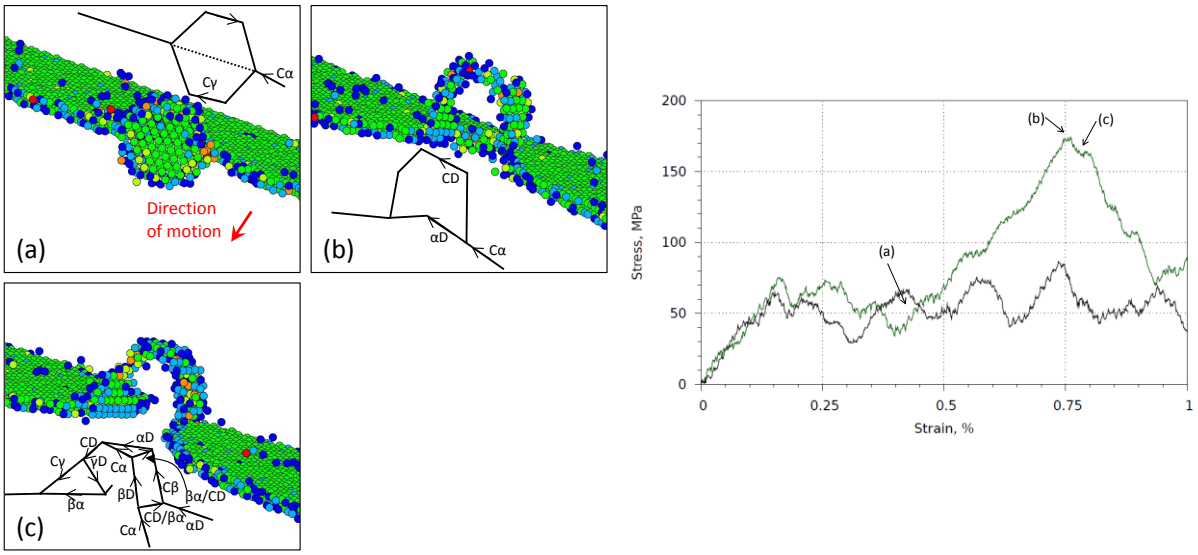

Figure 4.23: Configuration V_3/M+ at 900 K: snapshots are shown at 43,6 MPa, 445 ps (a), 175 MPa (Critical stress), 770 ps (b), 162 MPa, 780 ps (c). The associated Stress-Strain curve is plotted on the right with its single edge dislocation response.

4.3.5. Analysis of the 2nd and 3thd dislocation passage

The simulations have been continued for a second and third passage, if the Frank loop has not been previously absorbed. In fact, as the probability that a double "superjog" or a glissile loop may interact with a faulted or unfaulted loop is very low, the simulations are stopped once the defect has been partially or completely absorbed. A first analysis reveals that unfaulting and absorption are thermally activated to become predominant at 900 K. Thus, for 3 successive interactions, all the configurations, that is the alloying random generator combined with the orientation of the loop, conducted to absorb the Frank loop to the new perfect loop. These observations are in accordance with the previous analysis made by Nogaret *et al.* [6], which notices the removing of the defects. This coincides with the observation of clear band in irradiated material. In this study, the absorption is observed for 80% of the total configurations. In the absorption process, it appears that the unfaulting is necessary for a next and likely absorption. However, 10% of the initial Frank loop conserved their faulted character and 50% of the faulted loops are still present at 300 K. The other new configurations exhibit unfaulted loops with a new Burgers vector $\frac{1}{2}\langle 110 \rangle$, which suggests an absorption if the interactions were pursued.

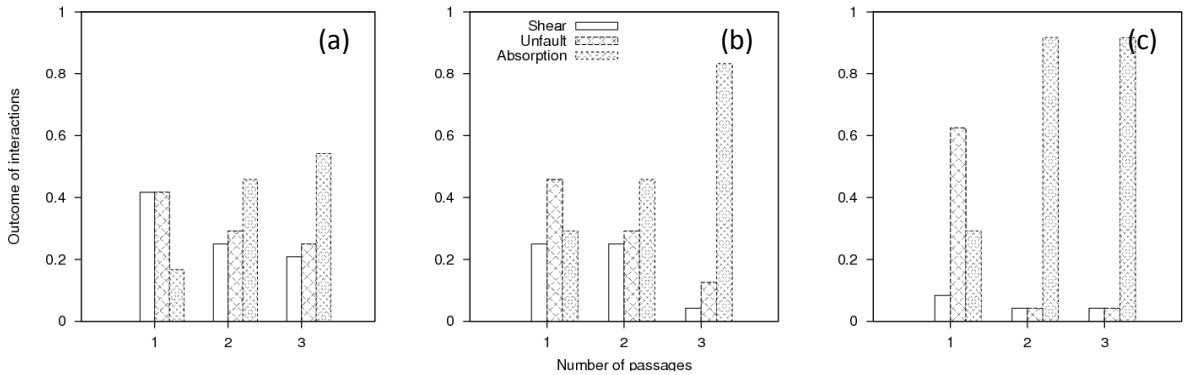

Figure 4.24: Cumulative ratio of interaction configurations (unfaulting, absorption or shear) at 300 K (a), 600 K (b) and 900 K (c) depending on the number of passages.

The effect of alloying is also very strong on the reaction mechanism even if sometimes it appears there is a preferential orientation for a specific reaction. In this way, it can mean that the SFE and/or friction stress is an important parameter to justify the new configuration adopted by the Frank loop. The effect of local alloying content has not been investigated here but recent studies led by Terentyev *et al.* [7] highlight the effect of Ni in a Fe FCC host matrix. It appears that SFE and friction stress reduce the probability of absorption in the case of edge and screw dislocations. In that case, a possibility of absorption in temperature is the decreasing of friction stress which allows the dislocation to cross-slip with the two arms of the leading edge dislocation that have acquired a screw character. Thus, the unfaulting mechanism becomes similar to the one that occurs in pure metals [32, 51]. With the aim of investigating the effect of the Frank loop size, the equivalent interactions have been conducted in the case of an *M+* motion for a diameter of 10 nm.

4.3.6. Interaction with a 10 nm Frank loop

In the case of a 10 nm Frank loop size, shearing is the majority resulting configuration for each orientation and random distribution. New dimensions of the simulation box have been adopted mainly to avoid inherent surface effect. However, if shearing is the main mechanism of interaction observed, different types of shearing have been observed.

Shearing with cross-slip (see Figure 4.25)

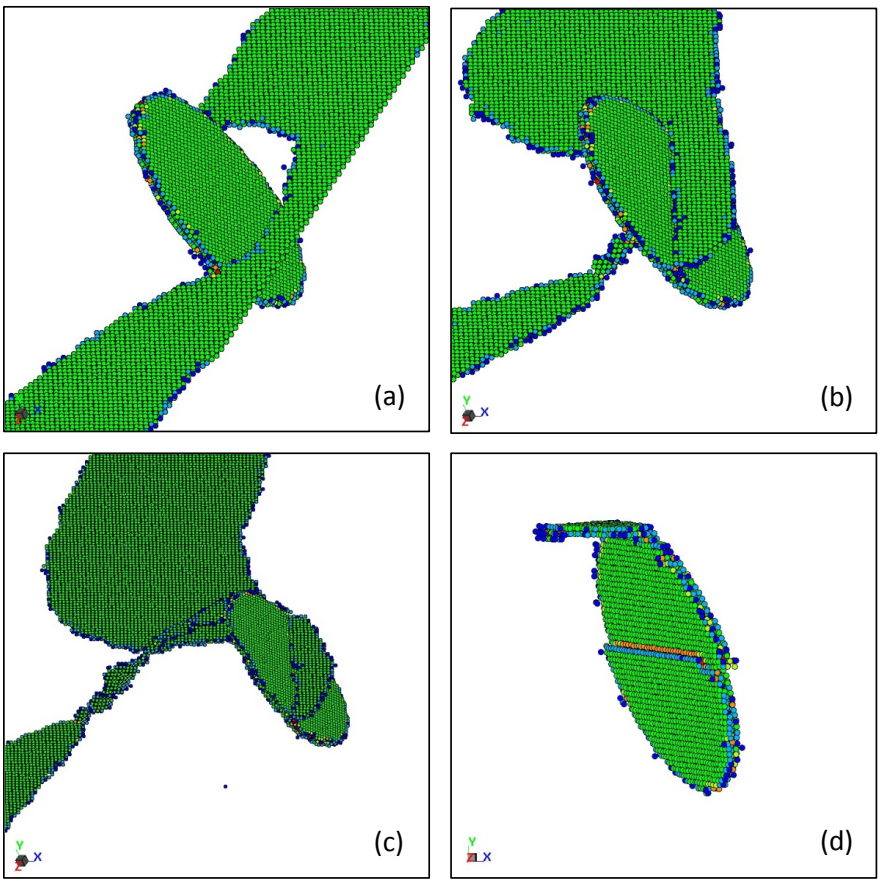

Figure 4.25: Configuration V_3/M+ at 300 K: snapshots are shown at 204 MPa, 0.93 ns (a), 330 MPa (Critical stress), 1.37 ns (b), 228 MPa, 1.43 ns (c) and 199 MPa, 1.57 ns (with a different view angle) (d).

As it can be seen in Figure 4.25, the edge dislocation comes into contact with the Frank loop on the sides of the Frank loop in the glide plane of the dislocation. As it is represented in snapshot (a), the edge dislocation is repelled by the Frank loop and begins to interact with the extrinsic fault when the stress increases. On the other hand, due to the increasing stress, the edge dislocation arms acquire a screw character and cross-slip, as it can be observed on snapshots (b). As the left arm of the edge dislocation continues to cross-slip along the sides of Frank loop, the right arm is still pinned on the dislocation glide plane. Once the edge dislocation is unpinned from the obstacle, the helix disappears and joins to the other arm. The two partials have consequently sheared the loop sequentially, leaving a $1/2\langle 110\rangle$ step on its surface (d). Contrary to shearing observed on smaller Frank loop, this straight step remains stable until the next interaction.

Simple shearing (see Figure 4.26)

The leading partial reaches the loop surface. With the increasing stress, the trailing partial comes into contact with the Frank loop. The dislocation is enlarged in this right part. The edge dislocation leaves the Frank loop with a $1/2[110]$ step generated on the dislocation glide plane. It has to be noted that no recombination of the step happened before the next interaction.

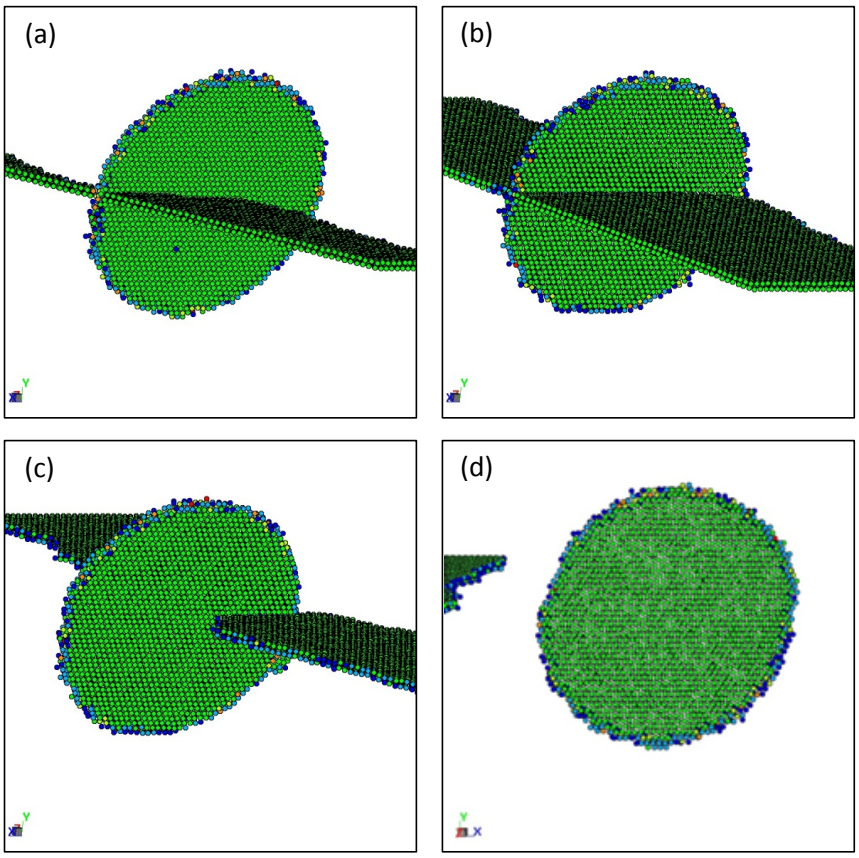

Figure 4.26: Configuration V_2/M+ at 300 K: snapshots are shown at 155 MPa, 0.68 ns (a), 219 MPa, 0.73 ns (b), 225 MPa (Critical stress), 1.03 ns (c) and 161 MPa, 1.1 ns (d).

Single Shearing with Frank loop climbing (see Figure 4.27)

Applied strain forces leading partial to approach the Frank loop. With increasing stress, trailing partial approaches the loop and forms the constriction. After that, the leading partial dislocation arms start to bow out and conjoin behind the loop. As a result, the constriction is formed. Then, with the increasing stress, the trailing partial bows-out emerging a dipole which closes leaving behind a sheared faulted loop. As the trailing partial tries to overcome the last side of Frank loop, the obstacle climbs down by $1/3[111]$.

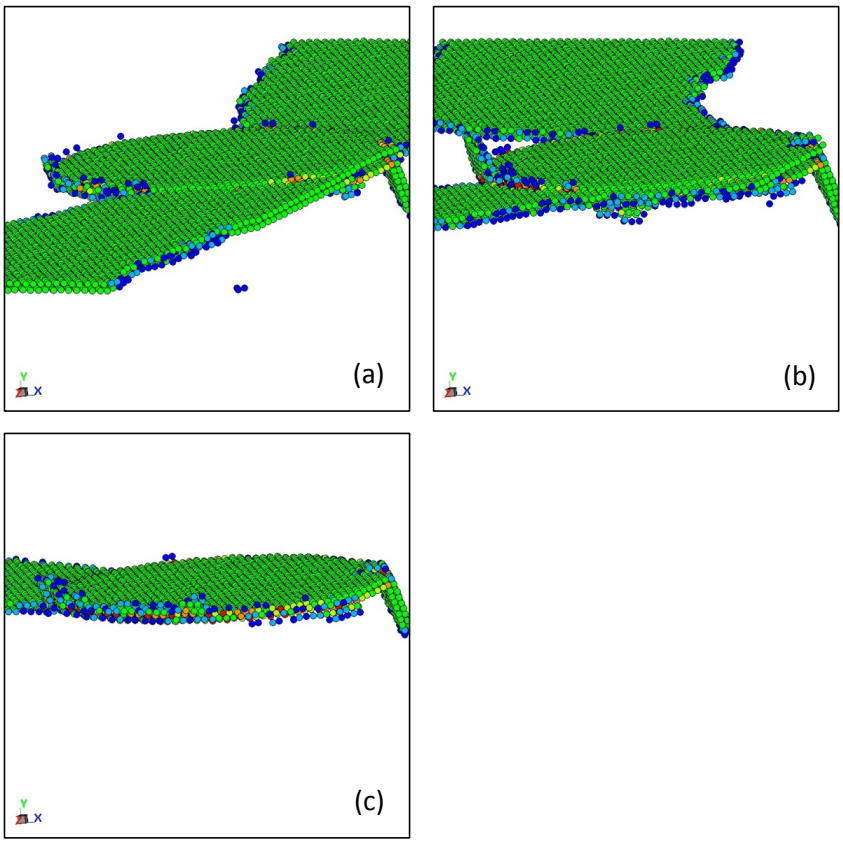

Figure 4.27: Configuration V_4/M+ at 300 K: snapshots are shown at 281 MPa, 1 ns (a), 347 MPa (Critical stress), 1.25 ns (b), 298 MPa, 1.45 ns (c).

4.3.7. Critical unpinning stress analysis: comparison between 2 and 10 nm size

The effective force of a point obstacle provides the formula $F = 2\Gamma\cos(\varphi)$. However, the line tension in the vicinity of the obstacle is difficult to define because of the complex and strong interaction between the dislocation segments surrounding the obstacle. Secondly, the angle φ is hard to determine as the curvature of the dislocation segments varies strongly in the vicinity of the obstacle. Nevertheless, this classical treatment can be used only if the line tension of the dislocation is well known. Although uncommon, this situation is associated to the Orowan mechanism, meaning the obstacle resistance is infinite irrespective of the size of the obstacle. Once the shear stress τ is applied, a segment of length l bows out into an arc of radius $r=\mu b/\tau$. The maximum shear stress τ_{max} can be introduced in the Orowan stress formula $\Delta\tau l/\mu b$ as the strength of the obstacle

$$\alpha = \frac{(\tau_{\max} - \tau_c)l}{\mu b_0} \tag{4.7}$$

with μ the shear modulus, $b_0 \approx 0.71 a_0$ and $l=L_x-D_L$, where L_x is the dimension of the box of the *x axis* and D_L is the Frank loop Diameter. τ_c is the friction stress evaluated without the presence of Frank loop for the equivalent strain rate. The shear modulus is defined here as the average of both the Reuss (μ=60 GPa) and the Voigt (μ=88 GPa) average. Thus, in this section, μ=74 GPa.

The influence of temperature, loop morphology and random generator has been investigated on the unpinning stress for dislocation to overcome Frank loops strength. The strength α of the obstacle has been subdivided into three classes depending on the temperature, four classes depending on the orientation of the Frank loop and three other classes based on the alloying random generator. The

strength of the 2 nm Frank loop, represented in Figure 4.28 and 4.29 and in Figure 4.30 in the case of the 10 nm Frank loop. The influence of temperature on α is not similar for the different orientations and sizes of Frank loops. However, in the case of the 10 nm size, where shearing is the only mechanism that is observed, the strength of the obstacle tends to decrease systematically with the temperature. Thus, the interaction mechanism types influence strongly the strength of the obstacle, *i.e.* can provide an increase of α whereas the temperature also increases. Depending on the Frank loop size, the 10 nm Frank loop gives a higher hardening by a factor of ~33 %.

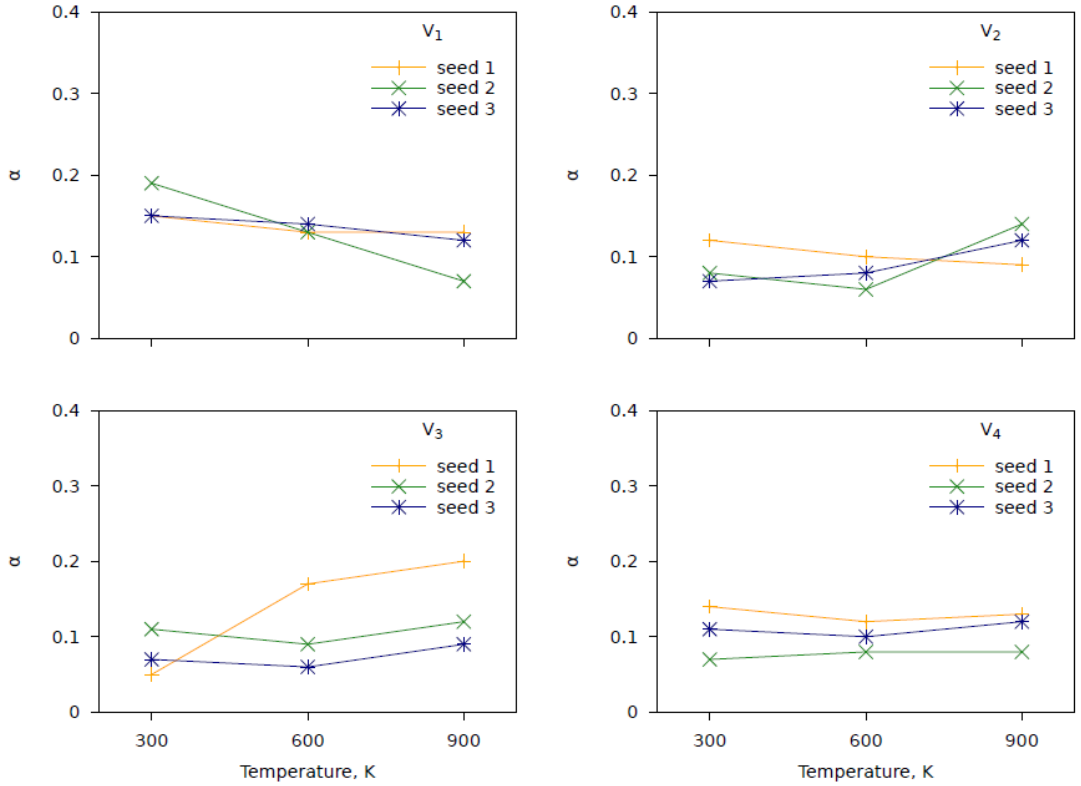

Figure 4.28: Strength of the Frank loop depending on temperature for the four possible orientations and three alloying random generators for a shear modulus of 74 GPa and a diameter of 2 nm in the case of the *M*- motion.

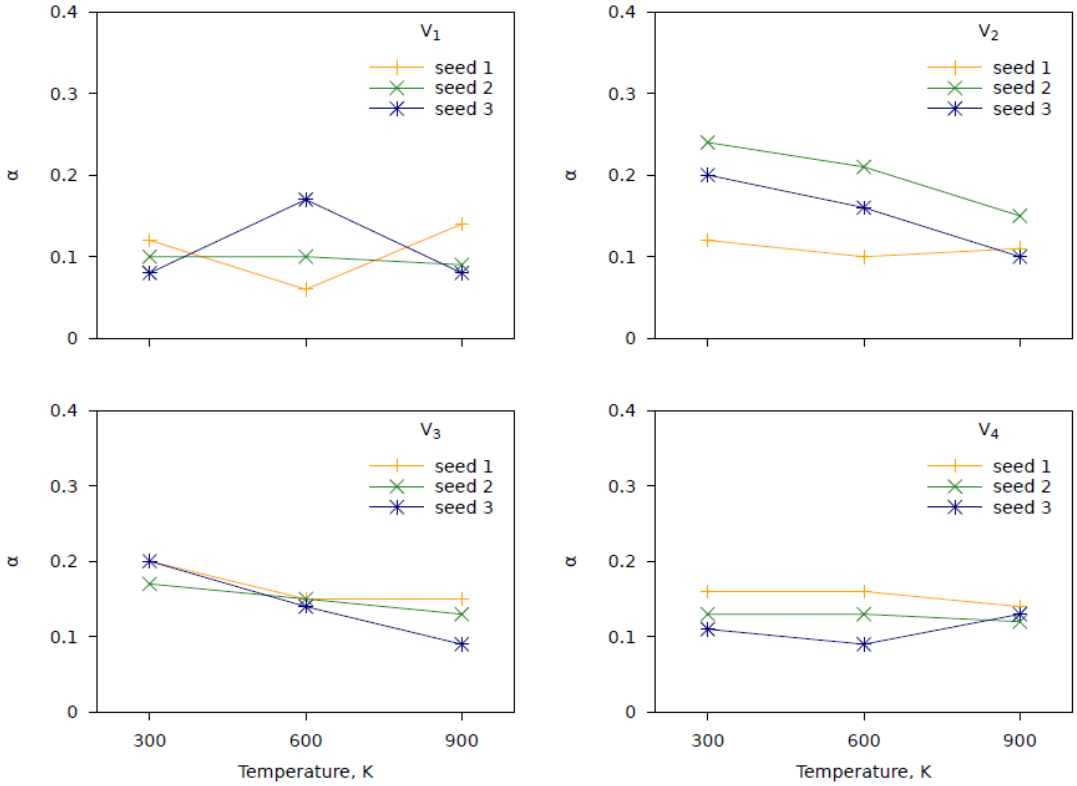

Figure 4.29: Strength of the Frank loop depending on temperature for the four possible orientations and three alloying random generators for a shear modulus of 74 GPa and a diameter of 2 nm in the case of the *M+* motion.

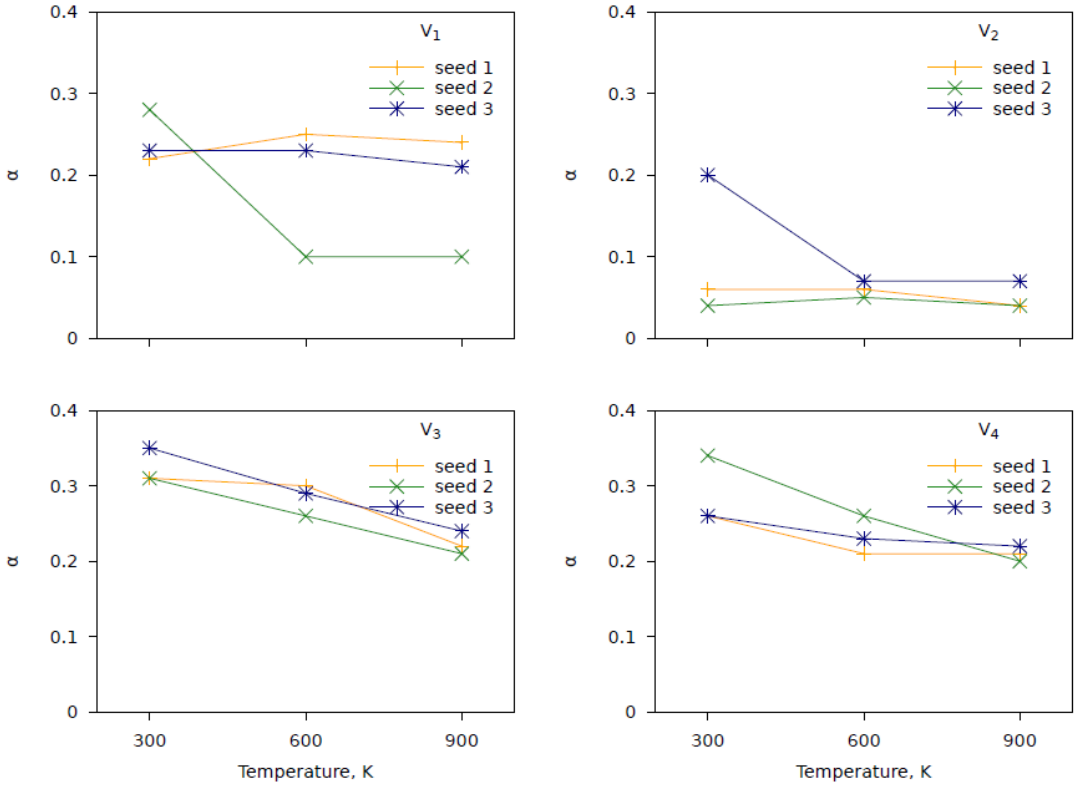

Figure 4.30: Strength of the Frank loop depending on temperature for the four possible orientations and three alloying random generators for a shear modulus of 74 GPa and a diameter of 10 nm in the case of the *M+* motion.

4.4. Constitutive law

In all cases, the reactions observed for the interactions between dislocation and Frank loop are similar as those found in [6, 33 and 51]. The absorption mechanism is a thermally activated process, which becomes the majority of the interactions observed after the third interaction. The Unfaulting mechanism appears to be a prerequisite for the absorption of the Frank loop. For the shearing mechanism, the reconstruction of the sheared Frank loop, which occurs via the migration of the 1/2[110] step formed in the shear reaction over the loop, is systematic for the 2 nm size and never observed for the 10 nm size. This observation is in accordance with the simulation realized by Rodney and presented in the PhD thesis of Pokor [56]. In the case of the 2 nm size of Frank loops, the combination of the probability of the outcome reactions and the average strength $\overline{\alpha}$ of the obstacle can constitute a constitutive law which can be employed at a higher simulation scale, for example in Dislocation Dynamics. The average strength of the obstacle and the outcome of the interaction are gathered in Figure 4.31 for the three main sets of interactions.

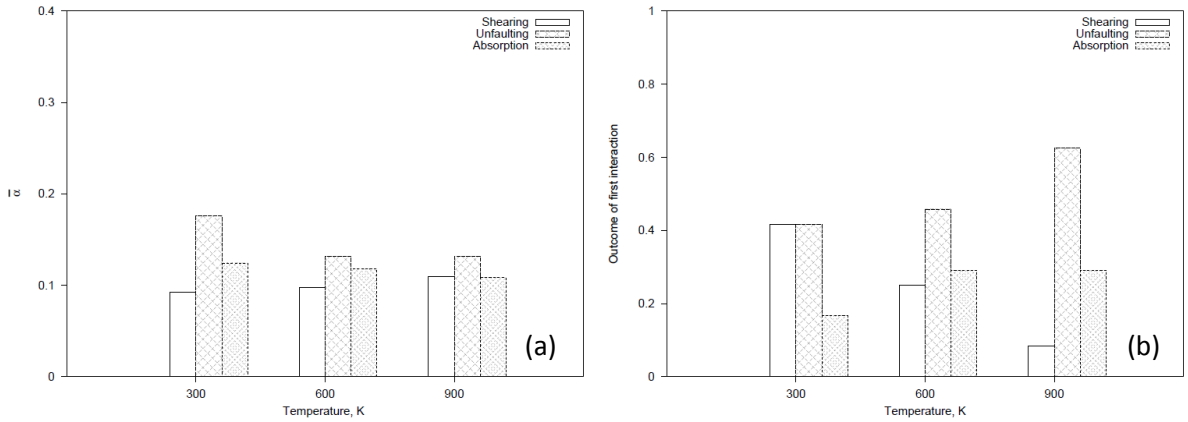

Figure 4.31: Comparison between (a) the average strength $\overline{\alpha}$ of the obstacle and (b) the associated probability of the reaction outcomes at 300 K, 600 K and 900 K in the case of the 2 nm Frank loop and the first interaction.

4.5. Conclusion

The interaction between edge dislocation with Frank loops in a random solid solution Fe-Ni_{10}-Cr_{20} has been studied. The interaction has been carried out using a constant strain rate loading conditions corresponding to a dislocation velocity of ~55 m.s^{-1}. For the 2 nm size, the interaction mechanism between the edge dislocation and the Frank loop can be categorized into three sets: the shearing, unfaulting and the absorption. The majority of Frank loop are absorbed in the third passage, where unfaulting of the Frank loop appears to be a prerequisite. The absorption of nearly all the obstacles is in agreement with the experimental observations where the presences of clear bands or free obstacle channels are revealed. The unfaulting of Frank loop always happened with a direct contact between the Frank loop and edge dislocation and the faulted Frank loop is turned into a perfect loop of $b = 1/2 < 110 >$. For a 10 nm size of Frank loop, only shearing is identified by letting behind a stable step on the Frank loop.

From a mechanical point of view, the 10 nm size appears exhibit a higher strength than the 2 nm size by a factor of 33 %. In the case of the 2 nm size, the unfaulting mechanism is the most strengthening mechanism compare to the shearing which exhibits the lesser strength α of the obstacle. The temperature affects strongly the resistance of the obstacle. However, for the 2 nm size, the decreasing of α is not systematic. This can be partly explained by the unfaulting mechanism, which is a thermally activated process, and is associated to a higher strength. The combination of data on the average strength of the obstacle and the probability of the outcome reaction can constitute a constitutive law useful for the Dislocation Dynamics.

References

- Chapter IV -

[1] F. A. Garner, **Radiation Damage in Austenitic Steels**, Elsevier (2012) Amsterdam.
[2] G. S. Was, **Fundamentals of Radiation Materials Science Metals and Alloys**, Springer (2007).
[3] S. J. Zinkle, P. J. Maziasz, R. E. Stoller, **Dose dependence of the microstructural evolution in neutron-irradiated austenitic stainless steel**, J. Nucl. Mater., 206 (1993) 266-286.
[4] S.M. Bruemmer, E. P. Simonen, P. M. Scott, P. L. Andresen, G. S. Was, J. L. Nelson, **Radiation-induced material changes and susceptibility to intergranular failure of light-water-reactor core internals**, J. Nucl. Mater., 274 (1999) 299-314.
[5] X. Q. Li, A. Almazouzi, **Deformation and microstructure of neutron irradiated stainless steels with different stacking fault energy**, J. Nucl. Mater., 385 (2009) 329-333.
[6] T. Nogaret, C. Robertson, D. Rodney, **Atomistic-scale plasticity in the presence of Frank loops**, Phil. Mag., 87 (2007) 945-966.
[7] D. Terentyev, A. Bakaev, Y. N. Osetsky, **Interaction of dislocations with Frank loops in Fe-Ni alloys and pure Ni: An MD study**, J. Nucl. Mater., 442 (2013) 208-217.
[8] J. A. Brinkman, **On the nature of radiation damage in metals**, J. App. Phys., 25 (1954) 961-970.
[9] D. J. Bacon, F. Gao, Y. N. Osetsky, **The primary damage state in fcc, bcc and hcp metals as seen in molecular dynamics simulations**, J. Nucl. Mater., 276 (2000) 1-12.
[10] A. Seeger, **The nature of radiation damage in metals**, International atomic energy agency symposium on radiation damage in solids and reactor Materials, Venice, Italy (1962).
[11] R. S. Averback, **Atomic displacement processes in irradiated metals**, J. Nucl. Mater., 216 (1994) 49-62.
[12] C. S. Becquart, C. Domain, A. Legris, J. C. Van Duysen, **Influence of the interatomic potentials on molecular dynamics simulations of displacement cascades**, J. Nucl. Mater., 280 (2000) 73-85.
[13] A. V. Barashev, D. J. Bacon, S. I. Golubov, **Monte Carlo modeling of damage accumulation in metals under cascade irradiation**, J. Nucl. Mater., 276 (2000) 243-250.
[14] L. Boulanger, F. Soisson, Y. Serruys, **Interaction between the deformation and the irradiation defect clusters in austenitic steels**, J. Nucl. Mater., 233-237 (1996) 1004-1008.
[15] J. L. Strudel, J. Washburn, **Direct observations of interactions between imperfect loops and moving dislocations in aluminium**, Phil. Mag., 9 (1964) 491-506.
[16] G. Saada, **On the Stability of quenched dislocation loops in aluminium**, Acta Met., 10 (1962) 985-986.
[17] G. Saada, **Sur les boucles de dislocations formées par trempe**, Acta Metallurgica, 10 (1962) 551-553.
[18] Hull, D. J. Bacon, **Introduction to dislocations**, 4th. Ed. Oxford: Butterworth-Heinemann; 2001.
[19] T. Kadoyoshi, H. Kaburaki, F. Shimizu, H. Kimizuka, S. Jitsukawa, J. Li, **Molecular dynamics study on the formation of stacking fault tetrahedral and unfaulting of Frank loops in fcc metals**, Acta Mater., 55 (2007) 3073-3080.
[20] D. Kuhlmann-Wilsdorf, **On the origin of dislocations**, Phil. Mag., 26 (1958) 125-139.
[21] D. Rodney, G. Martin, **Dislocation pinning by small interstitial loops: a molecular dynamics study**, Phys. Rev. Lett., 82 (1999) 3272-3275.
[22] D. Rodney, G. Martin, Y. Bréchet, **Irradiation hardening by interstitial loops: atomistic study and micromechanical model**, Mater. Sci. Eng., A309-310 (2001) 198-202.
[23] Y. N. Osetsky, D. J. Bacon, V. Molhes, **Atomic modelling of strengthening mechanisms due to voids and copper precipitates in α-iron**, Philos. Mag., 83 (2003) 3623-3641.
[24] Y. N. Osetsky, D. J. Bacon, **Void and precipitate strengthening in α-iron: what can we learn from atomic-level modelling?**, J. Nucl. Mater., 323 (2003) 268-280.
[25] D. J. Bacon, Y. N. Osetsky, **The atomic-scale modeling of dislocation-obstacle interactions in irradiated metals**, Journal of Metals, 59 (2007) 40-45.

[26] D. J. Bacon, Y. N. Osetsky, **Dislocation-Obstacle interactions at atomic level in irradiated metals**, J. Math. Mech. Sol., 14 (2009) 270-283.
[27] G. J. Ackland, G. I. Tichy, V. Vitek, M. W. Finnis, **Simple N-body potentials for the noble-metals and nickel**, Philos. Mag., A 56 (1987) 735-756.
[28] D. J. Bacon, Y. N. Osetsky, **Modelling dislocation-obstacle interactions in metals exposed to an irradiation environment**, Mater. Sci. Eng., A 400 (2005) 353-361.
[29] D. J. Bacon, Y. N. Osetsky, D. Rodney, **Dislocation-Obstacle Interactions at the Atomic Level**, Chapter 88 (2009).
[30] D. Terentyev, A. Bakaev, **Interaction of a screw dislocation with Frank loops in Fe-10Ni-20Cr alloy**, J. Nucl. Mater., 442 (2013) 208-217.
[31] [X] B.N. Singh, S. J. Zinkle, **Defect accumulation in pure fcc metals in the transient regime: a review**, Journal of Nuclear Materials, 206 (1993) 212-229.
[32] D. Terentyev, P. Grammatikopoulos, D. J. Bacon, Yu. N. Osetsky, **Simulation of the interaction between an edge dislocation and a $\langle 100 \rangle$ interstitial dislocation loop in α-iron**, Acta Mater., 56 (2008) 5086-5046.
[33] D. Rodney, G. Martin, **Dislocation pinning by glissile interstitial loops in a nickel crystal: A molecular-dynamics study**, Phys. Rev., B61 (2000) 8714-8725.
[34] T. S. Byun, N. Hashimoto, K. Farrell, E. H. Lee, **Characteristics of microscopic strain localization in irradiated 316 stainless steels and pure vanadium**, J. Nucl. Mater., 349 (2006) 251-264.
[35] E. H. Lee, T. S. Byun, J. D. Hunn, M. H. Yoo, K. Farrell, L. K. Mansur, **On the origin of deformation microstructures in austenitic stainless steel: part I-Microstructures**, Acta Mater., 49 (2001) 3269-3276.
[36] H. Neuhauser, R. Rodloff, **Study of slip band development on neutron-irradiated copper single crystals by high speed cinematography**, Acta Met., 22 (1974) 375-384.
[37] T. S. Byun, N. Hashimoto, K. Farrell, **Deformation mode map of irradiated 316 stainless steel in true stress-dose space**, J Nucl. Mater., 351 (2006) 303-315.
[38] I.M. Robertson, A. Beaudoin, K. Al-Fadhalah, Li. Chun-Ming, J. Robach, B.D. Wirth, A. Arsenlis, D. Ahn, P. Sofronis, **Dislocation-obstacle interactions: Dynamics experiments to continuum modeling**, Mater. Sci. Eng., 400-401 (2005) 245-250.
[39] T. Nogaret, D. Rodney, M. Fivel, C. Robertson, **Clear band formation simulated by dislocation dynamics: Role of helical turns and pile ups**, J. Nucl. Mater., 380 (2008) 22-29.
[40] D.J. Edwards, B. N. Singh, J.B. Bilde-Sørensen, **Initiation and propagation of cleared channels in neutron-irradiated pure copper and a precipitation hardened CuCrZr alloy**, J. Nucl. Mater., 342 (2005) 164-178.
[41] M. Sauzay, K. Bavard, W. Karlsen, **TEM observations and finite element modeling of channel deformation in pre-irradiated austenitic stainless steels – Interactions with free surfaces and grain boundaries**, J. Nucl. Mater., 406 (2010) 152-165.
[42] C. Pokor, Y. Bréchet, P. Dubuisson, J.-P. Massoud, A. Barbu, **Irradiation damage in 304 and 316 stainless steels: experimental investigation and modeling. Part I: Evolution of the microstructure**, J. Nucl. Mater., 326 (2004) 19-29.
[43] P. J. Maziasz, **Overview of microstructural evolution in neutron-irradiated austenitic stainless steels**, J. Nucl. Mater., 205 (1993) 118-145.
[44] N. Yoshida, **Microstructure formation and its role on yield strength in AISI 316 SS irradiated by fission and fusion neutrons**, J. Nucl. Mater., 174 (1990) 220-228.
[45] A. Etienne, B. Radiguet, P. Pareige, J.-P. Massoud, C. Pokor, **Tomographic atom probe characterization of the microstructure of a cold worked 316 austenitic stainless steel after neutron irradiation**, J. Nucl. Mater., 382 (2008) 64-69.
[46] D. J. Edwards, E. P. Simonen, F. A. Garner, L. R. Greenwood, B. M. Oliver, S. M. Bruemmer, **Influence of irradiation temperature and dose gradients on the microstructural evolution in neutron-irradiated 316SS**, J. Nucl. Mater., 317 (2003) 32-45.

[47] D. J. Edwards, E. P. Simonen, S. M. Bruemmer, **Evolution of fine-scale defects in stainless steels neutron-irradiated at 275 °C**, J. Nucl. Mater., 317 (2003) 13-31.
[48] A. Volgin, **Characterization and understanding of ion irradiation effect on the microstructure of austenitic stainless steels,** PhD thesis (2012) University of Rouen.
[49] T. S. Byun, K. Farrell, E. H. Lee, J. D. Hunn, L. K. Mansur, **Strain hardening and plastic instability properties of austenitic stainless steels after proton and neutron irradiation**, J. Nucl. Mater., 298 (2001) 269-279.
[50] K. Farrell, T. S. Byun, **Tensile properties of candidate SNS target container materials after proton and neutron irradiation in the LANSCE accelerator**, J. Nucl. Mater., 296 (2001) 129-138.
[51] D. Rodney, **Molecular dynamics simulation of screw dislocations interacting with interstitial Frank loops in a model FCC crystal**, Acta Mater., 52 (2004) 607-614.
[52] Y. N. Osetsky, D. J. Bacon, **An atomic-level model for studying the dynamics of edge dislocations in metals**, Modelling Simul. Mater. Sci. Eng., 11 (2003) 427-446.
[53] J. P. Hirth, J. Lothe, **Theory of Dislocations**, Krieger, Malabar (1982).
[54] A. Luft, **Microstructural processes of plastic instabilities in strengthened metals**, Prog. Mater. Sci., 35 (1991) 97-204.
[55] A. N. Stroh, **Constrictions and Jogs in Extended Dislocations**, Proc. Phys. Soc., 67 (1954) 427-436.
[56] Cédric Pokor, **Caractérisation microstructurale et modélisation du durcissement des aciers austénitiques irradiés des structures internes des réacteurs à eau pressurisée**, PhD thesis (2002) Institut National Polytechnique de Grenoble.

5. General conclusion and future prospects

5.1 General conclusion

This study covers at the atomic scale the plasticity of a ternary Fe-Ni_{10}-Cr_{20} alloy, used to mimic 304 and/or 316 austenitic stainless steels, before and after the neutron irradiation through molecular dynamics simulations. The deformation mechanism is performed on a straight edge dislocation. The pre-irradiated material consists in a perfect solid solute solution of Ni and Cr randomly distributed in a Fe host matrix whereas the irradiated material is equivalent to the previous one with the presence of an interstitial Frank loop. These simulations are based on a ternary FeNiCr EAM potential developed in the SCK-CEN. This potential reproduces accurately the SFE and elastic constants C_{11}, C_{12} and C_{44} of the targeted composition. The SFE of this material, calculated with the dissociation distance measurements, is shown to decrease with temperature.

A theoretical analysis, based on the effect of the stress on the dissociation distance, has shown through a global expression that two stress components, τ_{xz} and τ_{yz}, affect the dislocation: τ_{xz} leads to the displacement of the dislocation whereas τ_{yz} influences the separation distance. A critical stress τ_{yz}, which depends only on the SFE, conducts to an infinite distance between the two partials, for the edge and screw character. The friction stress τ_f, neglected until now, is found to affect strongly the dissociation width.

The friction stress τ_f of the alloying material Fe-Ni_{10}-Cr_{20} has been determined by measuring the dissociation distance. A strong temperature dependence of τ_f is pointed out. Once a strain is applied and for a strain rate lower than 4 times 10^7 s^{-1}, the motion of the edge dislocation can be assimilated to a "stop and go" motion dominated by multiple pinning and unpinning events due to the different configurations adopted by the solute atoms in the dislocation glide plane. However, for a high velocity, the gliding of the dislocation appears to be continuous without any pinning events. The dislocation velocity which separates these two domains is set to 200 $m.s^{-1}$ at 300 K. The edge dislocation adopts an average velocity given by the Orowan's law. The critical stress τ_c has been found to be strongly affected by temperature in the same way as τ_f was. To predict the stress response of the edge dislocation, two constitutive laws have been applied. One is purely empirical and the second model takes explicitly the temperature into account and provides an activation volume of 12 b^3.

The interaction between the edge dislocation and the Frank loop is performed in the same random solid solute solution. The orientation, temperature, alloying random generator, shear direction and Frank loop size are investigated. For the 2 nm size, the resulting configurations have been found to depend strongly on the Ni and Cr configurations around the Frank loop. The Frank loop has been observed to be either sheared, unfaulted or absorbed, as observed in other studies. The absorption appears to be a thermally activated process where unfaulting is a prerequisite. The unfaulted loop adopts a $\frac{1}{2}\langle 110 \rangle$ Burgers vector and is shown to be metastable. The step created after shearing has a very low stability and is recombined after less than 5 ps. The absorption of the Frank loop on the dislocation can be done in the form of junctions, superjogs or double superjogs. After a series of interactions with the edge dislocation, most of the obstacles are removed. This result is in accordance with TEM observations of clear bands. The ratio of perfect loops and Frank loops

absorbed by the edge dislocation increases with temperature, which suggests that absorption is a thermally activated process. The unfaulting mechanism always involves a direct contact with the dislocation, *i.e.* due to the strain field of the dislocation, no partial nucleates inside the Frank loop surface to remove the faulted plane.

For the 10 nm diameter, the only mechanism observed is shearing. Contrary to the 2 nm size, the step created following the interactions with the dislocation is stable. The strength of Frank loops is more important for the 10 nm size. However, the strength of the 2 nm obstacle is not so weak in the alloy. In general, temperature leads to a reduction of the resistance of the obstacles except for the stress related to the unfaulting mechanism. The unfaulting mechanism requires the highest level of stress at 300 K and can be considered as the most efficient pinning mechanism. This can be explained by the strong bowing-out of the leading partial after the constriction with the Frank loop. This bowing-out conducts the leading partial segments to adopt a screw character. This new orientation induces a cross-slip and finally the unfaulting of the Frank loop. For the 10 nm size, the resistance of the obstacle is not affected by any parameters. In the case of the 2 nm, the linking of the probability of the outcome of the reactions, *i.e.* shearing, unfaulting or absorption, and the average stress associated to each reaction, conduct to a constitutive model providing fundamental data to proceed with the study at a higher simulation scale, for example with Dislocation Dynamics.

5.2 Future prospects

The major requirement for this study is to move on to the next simulation scale. DDD is the adequate simulation tool, mainly for investigating a consequential effect of a randomly distributed population of Frank loops of different sizes in the material. Also, the hypothesis that plastic deformation is accommodated by newly nucleated dislocations could be taken into account.

The effect of the local atomic configuration around the Frank loop affects strongly the interaction mechanism between the edge dislocation and the Frank loop, and thus the strength of the obstacle. Thus, the effect of alloying distribution around the Frank loops requests a deep investigation. This prospect is reinforced by the experimental investigations which show that Frank loops are decorated of Ni and depreciated in Cr for FeNiCr model alloy. At first sight, this effect is difficult to investigate due to the huge alloying content of the material. Moreover, it is also not obvious which part of the loop is the most hardening, *i.e.* the edge of the Frank loop or the faulted plan. The SFE and the friction stress are also two parameters that can have an effect on the interaction mechanism and thus on the resistance of the obstacle. The chemical composition can also be extended to Si. Another recent experimental study on a FeNiCrSi alloy has pointed out an enrichment in Si around Frank loops. Another point to consider is the extension to the lower and upper simulation scale. The enrichment in alloying elements of Frank loops should be conducted for example with the Kinetic Monte Carlo method for a lower simulation scale, and a correlative effect on the hardening, with a randomly distributed population of Frank loops, should be put forward with Dislocation Dynamics.

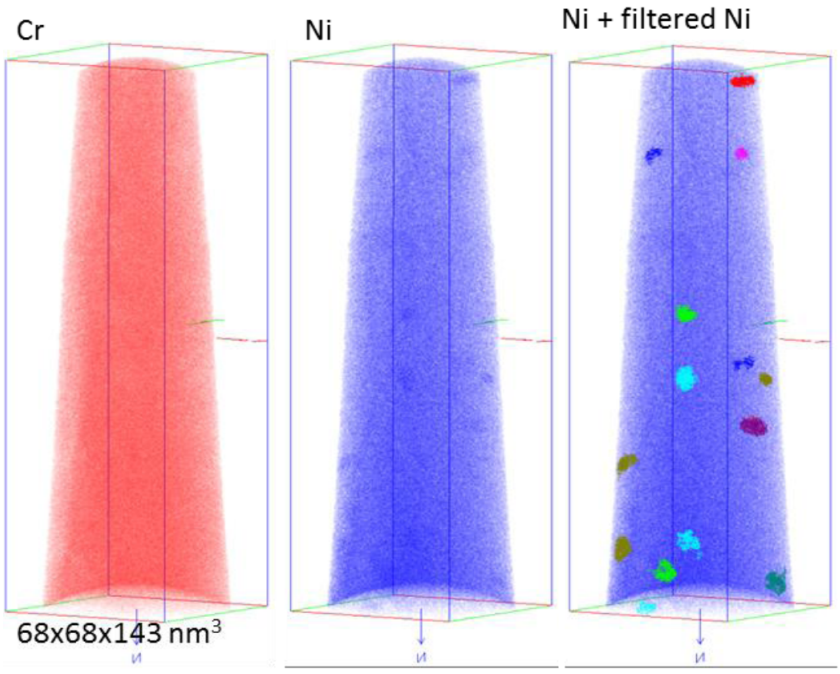

3D reconstruction of a FeNiCr typical bulk. Detected elements are represented separately. Ni-rich clouds, depleted in Cr, were detected. They are filtered and imaged in color on the right image. Other elements are distributed homogeneously[1].

Concerning irradiation damage investigations, the interaction could be extended to Helium cavities or voids observed in fast neutrons nuclear reactors. Although Frank loops are the most hardening defects in irradiated austenitic stainless steels, the TEM observation reveal the presence of voids which nucleate and swell to lead to their coalescence. However, the nucleation and swelling of these defects request a higher temperature of formation. It has been found that strengthening due to the voids can be significant as an irradiation effect in nuclear metals. Recent studies have shown that important effects can be revealed with atomistic modeling but they have always focused on pure materials although the FCC phase has been investigated. Another obstacle defect to point out is the Stacking Fault Tetrahedron (SFT). The SFT is a typical vacancy cluster produced by neutron irradiation. This SFT has a tetragonal shape composed by four stacking faults expanded on $\{111\}$ plans and locked by six sessile stair-rod dislocations. These obstacles are highly stable under shear stress. The complex mechanism of interaction has been clarified but it is unclear if it is the only process for SFT collapsing. Their annihilation is proven to be based on experimental data obtained in situ in a TEM. To a lesser extent, in austenitic stainless steels, irradiation enhances the appearance of small precipitates of γ' type (Ni_3Si). The study of temperature stability of γ' precipitates was performed and has shown that at 400°C, annealing does not affect the size and number density of the precipitates, which starts to be modified at 500°C with an increase of the precipitate size and a decrease of their number density. Thus, the study of the interaction mechanism between dislocation and small precipitates can be useful and realized in MD.

[1] A. Volgin, **PHD thesis** (2012) University of Rouen.

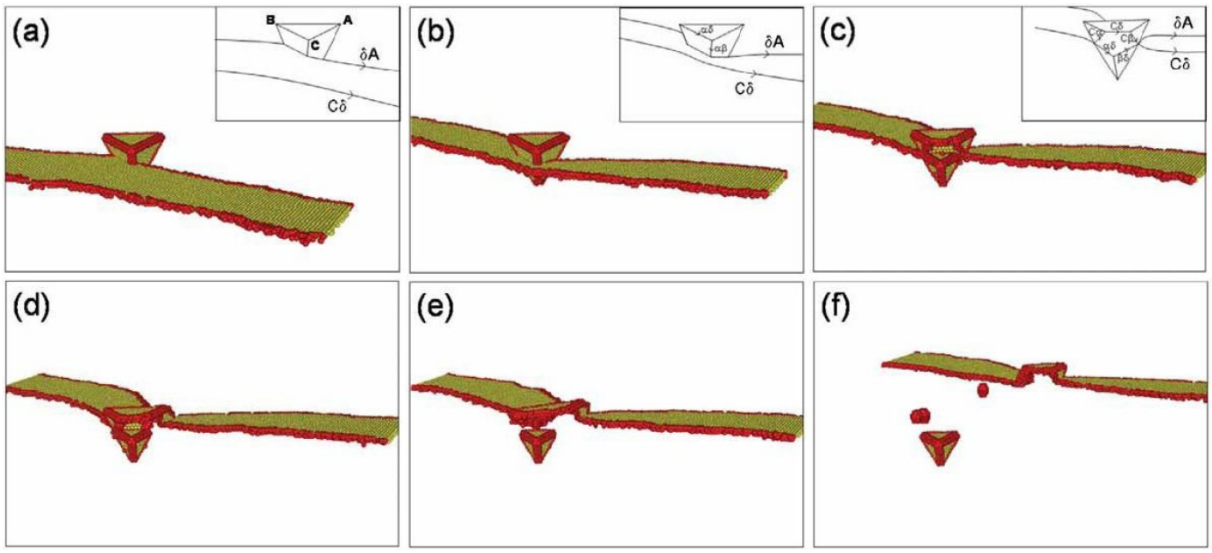

Partial absorption of a SFT into a superjog by an edge dislocation[2].

[2] Y. N. Osetsky, D. Rodney, D. J. Bacon, **Atomic-scale study of dislocation–stacking fault tetrahedron interactions. Part I: Mechanisms**, Phil. Mag., 86 (2006) 2295-2313.

Appendix I: Molecular Dynamics Techniques

MD is a numerical simulation technique that enables to mimic a material at the atomic scale. This simulation method can predict the chemical, physical and mechanical properties under conditions when experimental techniques have some difficulties due to a small spatial scale, an excessively elevated temperature, pressure, and hazardous material (radioactive). This simulation technique employs the resolution of Newton's equations.

AI.1. Principle

The main principle of MD consists in establishing the temporal evolution of the atomic positions. For this, the system is modeled as atoms or molecules as a mass set. With each particle *i* is associated a mass m_i, a position $\vec{r}_i$ and a velocity $\vec{v}_i$. The total energy E_i of an atom *i* is the sum of its potential energy E_p and its kinetic energy E_k. The total potential energy is the sum of the interaction potential energies. These potential energies include the interaction potential between atoms:

$$E_p = \Sigma E_{pi}^{\text{int}} \tag{AI.1}$$

The net force $\vec{F}_i$ on an atom *i* is equal to the gradient of the total potential energy of the system based on the position of atom:

$$\vec{F}_i = -\nabla E_p \tag{AI.2}$$

It can be decomposed into the sum of the potential interaction energy between atoms:

$$\vec{F}_i^{\text{int}} = -\nabla E_p^{\text{int}}(r_i) \tag{AI.3}$$

The system force is related to the atomic acceleration $\vec{a}_i$ with the Newton law

$$\vec{F}_i = m_i \vec{a}_i \tag{AI.4}$$

AI.2. Initialization of velocity

Particles are assigned an initial velocity defined by a norm and a direction. This velocity mimics atomic thermal vibration. The velocity vector distribution is equidistributed in the simulated crystal and correlated displacement of atoms must not happen such as: $\sum_{i=1,\,N} \vec{V}_i = \vec{0}$.

The system obeys to the distribution function of Maxwell-Boltzmann for velocities associated to temperature *T*:

$$f(v_i) = \frac{1}{Z_v} \exp\left(-\frac{m|v_i|^2}{2k_B T} \right), \text{ with } Z_v = \int \exp\left(-\frac{m|v|^2}{2k_B T} \right) dv = 1 \tag{AI.5}$$

Average kinetic energy of a system at equilibrium is defined by the following equation:

$$E_{kin} = \frac{3}{2} k_B T = \frac{\sum \frac{1}{2} m_i v_i^2}{N}$$

(AI.6)

At equilibrium, the instantaneous temperature of the system evolved around the target temperature *T*. Nevertheless, we can rescale the temperature to set $T = T^{inst}$. Thus it is necessary to set temperature for calculating the desired velocity.

AI.3. Integration of the Newton equation

The equation of Newton is integrated to determine the atomic position and velocity for each atom *i*:

$$\vec{F}_i = m\vec{a}_i \qquad \forall\, i \in [1, ..., N] \tag{AI.7}$$

Atomic positions and the potential energy allow defining the force exerted on each atom. The interactions between particles are thus defined and forces are expressed by the following relation:

The series of Taylor defines the position at a given moment

$$\vec{r}(t+\delta t) = \vec{r}(t) + \delta t \frac{\partial \vec{r}}{\partial t} + \frac{\delta t^2}{2} \frac{\partial^2 \vec{r}}{\partial t^2} + \frac{\delta t^3}{3 \times 2} \frac{\partial^3 \vec{r}}{\partial t^3} + \varepsilon(\delta t^4) \tag{AI.8}$$

$$\vec{r}(t-\delta t) = \vec{r}(t) - \delta t \frac{\partial \vec{r}}{\partial t} + \frac{\delta t^2}{2} \frac{\partial^2 \vec{r}}{\partial t^2} - \frac{\delta t^3}{3 \times 2} \frac{\partial^3 \vec{r}}{\partial t^3} + \varepsilon(\delta t^4) \tag{AI.9}$$

The Verlet Algorithm solves motion equations. It is based on the sum of eq. (AI.8) and (AI.9) which gives

$$\vec{r}_i(t+\Delta t) = 2\vec{r}_i(t) - \vec{r}_i(t-\Delta t) + \vec{F}_i(t)\frac{(\Delta t)^2}{m} + \varepsilon(\Delta t^4) \tag{AI.10}$$

The equation (AI.10) can be used to determine the position of the particles at a given time $(t+\Delta t)$, based on the position at *t* and $t - \Delta t$ of atoms. The velocity of atoms can be determined by the following expression:

$$\vec{v}_i(t) = [\vec{r}_i(t+\Delta t) - \vec{r}_i(t-\Delta t)]/(2\Delta t) \tag{AI.11}$$

Then Equation (AI.10) is solved to determine the positions of atoms at $t + \Delta t$. The time step chosen for our simulations is Δt=1x10^{-15} s.

Appendix II: Average Elastic Constants

Considering isotropic crystals is a simplification. In fact, most crystals are anisotropic, and the isotropic theory is an approximation. The isotropic theory is a cut off to lead to useful results but usually quickly overtaken. First of all, errors generated by isotropic elasticity are about 20-30% completed by the other approximation raised with the dislocation theory and experimental observations [1].

There are some cases when the use of the anisotropy theory is simplified. For example when the dislocation is straight along a direction of high level of symmetry, the application of anisotropic elasticity is highly simplified. The complexity raised by this study involves using isotropic elastic constants. The most reliable values are obtained when the average is made over all the possible directions of the crystal axes. But this averaging can be done over the elastic constant C_{ijkl} [2] or over the elastic compliances S_{ijkl}. Elastic constants are appropriate when we consider strain equivalents on the grains in a polycrystal whereas elastic compliances are better for considering states of stress equivalents. The Voigt average [3] over C_{ijkl} is most appropriate for cases involving local strains around dislocations. The cases where stress fields are considered require using the Reuss average [4] over the S_{ijkl} . Thus, these two methods set the limits for the shear modulus μ and the Poisson's ratio ν.

AII.1. The Voigt Average

For cubic crystals, the number of elastic constants is reduced to 21 because of the crystal symmetry [1]. If the coordinate axes match with the crystal axes, as cubic crystal is invariant in symmetry to 90° rotations, then $C_{iiii}=C_{11}$, $C_{iijj}=C_{12}$ and $C_{ijij}=C_{44}$. In that case, the 6×6 elastic constant matrix is:

$$\begin{bmatrix} C_{11} & C_{12} & C_{12} & 0 & 0 & 0 \\ C_{12} & C_{11} & C_{12} & 0 & 0 & 0 \\ C_{12} & C_{12} & C_{11} & 0 & 0 & 0 \\ 0 & 0 & 0 & C_{44} & 0 & 0 \\ 0 & 0 & 0 & 0 & C_{44} & 0 \\ 0 & 0 & 0 & 0 & 0 & C_{44} \end{bmatrix} \quad \text{(AII.1)}$$

and for cubic crystals the relation (AII.2) in a 9×9 representation gives the following relation:

$$C_{ijij} = 3C_{11} + 6C_{44} \qquad \text{and} \qquad C_{iijj} = 3C_{11} + 6C_{12} \quad \text{(AII.2)}$$

and the solving for μ and λ gives the following average values [1]

$$\begin{aligned} \lambda + 2\mu &= C_{11} + \tfrac{2}{5}H \\ \mu &= C_{44} - \tfrac{1}{5}H \\ \lambda &= C_{12} - \tfrac{1}{5}H \end{aligned} \quad \text{(AII.3)}$$

with H the anisotropy factor

$$H = 2C_{44} + C_{12} - C_{11} \quad \text{(AII.4)}$$

In the case of the 316L stainless steel, the elastic constants used are those found by Mangalick *et al.* [5] from a ternary Fe-Ni_X-Cr_Y single crystal. Those elastic constants are respectively: C_{11}=210 GPa, C_{12}=130 GPa and C_{44}=120 GPa. Thus the anisotropy ratio is in our case H=160 GPa, which make 316L steel highly anisotropic with λ=98 GPa and μ=88 GPa. Another commonly used elastic constant is Poisson's ratio ν related with the other useful constants as:

$$\nu = \frac{\lambda}{2(\mu + \lambda)} \tag{AII.5}$$

and in our case ν= 0.26.

AII.2. The Reuss Average

We now consider the inverse coefficients called elastic compliance constants S_{ijkl}. The equivalent system generated in this case for elastic compliances is:

$$\begin{aligned} \frac{1}{E_R} &= \tfrac{1}{15}\left(2S_{ijij} + S_{iijj}\right) \\ \frac{\nu_R}{E_R} &= \tfrac{1}{15}\left(S_{ijij} - 2S_{iijj}\right) \\ \frac{1}{\mu_R} &= \tfrac{1}{15}\left(6S_{ijij} - 2S_{iijj}\right) \end{aligned} \tag{AII.6}$$

where the index R indicates the Reuss averages and E is the Young Modulus. The equivalent system obtained in (1.3) for elastic compliances is:

$$\begin{aligned} \frac{1}{E_R} &= S_{11}^{'} - \tfrac{2}{5}J \\ \frac{1}{\mu_R} &= S_{44}^{'} + \tfrac{4}{5}J \\ \frac{\nu_R}{E_R} &= -S_{12}^{'} - \tfrac{1}{5}J \end{aligned} \tag{AII.7}$$

where J is defined as

$$J = \left(S_{11}^{'} - S_{12}^{'} - \tfrac{1}{2}S_{44}^{'}\right) \tag{AII.8}$$

by inverting the 6×6 matrix set in (AII.1), elastic compliances are expressed with the elastic constants in the following way:

$$\begin{aligned} S_{11}^{'} &= \frac{C_{11} + C_{12}}{C_{11}^{\,2} + C_{11}C_{12} - 2C_{12}^{\,2}} \\ S_{12}^{'} &= \frac{-C_{12}}{C_{11}^{\,2} + C_{11}C_{12} - 2C_{12}^{\,2}} \\ S_{44}^{'} &= \frac{1}{C_{44}} \end{aligned} \tag{AII.9}$$

and the referring elastic compliances based on the associated elastic constants [5] are S_{11}=9.04, S_{12}=-3.46 and S_{44}=8.33 10^{-12} Pa^{-1}. Thus the averaging set in the case of Reuss method gives a compliance anisotropic factor J=8.34 10^{-12} Pa^{-1}, a Young modulus E_R=175 GPa, a shear modulus μ=67 GPa and a Poisson's Ratio v=0.31.

The values for pure crystals used in this study as well as the elastic constants used in the ternary potential are listed in Table AII.1.

Table AII.3.: Elastic constants for pure constitutive elements and ternary alloy FeNiCr.

Crystal	s'_{11}	$-s'_{12}$	s'_{44}	J	E_R	v_R	μ_R	C_{11}	C_{12}	C_{44}	H	μ	λ	N
Fe [6]	7.60	2.87	8.92	6.01	192.5	0.32	72.8	242	146.5	112	128.5	86.3	120.8	0.29
Ni [2]	7.34	2.74	8.02	6.06	203.4	0.31	77.7	246.5	147.3	124.7	150.2	94.66	117.3	0.28
Cr [7]	3.00	0.43	9.92	-1.53	276.9	0.20	115	350	57.8	101	-90.2	119.04	75.8	0.19
316L exp. [8, 9, 10]	7.92-9.97	2.93-3.91	8.20-9.00	6.75-9.38	191.6-160.8	0.31-0.33	60.6-74.3	204-226	132-134	111-122	150-152	81-91.6	102-103.6	0.27-0.29
FeNi10Cr20 pot.[11]	9.2	3.59	7.75	8.92	177.6	0.32	67.2	214	136	129	180	93	100	0.26

Appendix III: Properties of pure potentials

Table AIII.1: Static properties of pure elements [11].

	Iron		Nickel		Chromium	
	Target	Potential	Target	Potential	Target	Potential
E_{coh} *(fcc) (eV/at.)*	—	4.12	4.45	4.45	—	3.69
ΔE_{coh} *(fcc-bcc) (eV/at.)*	-0.16	+0.11	+0.15	+0.19	-0.39	+0.05
ΔE_{coh} *(fcc-hcp) (eV/at.)*	—	0.00	+0.03	+0.02	—	+0.04
a (fcc) (Å)	3.425[3]	3.499	3.519	3.519	3.610	3.584
a (hcp) (Å)	—	2.474[4]	—	2.488[5]	—	2.523[6]
a (bcc) (Å)	2.867	2.962[7]	2.801	2.801	2.878	3.149[8]
C_{11} *(GPa)*	141	141	247	247	249	247
C_{12} *(GPa)*	100	100	147	147	178	183
C_{44} *(GPa)*	108	108	125	125	143	145
E_{SF} *(mJ.m^{-2})*	4	0	111-128	113	341	272
E_m *(Vac) (eV)*	0.95-1.05	0.61	1.08-1.30	1.17	2.19	2.25
E_f *(Vac) (eV)*	1.89-1.95	1.94	1.45-1.79	1.48	2.14	2.11
E_f *(*$\langle 100 \rangle$ *SIA) (eV)*	3.53-3.65	3.60	4.07-4.11	4.08	—	5.10
E_f *(*$\langle 110 \rangle$ *SIA) (eV)*	—	3.91	4.99-4.91	4.71	—	5.60
E_f *(*$\langle 111 \rangle$ *SIA) (eV)*	4.56	4.61	4.69-4.72	4.76	—	5.40
E_f *(Octa SIA) (eV)*	4.35	3.87	4.25-4.32	4.89	—	5.71
E_f *(Tetra SIA) (eV)*	4.32	4.58	4.69-4.71	4.99	—	5.56

[3] $c/a = 1.065.$
[4] $c/a = 1.633.$
[5] $c/a = 1.663.$
[6] $c/a = 1.736.$
[7] $c/a = 0.895.$
[8] $c/a = 0.793.$

The static properties of the pure potentials are summarized in Table AIII.1. A comparison is established for each element with the target values selected from the Density Functional Theory (DFT) and the experiments. The main purpose of this potential is to reproduce correctly the elastic constants, the SFE and the stability of the FCC phase in the temperature range 0-900 K. In the case of Fe and Cr, this FCC phase is artificially stabilized as the maintaining of BCC phase for these two elements would disturb the stabilities of the system. As the FCC phase is the most stable for Ni, a strong base is attributed to this element. In general, the potential values obtained for Fe and Ni agree with the experimental values whereas the Cr results are in poor agreement.

The target values for the FCC SFE calculations are based on the experimental results (128 mJ.m^{-2} for Ni) [12] and the other FCC values are defined by extrapolation of low temperature (300 K) thermodynamic results [13]. As well as other data, the SFE values are well reproduced by the potential for Ni and Fe elements but are underestimated by ~70 mJ.m^{-2}. However, as the correct value is defined for the target composition, this can be neglected. In Figure AIII.1, the $\langle 112 \rangle \{111\}$ gamma lines are represented for the three constitutive elements and the target composition. The gamma lines are smooth which is a prerequisite to simulate the motion of the dislocation core properly. The SFE can be identified by following the different lines around 0.4 $\langle 112 \rangle$ distance (a_0).

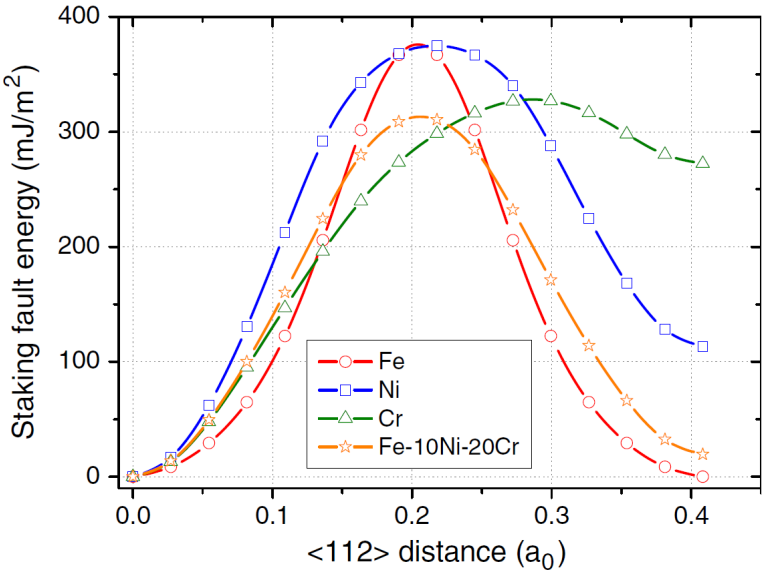

Figure AIII.2: $\langle 112 \rangle \{111\}$ gamma cut calculated for the pure elements and Fe-Ni$_{10}$-Cr$_{20}$ from [11].

The different SIAs configurations for Ni and Cr elements are obtained from DFT calculations [14]. Due to the Cr FCC phase instability, no data are available for SIAs. The $\langle 100 \rangle$ dumbbell is predicted to be the ground state by referring to the DFT results. In Figure AIII.2, the average lattice energy ($E^*=E/E_{coh}$) is compared with Rose's universal equation of state [15]. This equation describes the energy per atom $E(a^*)$ for the lattice under uniform expansion or contraction. Both Ni and Fe match with the equation of state. For Fe, there is a disagreement for large expansion and contraction. The latter is induced by the short interaction range of the potential (4.0 Å compared with 5.6 Å for both Ni and Cr) and the former is due to the incompatibility with the $\langle 100 \rangle$ dumbbell formation energy.

For Ni element the elastic constants match the experimental data [16]. As Fe and Cr are not stable in the FCC phase, there are no data concerning elastic constants and as for SFE, the reported values are an extrapolation of the experimental results measured of Ni-Fe and Ni-Cr elastic constants taken from [16, 17]. The elastic constants resulting from both Fe and Cr are in good agreement with the targeted values.

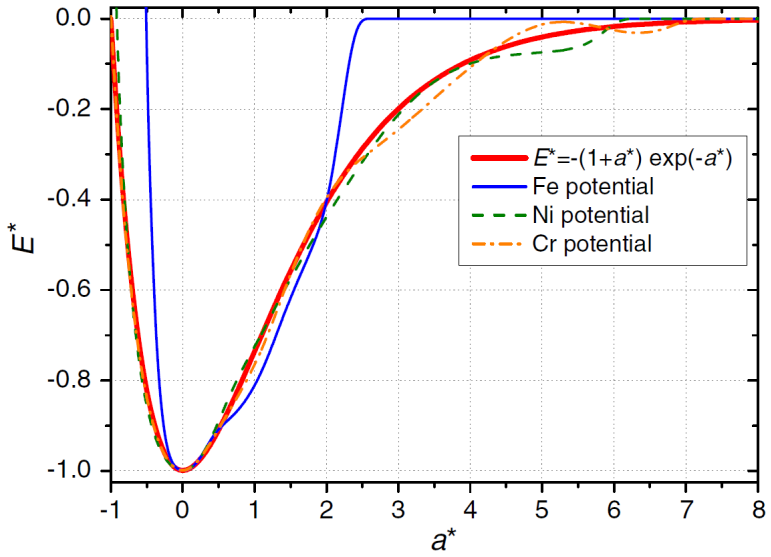

Figure AIII.3: Evaluation of Rose's equation for the different potentials from [11].

Appendix IV: Resulting configurations for the 2nd and 3thd passage


Shearing


Absorption


Unfaulting after reaction

Temperature	Edge Dislocation	V_1 (111)	V_2 $(1\bar{1}\bar{1})$	V_3 $(\bar{1}\bar{1}1)$	V_4 $(\bar{1}1\bar{1})$
300 K	Seed #1	Previously Absorbed			
	Seed #2	Previously Absorbed			
	Seed #3				
600 K	Seed #1	Previously Absorbed	Previously Absorbed	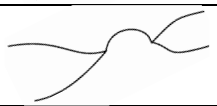	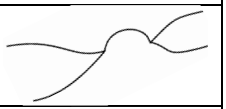
	Seed #2	Previously Absorbed			
	Seed #3	Previously Absorbed	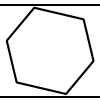	Previously Absorbed	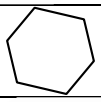
900 K	Seed #1	Previously Absorbed	Previously Absorbed		
	Seed #2	Previously Absorbed			
	Seed #3	Previously Absorbed		Previously Absorbed	

Table AIV.1: Resulting configurations between edge dislocation and Frank loop (*D*=2 nm) for the second passage with an *M+* dislocation motion. The above legend indicates the notation used in the table. The reaction is conducted at 300 K, 600 K and 900 K for three alloying random configurations. The loops have a $\langle 110 \rangle$ side and are hexagonal.

 Shearing  Absorption  Unfaulting after reaction

Temperature	Edge D	V_1 (111)	V_2 $(1\bar{1}\bar{1})$	V_3 $(\bar{1}\bar{1}1)$	V_4 $(\bar{1}1\bar{1})$
300 K	Seed #1	Previously Absorbed	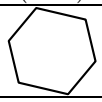	Previously Absorbed	Previously Absorbed
	Seed #2	Previously Absorbed	Previously Absorbed	Previously Absorbed	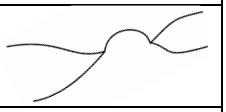
	Seed #3		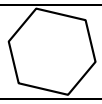	Previously Absorbed	
600 K	Seed #1	Previously Absorbed	Previously Absorbed	Previously Absorbed	Previously Absorbed
	Seed #2	Previously Absorbed	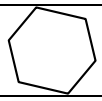	Previously Absorbed	Previously Absorbed
	Seed #3	Previously Absorbed		Previously Absorbed	
900 K	Seed #1	Previously Absorbed	Previously Absorbed	Previously Absorbed	Previously Absorbed
	Seed #2	Previously Absorbed	Previously Absorbed	Previously Absorbed	Previously Absorbed
	Seed #3	Previously Absorbed	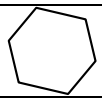	Previously Absorbed	Previously Absorbed

Table AIV.2: Resulting configurations between edge dislocation and Frank loop (*D*=2 nm) for the third passage with an *M+* dislocation motion. The above legend indicates the notation used in the table. The reaction is conducted at 300 K, 600 K and 900 K for three alloying random configurations. The loops have a $\langle 110 \rangle$ side and are hexagonal.

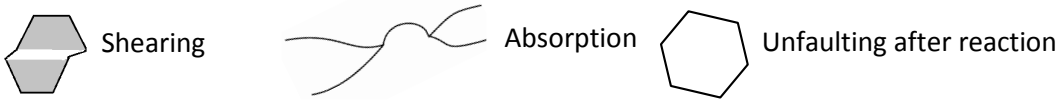

Temperature	ED	V_1 (111)	V_2 $(1\bar{1}\bar{1})$	V_3 $(\bar{1}\bar{1}1)$	V_4 $(\bar{1}1\bar{1})$
300 K	Seed #1				
	Seed #2				
	Seed #3	Previously Absorbed		Previously Absorbed	
600 K	Seed #1			Previously Absorbed	New FL plane $1/3\{111\}$
	Seed #2			Previously Absorbed	
	Seed #3				New FL plane $1/3\{\bar{1}\bar{1}1\}$
900 K	Seed #1	Previously Absorbed	Previously Absorbed	Previously Absorbed	
	Seed #2	Previously Absorbed		Previously Absorbed	Previously Absorbed
	Seed #3	Previously Absorbed	Previously Absorbed		

Table AIV.3: Resulting configurations between edge dislocation and Frank loop (*D*=2 nm) for the second passage with an *M*- dislocation motion. The above legend indicates the notation used in the table. The reaction is conducted at 300 K, 600 K and 900 K for three alloying random configurations. The loops have a $\langle 110 \rangle$ side and are hexagonal.

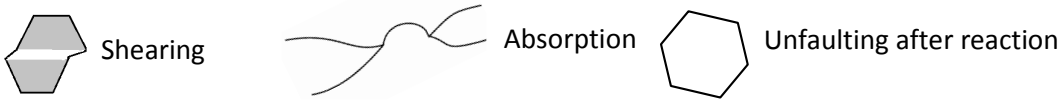

Temperature	ED	V_1 (111)	V_2 $(1\bar{1}\bar{1})$	V_3 $(\bar{1}\bar{1}1)$	V_4 $(\bar{1}1\bar{1})$
300 K	Seed #1	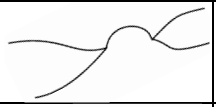		Previously Absorbed	
	Seed #2	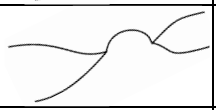			
	Seed #3	Previously Absorbed	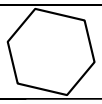	Previously Absorbed	
600 K	Seed #1	Previously Absorbed		Previously Absorbed	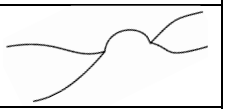
	Seed #2		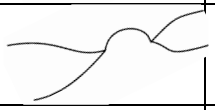	Previously Absorbed	
	Seed #3	Previously Absorbed		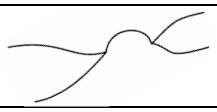	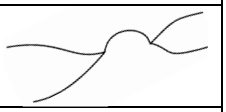
900 K	Seed #1	Previously Absorbed	Previously Absorbed	Previously Absorbed	
	Seed #2	Previously Absorbed	Previously Absorbed	Previously Absorbed	Previously Absorbed
	Seed #3	Previously Absorbed	Previously Absorbed	Previously Absorbed	Previously Absorbed

Table AIV.4: Resulting configurations between edge dislocation and Frank loop (*D*=2 nm) for the third passage with an *M*-dislocation motion. The above legend indicates the notation used in the table. The reaction is conducted at 300 K, 600 K and 900 K for three alloying random configurations. The loops have a $\langle 110 \rangle$ side and are hexagonal.

Appendix V: Edge dislocation and Frank loop interaction: unpinning stress results τ_{max}

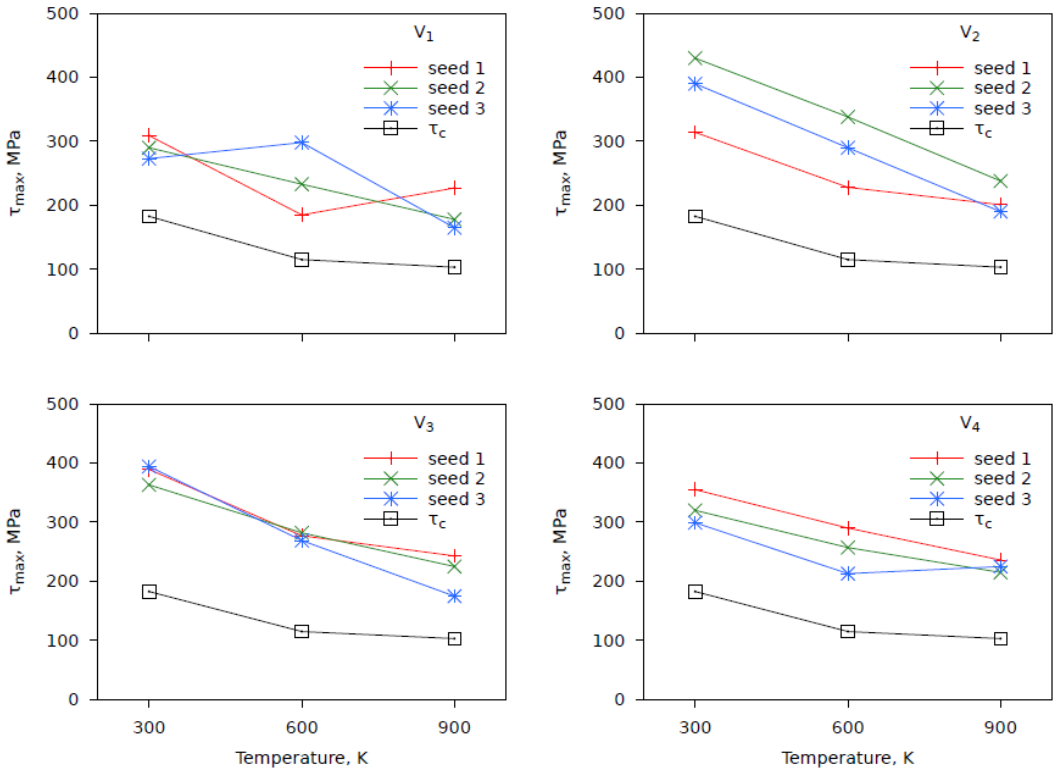

Figure AV.1: Unpinning stress depending on temperature for the four orientations of the FL and three alloying random generators in the case of 2 nm Frank loop for the first interaction and the *M+* motion.

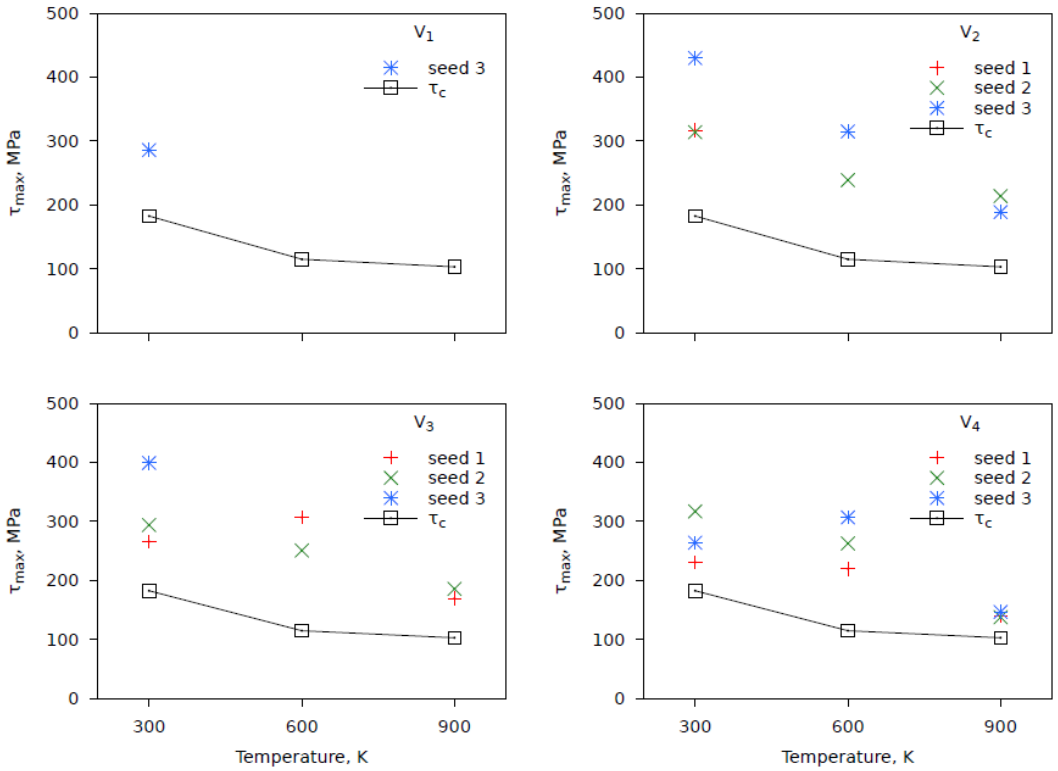

Figure AV.2: Unpinning stress depending on temperature for the four orientations of the FL and three alloying random generators in the case of 2 nm Frank loop for the second interaction and the *M+* motion.

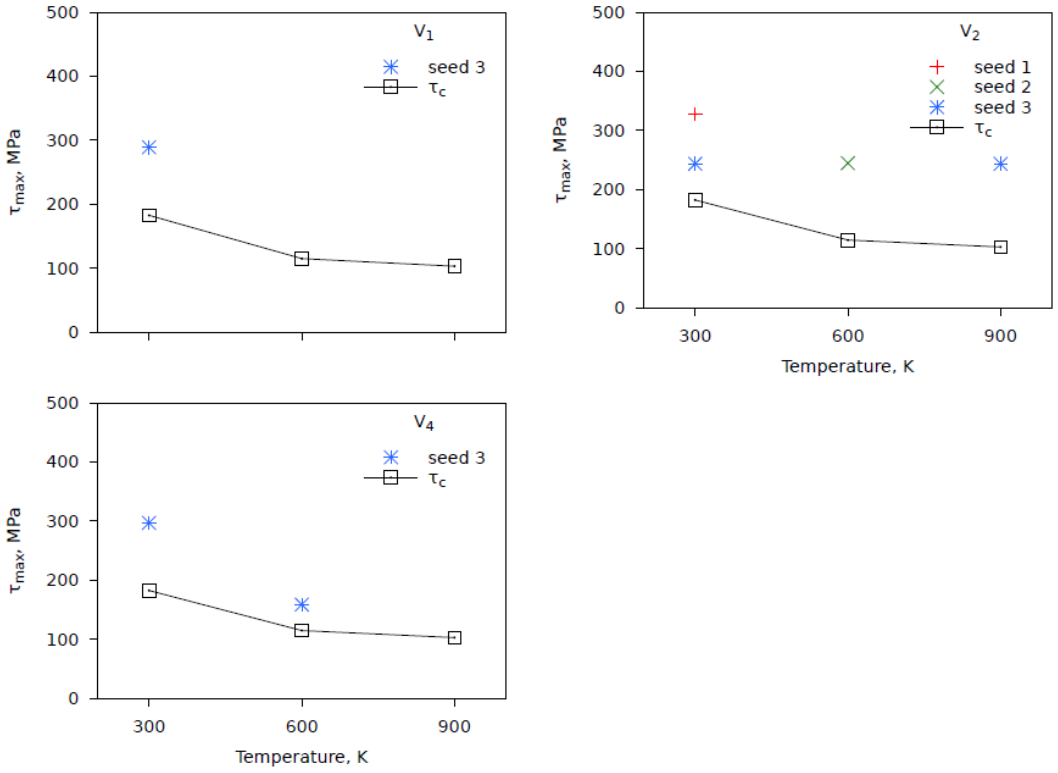

Figure AV.4: Unpinning stress depending on temperature for the four orientations of the FL and three alloying random generators in the case of 2 nm Frank loop for the third interaction and the *M+* motion.

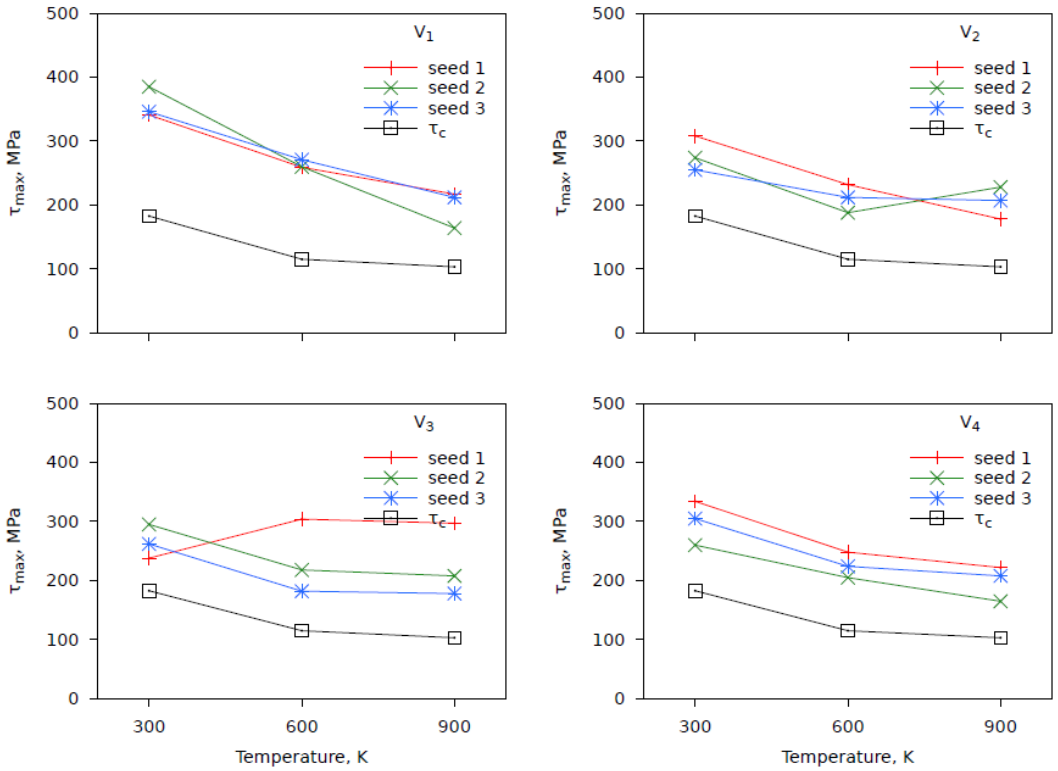

Figure AV.5: Unpinning stress depending on temperature for the four orientations of the FL and three alloying random generators in the case of 2 nm Frank loop for the third interaction and the *M*- motion.

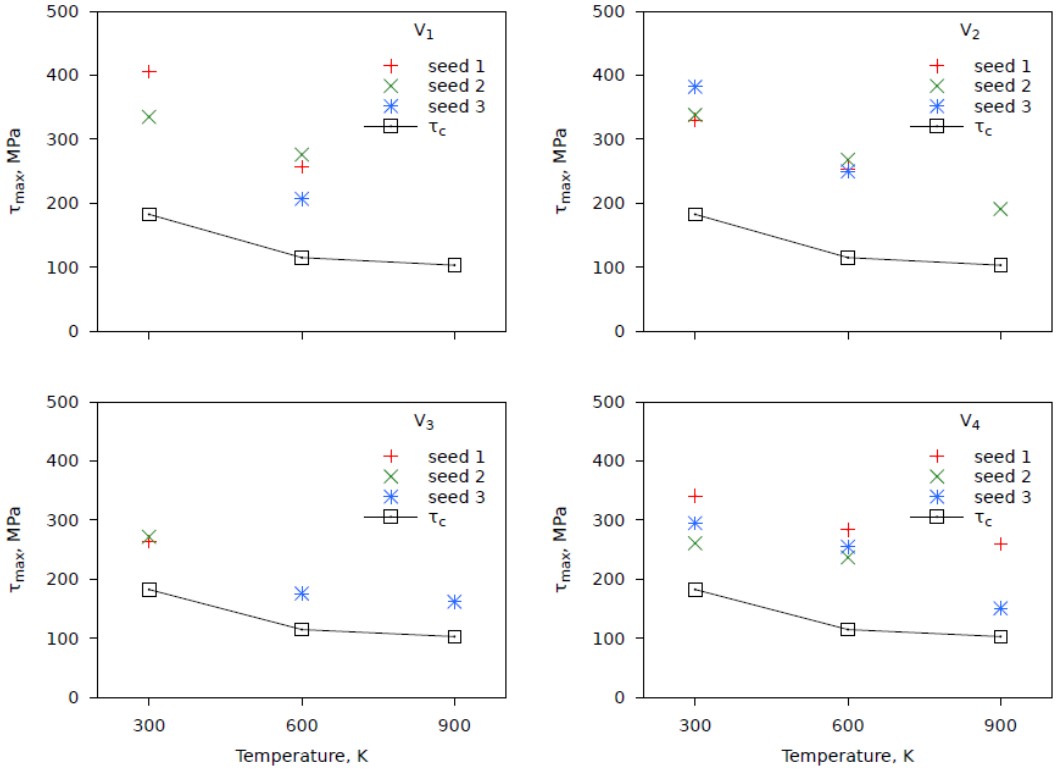

Figure AV.6: Unpinning stress depending on temperature for the four orientations of the FL and three alloying random generators in the case of 2 nm Frank loop for the second interaction and the *M*- motion.

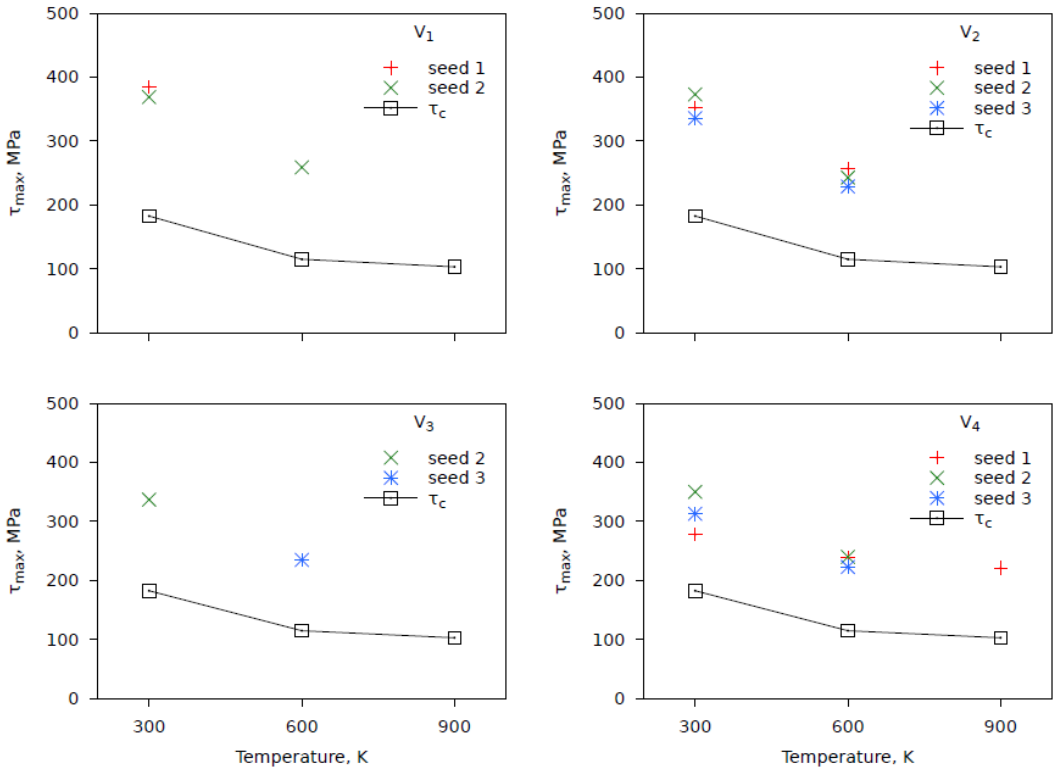

Figure AV.7: Unpinning stress depending on temperature for the four orientations of the FL and three alloying random generators in the case of 2 nm Frank loop for the third interaction and the *M-* motion.

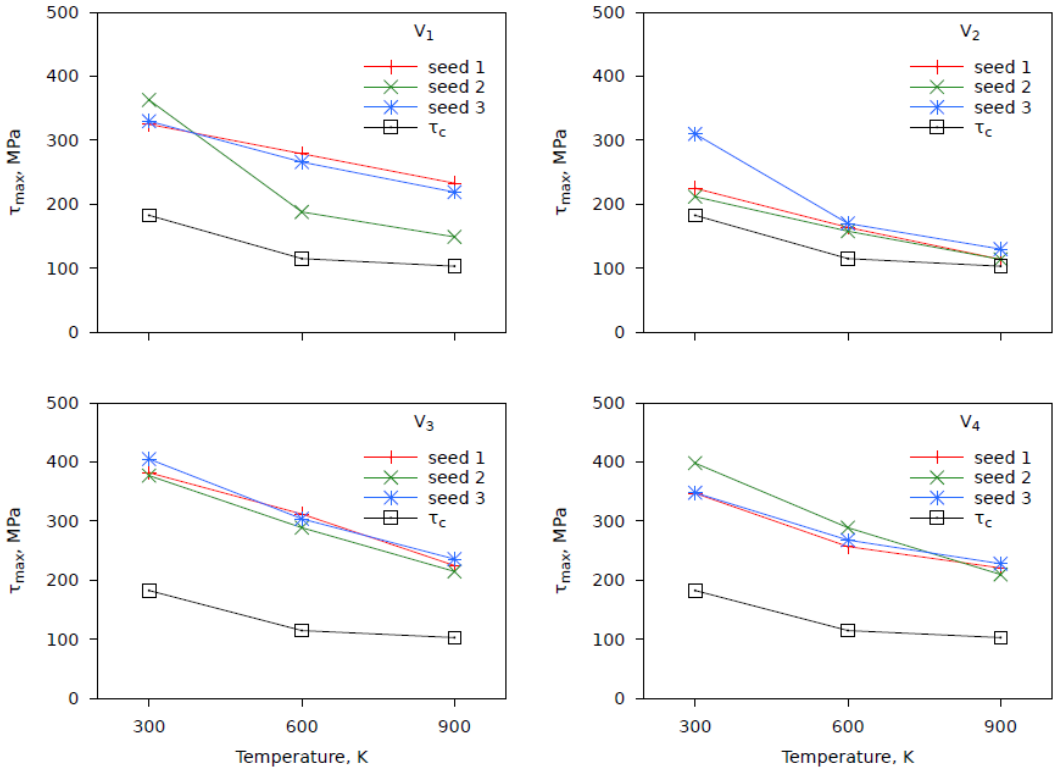

Figure AV.8: Unpinning stress depending on temperature for the four orientations of the FL and three alloying random generators in the case of 10 nm Frank loop for the first interaction and the *M+* motion.

Appendix VI: The Fe-Ni-Cr system

The Fe-Ni-Cr alloy is the ternary system alloy modeled to understand the properties of the non-irradiated and irradiated stainless steels. Four solid phases are involved in the Fe-Ni-Cr ternary phase diagram. At equilibrium state and depending on the alloying content, these four phases are:

1. the *α* phase, which exhibits a BCC solid solution. This *α*-Fe is the low temperature phase;
2. the *α'* phase, which is equivalent to the *α* phase but based on a solid solute solution of Cr in Fe BCC host matrix;
3. the *γ* phase, or high temperature phase, based on the FCC solid solution *γ*-Fe and *γ*-Ni;
4. the *σ* phase which is an intermetallic phase. The intermetallic phases precipitate for a wide range of Cr content in the Fe matrix and are derived from the Cr-Fe binary.

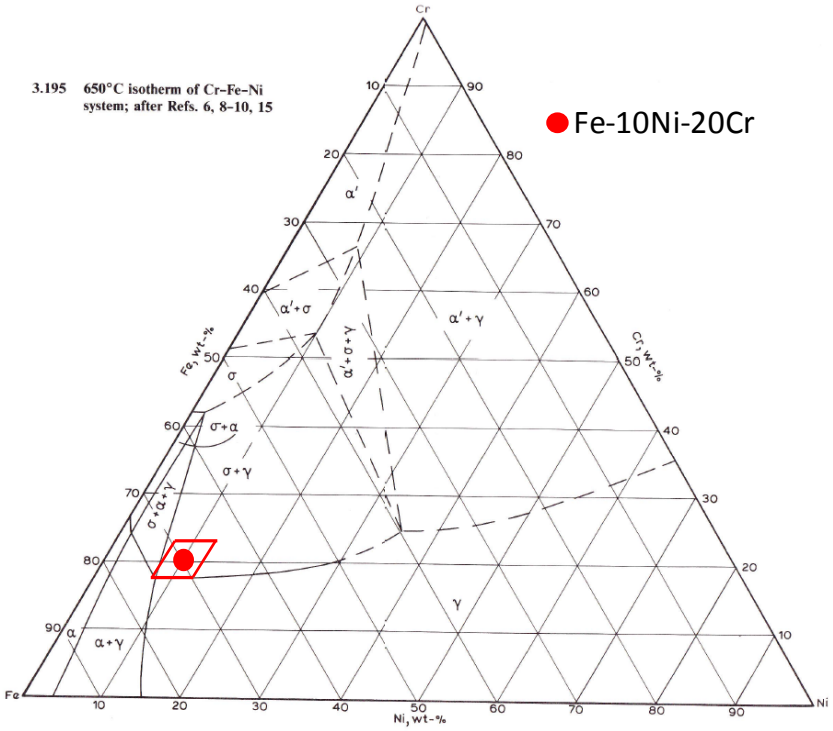

Figure AVI.1: Fe-Ni-Cr ternary phase diagram at 650°C [18]. The target composition Fe-Ni_{10}-Cr_{20} is represented by the red mark. The delimited area indicates the variations of compositions near the Fe-Ni_{10}-Cr_{20} target composition during the simulations.

At 650°C, the target material Fe-Ni_{10}-Cr_{20} is a binary FCC phase *σ+γ*. However, around the composition close to the target alloy, the composition can be a mixture of three different phases *α+γ+σ*. If we consider another element, the different domains and separations are still reported but their sizes are affected. For a higher temperature, the main *γ* domains are extended at the expense of the *α* domains.

Appendix VII: Stress-strain curves for 10^7 and 10^8 s^{-1} strain rate

Figure AVII.1 and Figure AVII.2 show the stress-strain curves at different temperatures. The strain rate associated to Figure AVII.1 and Figure AVII.2 can be assimilated to a dislocation velocity of respectively 55 $m.s^{-1}$ and 550 $m.s^{-1}$. Similarly for 10^6 s^{-1} strain rate, the simulations start with an elastic regime, during which the dislocation is immobile at a bottom of what can be assimilated to a Peierls valley [19] and the stress increases linearly with the strain. In the case of a 10^8 s^{-1} strain rate, no pinning events appear as the stress response is continuous for all the strain.

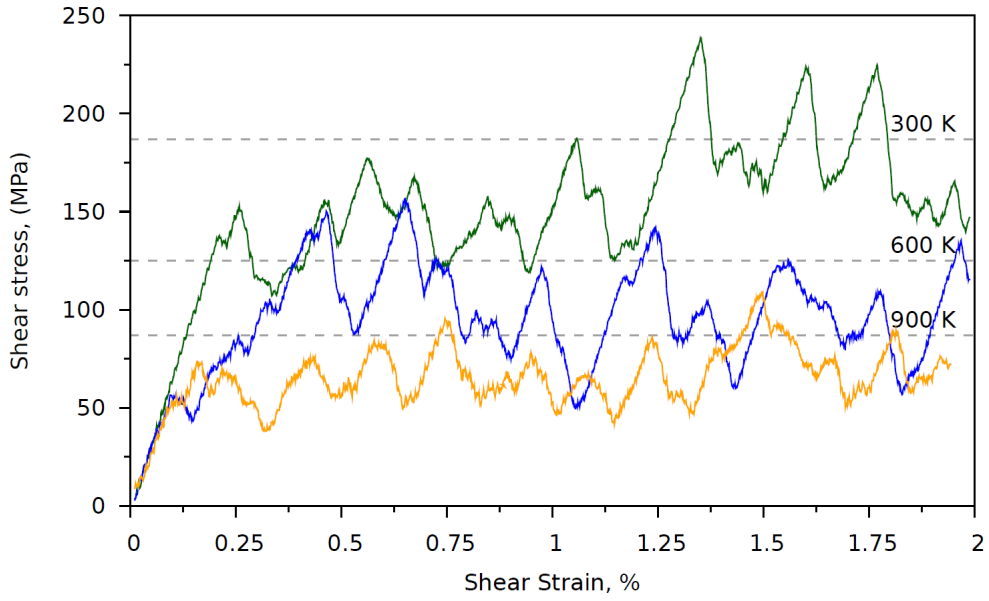

Figure AVII.1: Stress-strain dependence obtained by a dynamic modeling of dislocation motion under applied strain for different temperatures at 10^7 s^{-1} strain rate.

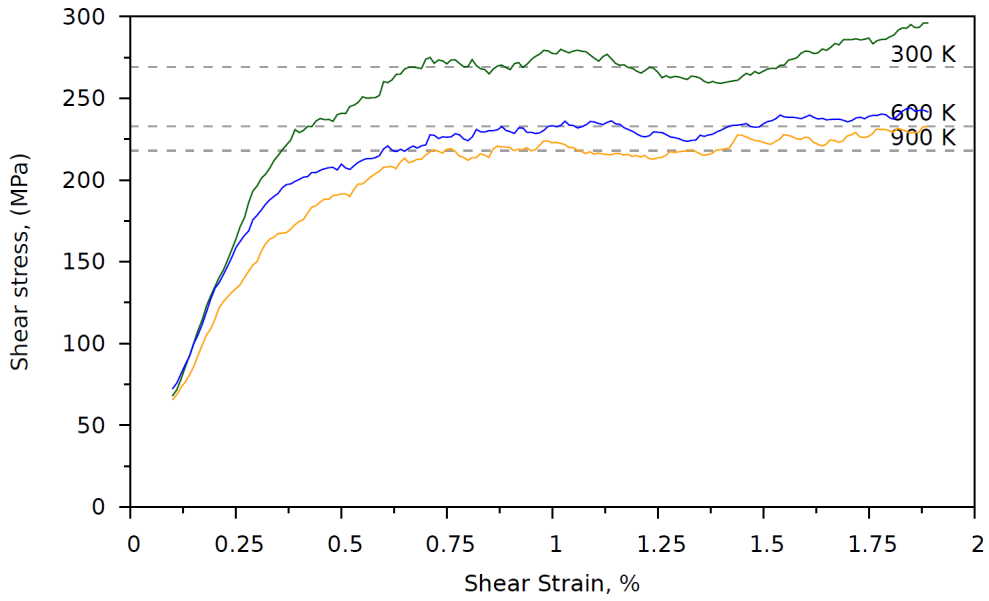

Figure AVII.2: Stress-strain dependence obtained by a dynamic modeling of dislocation motion under applied strain for different temperatures at 10^8 s^{-1} strain rate.

References

- Appendices -

[1] J. P. Hirth, J. Lothe, **Theory of Dislocations**, Krieger, Malabar (1982).
[2] H. B. Huntington, **The Elastic Constants of Crystals**, Solid State Phys., 7 (1958) 213-251.
[3] W. Voigt, **Lehrbuch der Kristalphysik**, Teubner, 1928.
[4] A. Reuss, **Berechnung der Fliessgrenze von Mischkristallen auf Grund der Plastizitäsbendingung für Einfristalle,** Z. Angew Math. Mech., 9 (1929) 49-58.
[5] M. C. Mangalick, N. F. Fiore, **Orientation Dependence of Dislocation Damping and Elastic Constants in Fe-18Cr-Ni Single Crystals**, Transactions of the Metallurgical Society of AIME, 242 (1968) 2363-2364.
[6] W. P. Mason, **"Piezoelectric Crystals and Their Applications to Ultrasonics"**, Van Nostrand, New York, 1950.
[7] D. I. Bolef, J. de Klerk, **Anomalies in the elastic constants and thermal expansion of chromium single crystals**, Phys. Rev., 129 (1963) 1063-1067.
[8] H. M. Ledbetter, **Monocrystal elastic constants in the ultrasonic study of welds**, Br. J. Non-Destr. Test., 23 (1985) 9-13.
[9] H. M. Ledbetter, **Predicted single-crystal elastic constants of stainless steel 316**, Ultrasonics, 34 (1981) 286-287.
[10] M. G. Silk, H. Lidington, G. F. Hammond, **A Time Domain Approach to Crack Location and Sizing in Austenitic Welds**, Brit. J. of NDT, 22 (1980) 55-61.
[11] G. Bonny, D. Terentyev, R. C. Pasianot, S. Poncé, A. Bakaev, **Interatomic potential to study plasticity in stainless steels: the FeNiCr model alloy**, Modelling Simul. Mater. Sci. Eng., 19 (2011) 085008.
[12] L. E. Murr, **Interfacial Phenomena in Metals and Alloys**, Addison-Wesley (1975).
[13] A. P. Miodownik, **CALPHAD**, 2 (1978) 207-226.
[14] T. P. C. Klaver, G. J. Ackland, D. J. Hepburn, **Defect and solute properties in dilute FeNiCr austenitic alloys: an ab initio study**, Phys. Rev., B 85 (2012) 174111.
[15] J. H. Rose, J. R. Smith, F. Guinea, J. Ferrante, **Universal features of the equation of state of metals**, Phys. Rev., B 29 (1984) 2963-2969.
[16] G. Simmons, H. Wang, **Single crystals elastic constants and calculated aggregate properties**, Cambridge, MA: MIT Press (1977).
[17] R. W. Smith, G. S. Was, **Application of molecular dynamics to the study of hydrogen embrittlement in Ni-Cr-Fe alloys**, Phys. Rev., B 40 (1989) 10322-10336.
[18] G. V. Raynor, V. G. Rivlin, **Cr-Fe-Ni Phase Equilibria in Iron Ternary Alloys**, Institute of Metals, London (1988) 316-332.
[19] R. Peierls, **The size of a dislocation**, Proceedings of the Physical Society, 52 (1940) 34.